

# Fakultät für Physik und Astronomie

Ruprecht-Karls-Universität Heidelberg

**Diplomarbeit**  
**Im Studiengang Physik**  
**vorgelegt von**  
**Max Neuner**  
**aus Heidelberg**  
**2012**



Measurement of the CP-violating phase  $\phi_s^{(-)}$  in  $B_s^0 \rightarrow J/\Psi\pi^+\pi^-$  decays at  
the LHCb experiment

Die Diplomarbeit wurde von Max Neuner  
ausgeführt am  
Physikalischen Institut  
unter der Betreuung von  
Herrn Prof. Dr. Ulrich Uwer



**Abstract** In this work, the CP-violating phase  $\phi_s$  is determined by measuring the time-dependent CP asymmetry of  $B_s^0 \rightarrow J/\Psi\pi^+\pi^-$  decays. The phase  $\phi_s$  is an observable that is very sensitive to new contributions to  $B_s^0$ - $\bar{B}_s^0$  mixing. Therefore, its precise determination tests the existence of new particles contributing to the loop corrections of mixing. The phase  $\phi_s$  is determined using a 2-dimensional maximum likelihood fit of the mass and proper time distributions. Resolution and acceptance effects are accounted for. The data sample that has been collected in 2011 by the LHCb-experiment at a center of mass energy of  $\sqrt{s} = 7$  TeV, corresponds to an integrated luminosity of  $\mathcal{L} = 1.03 \text{ fb}^{-1}$ . The fit yields  $7148 \pm 97$   $B_s^0 \rightarrow J/\Psi\pi^+\pi^-$  signal candidates and the phase is determined as

$$\phi_s = -0.074 \pm 0.177 \text{ (stat)} \pm 0.015 \text{ (syst) rad}$$

which is compatible with the Standard Model expectation for  $\phi_s^{SM} = (-0.0363^{+0.0016}_{-0.0015}) \text{ rad}$  [20].

**Kurzfassung** In dieser Arbeit wird die CP-verletzende Mischungsphase  $\phi_s$  mittels einer Messung der zeitabhängigen CP Asymmetrie von  $B_s^0 \rightarrow J/\Psi\pi^+\pi^-$  Zerfällen bestimmt. Die Mischungsphase  $\phi_s$  ist eine Observable, die sehr sensitiv auf neue Beiträge zur  $B_s^0$ - $\bar{B}_s^0$  Mischung ist. Ihre präzise Bestimmung testet deshalb die Existenz möglicher neuer Teilchen in den Quantenkorrekturen der Mischung. Die Phase  $\phi_s$  wird mittels eines 2 - dimensional Maximum Likelihood Fits der Massen- und Zerfallszeitverteilung bestimmt. Auflösungs- und Akzeptanzeffekte werden dabei berücksichtigt. In den im Jahr 2011 am LHCb-Experiment bei einer Schwerpunktsenergie von  $\sqrt{s} = 7$  TeV gesammelten Daten, die einer integrierten Luminosität von  $\mathcal{L} = 1.03 \text{ fb}^{-1}$  entsprechen, werden insgesamt  $7148 \pm 97$   $B_s^0 \rightarrow J/\Psi\pi^+\pi^-$  Signalkandidaten gefunden, mit denen die Phase  $\phi_s$  zu

$$\phi_s = -0.074 \pm 0.177 \text{ (stat)} \pm 0.015 \text{ (syst) rad}$$

bestimmt wird. Dieser Wert steht hervorragend mit der Vorhersage des Standardmodells von  $\phi_s^{SM} = (-0.0363^{+0.0016}_{-0.0015}) \text{ rad}$  [20] überein.



# Contents

<b>1</b>	<b>Introduction</b>	<b>1</b>
<b>2</b>	<b>Theory</b>	<b>3</b>
2.1	Standard Model of Particle Physics	3
2.1.1	Elementary Particles	3
2.1.2	Flavour Physics	4
2.1.3	Mixing of neutral B-mesons	6
2.1.4	CP-violation	9
2.1.5	CP-violating phase $\phi_s$ in the decay $B_s^0 \rightarrow J/\Psi\pi^+\pi^-$	11
2.2	Beyond the Standard Model contributions to B mixing	13
<b>3</b>	<b>The LHCb experiment</b>	<b>14</b>
3.1	Large Hadron Collider	14
3.2	LHCb-experiment	15
3.2.1	Track reconstruction	16
3.2.2	Ring Imaging Cherenkov Detector	18
3.2.3	Calorimeter System	18
3.2.4	Muon chambers	18
3.2.5	Particle identification	18
3.2.6	Event reconstruction	19
<b>4</b>	<b>Analysis Strategy</b>	<b>21</b>
<b>5</b>	<b>Signal selection and background</b>	<b>23</b>
5.1	Definition of event reconstruction variables	23
5.2	Reconstruction and Selection of the decay $B_s^0 \rightarrow J/\Psi\pi^+\pi^-$	24
5.2.1	$J/\Psi$ reconstruction	24
5.2.2	$\pi^+\pi^-$ resonance reconstruction	25
5.2.3	$B_s^0$ reconstruction	25
5.3	Fully simulated samples of signal decays and potential background decays	26
5.3.1	Signal decays	26
5.3.2	Potential background decays	27
5.4	Mass distributions of the selected $B_s^0 \rightarrow J/\Psi\pi^+\pi^-$ candidates obtained from data	29
5.5	Signal and background modeling for the selected $B_s^0$ candidates	31
5.6	Determination of the spin of the $\pi^+\pi^-$ states in the mass peak region of the $f_0(980)$	36
<b>6</b>	<b>Time Resolution</b>	<b>41</b>

6.1	Validation of the method on simulated events . . . . .	41
6.2	Time Resolution on data . . . . .	45
6.2.1	Average time resolution . . . . .	47
6.2.2	Per event time resolution . . . . .	48
<b>7</b>	<b>Determination of the time acceptance correction</b>	<b>50</b>
7.1	Comparison of $B_s^0 \rightarrow J/\Psi f_0(980)$ and $B^0 \rightarrow J/\Psi K^*(892)$ time acceptance in simulated data . . . . .	51
7.2	Determination of the time acceptance using $B^0 \rightarrow J/\Psi K^*(892)$ decays in data . . . . .	53
<b>8</b>	<b>Proper time description of the background</b>	<b>56</b>
8.1	Proper time distributions of background events . . . . .	56
8.2	Determination of the proper time shape of the background . . . . .	57
<b>9</b>	<b>Determination of the initial <math>B_s^0</math> production flavour</b>	<b>61</b>
9.1	Calibration of the $B_s^0$ production flavour determination . . . . .	62
<b>10</b>	<b>Determination of the phase <math>\phi_s</math></b>	<b>64</b>
10.1	Maximum Likelihood Fit . . . . .	64
10.2	Signal description . . . . .	65
10.2.1	Mass description . . . . .	65
10.2.2	Proper time dependence . . . . .	66
10.3	Background description . . . . .	67
10.3.1	Mass description . . . . .	67
10.3.2	Proper time dependence . . . . .	67
10.4	Proper time resolution . . . . .	68
10.5	Proper time acceptance . . . . .	68
10.6	Correct treatment of the per event uncertainties $\omega_{tag}$ and $\sigma_{ct}$ . . . . .	68
10.7	Validation of the fitting procedure . . . . .	69
10.8	Results . . . . .	71
<b>11</b>	<b>Estimation of Systematic Uncertainties</b>	<b>74</b>
<b>12</b>	<b>Summary and Conclusion</b>	<b>76</b>
	<b>Bibliography</b>	<b>78</b>

# 1 Introduction

For decades, the Standard Model of Particle Physics has been very successful in explaining the physics at quantum scale and predicting the observations of particle physics experiments. However, it can be shown that the theory becomes insufficient to describe high energy scales. The Large Hadron Collider (LHC) in Geneva, the world's largest accelerator is designed to reach these energies that have never been observed before. It allows to test the limits of the Standard Model and theoretical predictions of new theories and answers open questions of Particle Physics and Cosmology.

The LHCb experiment, one of the four experiments at the LHC, is designed to study the different behaviour of particles and anti-particles in the decays of B- and D-mesons. Precisely studying CP violation in rare decays can give indirect evidence for New Physics beyond the Standard Model that might explain the large excess of matter observed in the universe.

One key goal of LHCb is the determination of the CP-violating phase  $\phi_s$  in the channel  $B_s^0 \rightarrow J/\Psi\phi$  in which the  $B_s^0$  meson can oscillate into its anti-particle before decaying. Time-dependent CP violation arises from the interference between the direct decay and the decay after mixing. Since Flavour mixing in the Standard Model is an effect of higher order loop corrections, the phase  $\phi_s$  is very sensitive to new heavy degrees of freedom contributing to the loop corrections. The mass scale of the New Physics contributions can be much higher than the  $B_s^0$  meson mass.

For the measurement of the CP violation of the channel  $B_s \rightarrow J/\Psi\phi$ , a major complexity arises because the final state is an interference of CP-eigenstates that depend on the relative angular momenta of the final state particles. These states have to be separated in an angular analysis on a statistical basis. After conducting the first measurements at LHCb, the decay channel  $B_s^0 \rightarrow J/\Psi f_0(980)(\rightarrow \pi^+\pi^-)$  was observed that exhibits a branching ratio relative to  $B_s^0 \rightarrow J/\Psi\phi$  of about 20 % [37]. Due to the spin 0 of the  $f_0(980)$ , the final state is a pure CP-eigenstate which makes an angular analysis unnecessary and simplifies the determination of  $\phi_s$ . When enlarging the allowed mass region of the  $\pi^+\pi^-$  final states and including the spin-0 resonances  $f_0(1370)$  and  $f_0(1500)$  and the spin-2 resonances  $f_2(1270)$  and  $f_2'(1525)$ , the final state is still an almost pure CP-eigenstate [37] but the statistics is doubled. The analysis of these  $B_s^0 \rightarrow J/\Psi\pi^+\pi^-$  decays has been done in [40] and a phase of  $\phi_s = -0.019_{-0.174-0.003}^{+0.173+0.004}$  rad is obtained.

This thesis repeats the measurement of [40] using an independent analysis approach and provides the first cross-check measurement on the same 2011 data set. The selection of the data varies slightly from [40] and the fitting procedure has been independently developed by the Heidelberg LHCb group.

The thesis is structured as follows. In chapter 2, the Standard Model is introduced that provides the theoretical framework of Particle Physics. CP-violation in  $B_s^0 \rightarrow J/\Psi\pi^+\pi^-$  decays is described in detail. Chapter 3 covers the description of the LHCb-experiment and its detector components and chapter 4 presents the strategy how to perform the analysis. In chapter

5, the reconstruction and selection of the signal decays is shown and possible background contributions are investigated. In chapters 6 and 7, the proper time resolution and the time acceptance that have to be accounted for are determined. Chapter 8 analyzes the proper time dependence of the background candidates. Chapter 9 summarizes how the initial production flavour of the  $B_s^0$  candidate is determined. In chapter 10, the fitting procedure is described and applied on the data to determine  $\phi_s$  before the systematic uncertainties are discussed in chapter 11. Chapter 12 summarizes the results of the analysis and gives an overview of the current and the future expected measurements.

# 2 Theory

This chapter gives a short summary of the Standard Model that provides the theoretical description of Particle Physics. After giving a short overview of the basic ingredients, the section will focus on the CKM-mechanism for the quark flavours, which is responsible for quark mixing and leads to effects, such as the particle - anti-particle oscillation for neutral mesons. The introduction of a complex mixing phase  $\phi_s$  gives rise to time-dependent CP violation due to the interference between the direct decay and the decay after mixing of the  $B_s^0$ -mesons. CP-violation in  $B_s^0 \rightarrow J/\Psi\pi^+\pi^-$  decays, the channel that is subject of this analysis, is presented in detail.

## 2.1 Standard Model of Particle Physics

The Standard Model of Particles is a theory that attempts to describe the fundamental particles and their interactions.

### 2.1.1 Elementary Particles

The fundamental particles can be divided into two groups, the fermions with spin  $\frac{1}{2}$  that make up matter and the spin-1 gauge bosons that mediate the fundamental forces between them. Every fermion has an anti-particle that is subject to the same physical processes but has the opposite electric charge. According to the interactions between them, the fermions can be classified as quarks and leptons, and further, into three generations or families. The quarks and leptons are presented in table 2.1. The quarks with an electric charge of  $+\frac{2}{3} e$  are referred to as up-type quarks while the quarks with charge  $-\frac{1}{3} e$  are called down-type quarks. The properties are taken from [2] and the quark masses given denote the current mass of the quark itself in contrast to the constituent mass when quarks form hadrons. Since quarks do not appear as free particles, the current mass is only imprecisely known.

generation	Quarks			Leptons		
	type	charge[e]	mass	type	charge[e]	mass
I	u	$+\frac{2}{3}$	1.8 - 3.0 MeV	e	-1	511 keV
	d	$-\frac{1}{3}$	4.5 - 5.5 MeV	$\nu_e$	0	< 2 eV
II	c	$+\frac{2}{3}$	$1.275 \pm 0.025$ GeV	$\mu$	-1	105.7 MeV
	s	$-\frac{1}{3}$	$95 \pm 5$ MeV	$\nu_\mu$	0	< 2eV
III	t	$+\frac{2}{3}$	$173.5 \pm 0.6$ GeV	$\tau$	-1	1777 MeV
	b	$-\frac{1}{3}$	4.15 - 4.68 GeV	$\nu_\tau$	0	< 2eV

**Table 2.1:** The fermions of the Standard Model (taken from [2])

The gauge bosons are the photon  $\gamma$ , the 8 gluons, the  $W^+/W^-$  bosons and the  $Z^0$  boson. The photon, coupling to the electric charge, is the carrier of the electromagnetic interaction while the gluons mediate the strong interaction and couple to the colour charge. Since the gluons exhibit colour charges themselves, they can even couple to other gluons. The weak interaction is mediated by the charged  $W^+/W^-$  and the neutral  $Z^0$  bosons that couple to the weak charge. With the recent discovery of a Higgs-like particle in [41], which through its coupling generates the particle masses, the particle spectrum of the Standard Model is complete. The gauge boson properties are listed in table 2.2.

type	charge[e]	mass	couples to
photon $\gamma$	0	0	electric charge
8 gluons	0	0	colour charge
$W^\pm$	$\pm 1$	80.39 GeV	weak charge
$Z^0$	0	91.19 GeV	weak charge

**Table 2.2:** The gauge bosons of the Standard Model (taken from [2])

### 2.1.2 Flavour Physics

The weak interaction is the only fundamental force that can describe decays in which the flavour of the quarks is changed through the exchange of a  $W^\pm$  boson. The quark mixing is the result of the quark mass eigenstates  $|q\rangle$  not being equal to the electroweak eigenstates  $|q'\rangle$ . The electroweak eigenstates are constructed by rotating the mass eigenstates with the Cabbibo-Kobayashi-Maskawa(CKM) matrix  $V_{CKM}$  first described in [3]:

$$\begin{pmatrix} d' \\ s' \\ b' \end{pmatrix} = V_{CKM} \begin{pmatrix} d \\ s \\ b \end{pmatrix}, \quad (2.1)$$

Due to charge conservation, the transitions between the mass eigenstates can only occur from an up-type to a down-type quark and vice versa. The probability that a quark with mass eigenstate  $j$  decays into a quark mass eigenstate  $i$  is proportional to  $|V_{ij}|^2$ :

$$V_{CKM} = \begin{pmatrix} V_{ud} & V_{us} & V_{ub} \\ V_{cd} & V_{cs} & V_{cb} \\ V_{td} & V_{ts} & V_{tb} \end{pmatrix}. \quad (2.2)$$

The complex CKM-matrix has 18 parameters. Since  $V_{CKM}$  is a unitary matrix, this number is reduced to 9. 5 of these are relative phases and irrelevant for the measurable quantities. The remaining parameters are three mixing angles  $\Theta_{12}$ ,  $\Theta_{13}$  and  $\Theta_{23}$  and the phase  $\delta$ . Denoting the cosines and the sines of the angles as  $c_i$  and  $s_i$ ,  $i = 12, 13, 23$ ;  $V_{CKM}$  becomes

$$V_{CKM} = \begin{pmatrix} 1 & 0 & 0 \\ 0 & c_{23} & s_{23} \\ 0 & -s_{23} & c_{23} \end{pmatrix} \begin{pmatrix} c_{13} & 0 & s_{13}e^{-i\delta} \\ 0 & 1 & 0 \\ -s_{13}e^{i\delta} & 0 & c_{13} \end{pmatrix} \begin{pmatrix} c_{12} & s_{12} & 0 \\ -s_{12} & c_{12} & 0 \\ 0 & 0 & c_{13} \end{pmatrix} \quad (2.3)$$

$$= \begin{pmatrix} c_{12}c_{13} & s_{12}c_{13} & s_{13}e^{-i\delta} \\ -s_{12}c_{23} - c_{12}s_{23}e^{i\delta} & c_{12}c_{23} - s_{12}s_{23}s_{13}e^{i\delta} & s_{23}c_{13} \\ s_{12}s_{23} - c_{12}c_{23}s_{13}e^{i\delta} & -c_{12}s_{23} - s_{12}c_{23}s_{13}e^{i\delta} & c_{23}c_{13} \end{pmatrix}. \quad (2.4)$$

Since this parameterisation is complicated and does not reflect the hierarchy of the matrix elements, Lincoln Wolfenstein proposed a different parameterisation in [4] that expresses the parameters according to their absolute values in expansions of a small parameter  $\lambda$ :

$$s_{12} = \lambda \quad (2.5)$$

$$s_{23} = A\lambda^2 \quad (2.6)$$

$$s_{13}e^{-i\delta} = A\lambda^3(\rho - i\eta), \quad (2.7)$$

where  $\lambda$ ,  $A$ ,  $\rho$  and  $\eta$  are the four new parameters. The CKM-matrix takes the form:

$$V_{CKM} = \begin{pmatrix} 1 - \frac{\lambda^2}{2} - \frac{\lambda^4}{8} & \lambda & A\lambda^3(\rho - i\eta) \\ -\lambda & 1 - \frac{\lambda^2}{2} - \frac{\lambda^4}{8}(1 + 4A^2) & A\lambda^2 \\ A\lambda^3(1 - \rho - i\eta) & -A\lambda^2 + \frac{1}{2}A\lambda^4(1 - 2(\rho + i\eta)) & 1 - \frac{1}{2}A^4\lambda^4 \end{pmatrix}. \quad (2.8)$$

It expresses the relative values of the matrix elements very well. Since the measured values of  $\lambda$  and  $A$  are approximately 0.23 and 0.82 [2], the diagonal elements are close to 1. The small off-diagonal elements are of the order of  $\lambda^2$  respectively  $\lambda^3$ .

Unitarity of the CKM-matrix gives six equations for the off-diagonal elements of  $V_{CKM}V_{CKM}^\dagger = 1$ , where three of them are only conjugated complex equations of the others:

$$V_{ud}V_{us}^* + V_{cd}V_{cs}^* + V_{td}V_{ts}^* = 0 \quad (2.9)$$

$$V_{us}V_{ub}^* + V_{cs}V_{cb}^* + V_{ts}V_{tb}^* = 0 \quad (2.10)$$

$$V_{ud}V_{ub}^* + V_{cd}V_{cb}^* + V_{td}V_{tb}^* = 0. \quad (2.11)$$

$$(2.12)$$

The relations represent triangles in the complex plane with one corner at the vertex (0,0). Taking the second equation and normalising it by dividing by the side  $V_{cs}V_{cb}^*$  results in

$$\frac{V_{us}V_{ub}^*}{V_{cs}V_{cb}^*} + \frac{V_{ts}V_{tb}^*}{V_{cs}V_{cb}^*} = 0. \quad (2.13)$$

The associated unitarity triangle is shown in figure 2.1 where  $(\bar{\rho}_s, \bar{\eta}_s)$  marks the triangle's apex.

The angles between two numbers in the complex plane can be computed as the argument of the division of the two. For this analysis, the angle  $\beta_s$  is relevant:

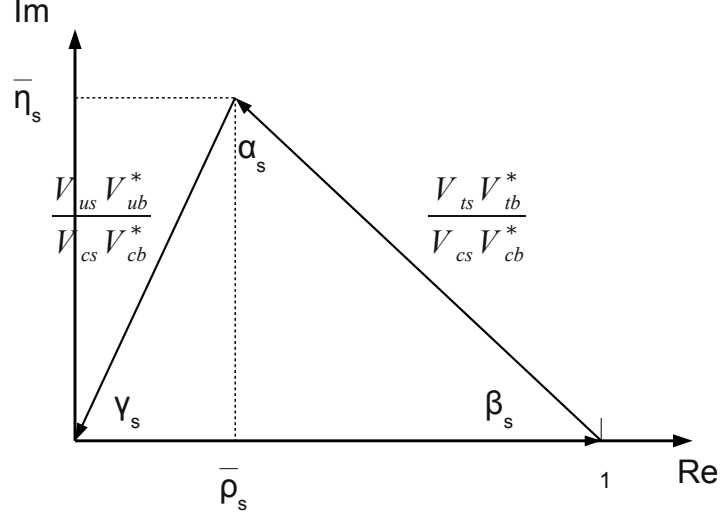


**Figure 2.1:**  $B_s^0$  Unitarity triangle of the CKM-matrix with normalised base

$$\beta_s \equiv \arg \left( -\frac{V_{ts} V_{tb}^*}{V_{cs} V_{cb}^*} \right). \quad (2.14)$$

The phase  $\phi_s$  that is subject to this analysis is defined as  $\phi_s = -2\beta_s$  and its Standard Model expectation value is  $\phi_s^{SM} = (-0.0363^{+0.0016}_{-0.0015}) \text{ rad}$  [20].

### 2.1.3 Mixing of neutral B-mesons

B mixing describes the possible transitions from one meson flavour state to the other via a flavour changing neutral current. Since these are not allowed on tree level, this process is only possible via a loop diagram shown in figure 2.2 in which W-bosons are exchanged.<sup>1</sup>

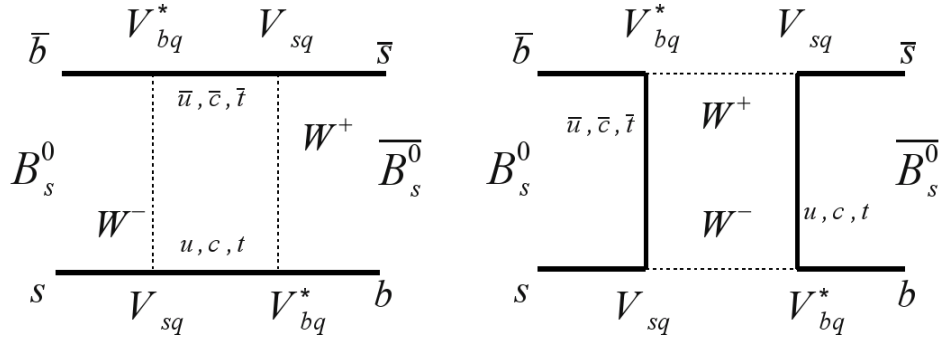


**Figure 2.2:**  $B_s^0$  mixing diagrams in the Standard Model

<sup>1</sup> The contributions from Penguin diagrams are neglected.

The total amplitude  $A$  of  $B_s^0$ -mixing is the sum of all possible quark transitions, where the sub-amplitudes  $A_q$  depend on the quark masses and the CKM matrix elements [6]:

$$A_q \propto (V_{qs}V_{qb}^*)^2 m_q^2/M_W^2. \quad (2.15)$$

Due to the Glashow-Iliopolous-Maiani (GIM) suppression in the limit of equal quark masses, the loop contribution is dominated by the heavy top quark and the mixing amplitude  $A$  is essentially proportional to  $V_{ts}V_{tb}^*$ .

The following derivation for the decay rates of the  $B_s^0$  flavour states is taken from [5], [6] and [8]. To determine the time-development of the flavour states  $|B_s^0\rangle$  and  $|\bar{B}_s^0\rangle$ , a phenomenological time-dependent Schrödinger equation can be written as

$$-\frac{\partial}{\partial t} \begin{pmatrix} |B_s^0\rangle \\ |\bar{B}_s^0\rangle \end{pmatrix} = \left( \mathbf{M} - \frac{i}{2}\mathbf{\Gamma} \right) \begin{pmatrix} |B_s^0\rangle \\ |\bar{B}_s^0\rangle \end{pmatrix} \quad (2.16)$$

with the mass matrix<sup>1</sup>  $\mathbf{M}$  and the decay matrix  $\mathbf{\Gamma}$  in the Hamiltonian. The off-diagonal elements of  $\mathbf{M}$  are non-zero when mixing is possible. The diagonal elements  $M_{11} = M_{22}$  denote the mass  $M$  and  $\Gamma_{11} = \Gamma_{22}$  denote the decay width  $\Gamma_s$  of the flavour state  $B_s^0$ .  $M_{12} = M_{21}^*$  and  $\Gamma_{12} = \Gamma_{21}^*$  are equal because of unitarity. Diagonalizing  $\mathbf{M} - \frac{i}{2}\mathbf{\Gamma}$  gives rise to two mass eigenstates, the light  $|B_L\rangle$  and the heavy  $|B_H\rangle$ :

$$\begin{aligned} |B_L\rangle &= p |B_s^0\rangle + q |\bar{B}_s^0\rangle \\ |B_H\rangle &= p |B_s^0\rangle - q |\bar{B}_s^0\rangle \end{aligned} \quad (2.17)$$

with  $|p|^2 + |q|^2 = 1$ . For the mass eigenstates, the Hamiltonian is diagonal and becomes  $\mathbf{M}_{L/H} - \frac{i}{2}\mathbf{\Gamma}_{L/H}$ . The diagonal elements are the masses  $M_{L/H}$  and the decay widths  $\Gamma_{L/H}$  so that the mass states develop in time with

$$\begin{aligned} |B_L\rangle(t) &= e^{-iM_L t} e^{-\frac{\Gamma_L}{2}t} |B_L\rangle \\ |B_H\rangle(t) &= e^{-iM_H t} e^{-\frac{\Gamma_H}{2}t} |B_H\rangle. \end{aligned}$$

The mass difference  $\Delta m_s$  and the difference  $\Delta\Gamma_s$  of the decay widths are defined as:

$$\Delta m_s = M_H - M_L \quad (2.18)$$

$$\Delta\Gamma_s = \Gamma_L - \Gamma_H, \quad (2.19)$$

where  $\Delta m_s > 0$  by definition and  $\Delta\Gamma_s$  can be positive or negative. They are related to the  $B_s^0$  mass  $M$  and width  $\Gamma_s$  by

<sup>1</sup> In this section, variables in bold refer to matrices and normal printed variables are scalars

$$M = \frac{M_H + M_L}{2} = M_L + \frac{\Delta m_s}{2} = M_H - \frac{\Delta m_s}{2} \quad (2.20)$$

$$\Gamma_s = \frac{\Gamma_L + \Gamma_H}{2} = \Gamma_H + \frac{\Delta \Gamma_s}{2} = \Gamma_L - \frac{\Delta \Gamma_s}{2}. \quad (2.21)$$

With equations 2.17 the flavour states can be written as

$$\begin{aligned} |B_s^0\rangle &= \frac{1}{2p}(|B_L\rangle + |B_H\rangle) \\ |\bar{B}_s^0\rangle &= \frac{1}{2q}(|B_L\rangle - |B_H\rangle). \end{aligned} \quad (2.22)$$

Inserting the time evolution of the mass eigenstates, this becomes

$$\begin{aligned} |B_s^0\rangle &= \frac{1}{2p} \left( e^{-iM_L t} e^{-\frac{\Gamma_L}{2} t} |B_L\rangle + e^{-iM_H t} e^{-\frac{\Gamma_H}{2} t} |B_H\rangle \right) \\ |\bar{B}_s^0\rangle &= \frac{1}{2q} \left( e^{-iM_L t} e^{-\frac{\Gamma_L}{2} t} |B_L\rangle - e^{-iM_H t} e^{-\frac{\Gamma_H}{2} t} |B_H\rangle \right). \end{aligned} \quad (2.23)$$

Inserting the mass eigenstates 2.17 in here with  $c = e^{-iM_L t} e^{-\frac{\Gamma_L}{2} t}$  and  $d = e^{-iM_H t} e^{-\frac{\Gamma_H}{2} t}$ ,

$$\begin{aligned} |B_s^0\rangle &= \frac{1}{2p} \left( p(c + d) |B_s^0\rangle + q(c - d) |\bar{B}_s^0\rangle \right) \\ |\bar{B}_s^0\rangle &= \frac{1}{2q} \left( p(c - d) |B_s^0\rangle + q(c + d) |\bar{B}_s^0\rangle \right). \end{aligned} \quad (2.24)$$

When the  $B_s^0$  decays into a final state  $f$ , the time-dependent decay rate  $\frac{d\Gamma(B_s^0 \rightarrow f)}{dt N_f}$  is the absolute square of the transition amplitude:

$$\frac{d\Gamma(B_s^0 \rightarrow f)}{dt N_f} = \left| \langle f | B_s^0 \rangle \right|^2. \quad (2.25)$$

For the computation, the absolute squares of sum and difference of  $c$  and  $d$  and mixed terms have to be calculated. Using equations 2.20 and 2.21, the sum is given here exemplary:

$$\begin{aligned} |c + d|^2 &= \left| e^{-iM_L t} e^{-\frac{\Gamma_L}{2} t} + e^{-iM_H t} e^{-\frac{\Gamma_H}{2} t} \right|^2 \\ &= e^{-\Gamma_L t} + e^{-\Gamma_H t} + e^{it(M_H - M_L)} e^{-\frac{t}{2}(\Gamma_L + \Gamma_H)} \\ &\quad + e^{it(M_L - M_H)} e^{-\frac{t}{2}(\Gamma_L + \Gamma_H)} \\ &= e^{-\Gamma_s t} \left( e^{-\frac{\Delta \Gamma_s}{2} t} + e^{\frac{\Delta \Gamma_s}{2} t} + e^{i\Delta m t} + e^{-i\Delta m t} \right) \\ &= e^{-\Gamma t} \left( 2 \cosh \frac{\Delta \Gamma_s}{2} t + 2 \cos(\Delta m t) \right), \end{aligned} \quad (2.26)$$

while the other products have a similar structure. Finally, the decay rates of  $B_s^0$  and  $\bar{B}_s^0$  are given by [6]:

$$\begin{aligned} \frac{d\Gamma(B_s^0 \rightarrow f)}{dtN_f} = & |A_f|^2 e^{-\Gamma_s t} \left\{ \frac{1 + |\lambda_f|^2}{2} \cosh \frac{\Delta\Gamma_s t}{2} + \frac{1 - |\lambda_f|^2}{2} \cos(\Delta m_s t) \right. \\ & \left. - \text{Re}\lambda_f \sinh \frac{\Delta\Gamma_s t}{2} - \text{Im}\lambda_f \sin(\Delta m_s t) \right\} \end{aligned} \quad (2.27)$$

and

$$\begin{aligned} \frac{d\Gamma(\bar{B}_s^0 \rightarrow f)}{dtN_f} = & |A_f|^2 \frac{1}{1-a} e^{-\Gamma_s t} \left\{ \frac{1 + |\lambda_f|^2}{2} \cosh \frac{\Delta\Gamma_s t}{2} - \frac{1 - |\lambda_f|^2}{2} \cos(\Delta m_s t) \right. \\ & \left. - \text{Re}\lambda_f \sinh \frac{\Delta\Gamma_s t}{2} + \text{Im}\lambda_f \sin(\Delta m_s t) \right\}, \end{aligned} \quad (2.28)$$

where  $\lambda_f = \frac{q}{p} \frac{\bar{A}_f}{A_f}$  with the decay amplitudes  $A_f = A(B_s^0 \rightarrow f)$  and  $\bar{A}_f = A(\bar{B}_s^0 \rightarrow f)$ ,  $a = 1 - \left| \frac{q}{p} \right|^2$  and  $N_f$  is a time-dependent normalisation factor. The decay rates into the final state  $\bar{f}$  are gained by substituting  $A_f$  by  $A_{\bar{f}}$  and  $\bar{A}_f$  by  $\bar{A}_{\bar{f}}$ .

#### 2.1.4 CP-violation

This section gives a short introduction to CP-violation. The CP operator is the consecutive application of charge conjugation (C) and parity (P) where charge conjugation converts a particle X into its anti-particle  $\bar{X}$  and P gives the parity  $\pi = \pm 1$  of the particle X:

$$P | X \rangle = \pi | X \rangle. \quad (2.29)$$

If a particle is identical to its anti-particle, the C-operator gives the C-eigenvalue  $\eta_C$ :

$$C | X \rangle = \eta_C | X \rangle, \quad (2.30)$$

where  $|\eta_C| = 1$ . For a CP-eigenstate  $| f_{CP} \rangle$ , the CP-operator gives the CP-eigenvalue  $\eta_{CP} = \eta_C \pi$ :

$$CP | f_{CP} \rangle = \eta_{CP} | f_{CP} \rangle. \quad (2.31)$$

If the CP-eigenvalue  $\eta_{CP}$  is +1, the CP-eigenstate is called CP-even. For  $\eta_{CP} = -1$ , the state is called CP-odd. Considering the system of two particles, the parity depends on the relative angular momentum  $l$ . Hence also the CP-eigenstate of a two particle state  $| f_{CP} \rangle$ :

$$CP | f_{CP} \rangle = \eta_{CP} (-1)^l | f_{CP} \rangle. \quad (2.32)$$

In 1964, it was discovered that CP symmetry is violated in decays of neutral Kaons [9].

However, there are three different types of CP-violation in the decays of a particle X into a final state f that are described in [6] and [8]. In the following, the notations  $\lambda_f = \frac{q}{p} \frac{\bar{A}_f}{A_f}$ , q and p are the same as above.

- **Direct CP violation**, often called CP violation in decay, is defined by

$$\left| \frac{\bar{A}_f}{A_f} \right| \neq 1 \quad (2.33)$$

and appears when the decay rates of the CP-conjugate processes  $X \rightarrow f$  and  $\bar{X} \rightarrow \bar{f}$  with particle X and final CP-eigenstate f are not equal. An example is the decays  $B^0 \rightarrow K^+ \pi^-$  and  $\bar{B}^0 \rightarrow K^- \pi^+$  reported in [10].

- **CP violation in mixing** of neutral mesons  $X^0$  and  $\bar{X}^0$  is defined by

$$\left| \frac{q}{p} \right| \neq 1, \quad (2.34)$$

That induces a difference between the transition probabilities  $\mathcal{P}(X^0 \rightarrow \bar{X}^0)$  and  $\mathcal{P}(\bar{X}^0 \rightarrow X^0)$  which this leads to an excess of particles of one flavour when assuming no direct CP violation but equal  $X^0$ - $\bar{X}^0$  production.

- **CP violation in interference** between the direct decay  $X^0 \rightarrow f_{CP}$ , and the decay after mixing,  $X^0 \rightarrow \bar{X}^0 \rightarrow f_{CP}$  as it is sketched in figure 2.3 is defined by

$$Im(\lambda_f) \neq 0. \quad (2.35)$$

This time-dependent CP violation is only possible when the final state  $f_{CP}$  is a CP-eigenstate and can be reached in the decay of  $X^0$  and  $\bar{X}^0$ . The final state can be formed by different CP-eigenstates.

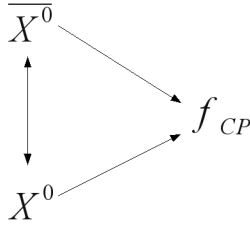


**Figure 2.3:** Illustration of CP violation in interference between the direct decay  $X^0 \rightarrow f_{CP}$ , and the decay after mixing,  $X^0 \rightarrow \bar{X}^0 \rightarrow f_{CP}$

In the decay  $B_s^0 \rightarrow J/\Psi \phi$  the final state is an admixture of different CP-eigenstates, where for the decay  $B_s^0 \rightarrow J/\Psi \pi^+ \pi^-$ , the final state is composed of a single CP-odd eigenstate.

### 2.1.5 CP-violating phase $\phi_s$ in the decay $B_s^0 \rightarrow J/\Psi \pi^+ \pi^-$

In the tree level diagram 2.4 of the decay  $B_s^0 \rightarrow J/\Psi \pi^+ \pi^-$ , the  $\bar{b}$ -quark of the  $B_s^0$  meson decays into a  $\bar{c}$ -quark by emitting a  $W^+$  boson. While the  $\bar{c}$ -quark hadronizes to become a  $J/\Psi$ , the  $s - \bar{s}$  final state forms a resonance that can decay into two pions. In [38], it is shown that the two pion system can only have even spin because of even G-parity of the  $s - \bar{s}$  system. Therefore, the expected  $\pi^+ \pi^-$  resonances in this analysis are the spin-0 mesons  $f_0(980)$ ,  $f_0(1370)$  and  $f_0(1500)$  and the spin-2 mesons  $f_2(1270)$  and  $f_2'(1525)$ . Spin-4 resonances do not appear in the selected mass region of the  $\pi^+ \pi^-$  system.

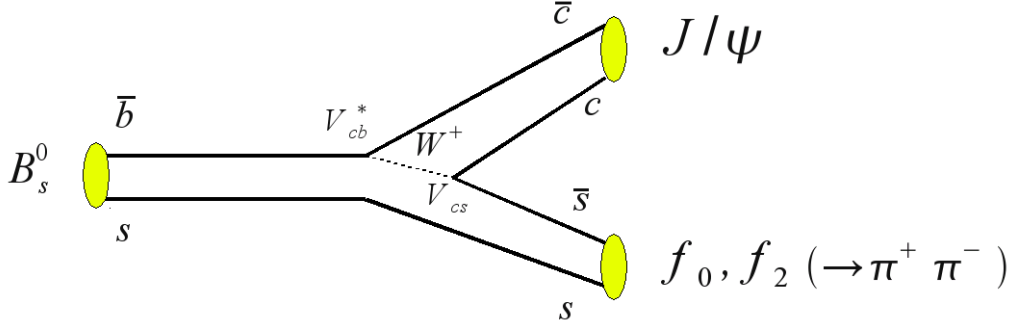


**Figure 2.4:** Tree level Feynman diagram of the decay  $B_s^0 \rightarrow J/\Psi f_0/f_2(\rightarrow \pi^+ \pi^-)$

The following derivation of the decay rate is taken from [6] and [7]. The decay amplitude  $A_{(J/\Psi \pi^+ \pi^-)}$  is proportional to the CKM matrix elements  $V_{cs}$  and  $V_{cb}^*$ . Assuming no direct CP violation, i.e.  $\left| \frac{\bar{A}_f}{A_f} \right|^2 = 1$ , the amplitude ratio  $\frac{\bar{A}_f}{A_f}$  is given by

$$\begin{aligned} \frac{\bar{A}_f}{A_f} &= -\eta_{(J/\Psi \pi^+ \pi^-)} \frac{V_{cb} V_{cs}^*}{V_{cb}^* V_{cs}} \\ &= -\eta_{(J/\Psi \pi^+ \pi^-)} e^{2i\phi_D} \end{aligned} \quad (2.36)$$

with the CP-eigenvalue  $\eta_{(J/\Psi \pi^+ \pi^-)}$  of the final state  $J/\Psi \pi^+ \pi^-$  and the weak phase of the decay  $\phi_D = \arg(V_{cb} V_{cs}^*)$ .

Assuming no CP violation in mixing, i.e.  $\left| \frac{q}{p} \right|^2 = 1$ , the ratio of  $q$  and  $p$  is given by

$$\begin{aligned} \frac{q}{p} &= -\frac{V_{ts} V_{tb}^*}{V_{ts}^* V_{tb}} \\ &= -e^{-i\phi_M}, \end{aligned} \quad (2.37)$$

where  $\phi_M = 2 \arg(V_{ts}^* V_{tb})$  is the  $B_s^0$  mixing phase that occurs in the mixing diagram in figure 2.2.

The quantity  $\lambda_f = \frac{q \bar{A}_f}{p A_f}$  is computed as

$$\begin{aligned} \lambda_f &= \eta_{(J/\Psi \pi^+ \pi^-)} e^{i(2\phi_D - \phi_M)} \\ &= \eta_{(J/\Psi \pi^+ \pi^-)} e^{-i\phi_s} \end{aligned} \quad (2.38)$$

with  $\phi_s = \phi_M - 2\phi_D = 2 \arg(V_{ts}^* V_{tb}) - 2 \arg(V_{cb} V_{cs}^*) = -2\beta_s$  where  $\beta_s = \arg(-V_{ts} V_{tb}^* / V_{cs} V_{cb}^*)$  is the angle in the unitarity  $B_s^0$  triangle defined in equation 2.14. The non-trivial imaginary part  $Im\lambda_f = -\eta_{(J/\Psi\pi^+\pi^-)} \sin \phi_s$  gives rise to time-dependent CP violation in interference between the direct decay and the decay after mixing. While the phases  $\phi_M$  and  $\phi_D$  are only chosen relative to each other,  $\phi_s$  is a measurable physical quantity.

### CP-eigenstate of the final state $J/\Psi\pi^+\pi^-$

In the decay  $B_s^0 \rightarrow J/\Psi f_0/f_2 (\rightarrow \pi^+\pi^-)$ , the spin-0  $B_s^0$  decays into the spin-1  $J/\Psi$  and the  $f_0$  or  $f_2$ . For conserving the initial spin  $\mathbf{J} = 0$ , the final state mesons need to have a relative angular momentum  $l$ .

If the final state  $\pi^+\pi^-$  has spin  $\mathbf{J} = 0$ , the only possibility is a relative angular momentum of  $l = 1$ . When a spin-2 state is produced, the variety of possible angular momenta is larger. If the  $J/\Psi$  and the pion system exhibit a z-projection of the spin  $J_z = 0$ , the spins  $\mathbf{J}_{J/\Psi} = 1$  and  $\mathbf{J}_{\pi^+\pi^-} = 2$  can combine according to the Clebsch-Gordan coefficients [2] to  $\mathbf{J}_{\text{combined}} = 1$  or 3 so that relative angular momenta  $l = 1$  or 3 are possible. If they exhibit an opposite  $J_z = \pm 1$ ,  $\mathbf{J}_{\text{combined}}$  and  $l$  can take the values 1, 2 or 3:

	$\mathbf{B}_s^0$	$\mathbf{J}/\Psi$	$\pi^+\pi^-$ system	possible $l$
$\mathbf{J}$	0	1	0	
$J_z$	0	0	0	1
$\mathbf{J}$	0	1	2	
$J_z$	0	0	0	1,3
$J_z$	0	$\pm 1$	$\mp 1$	1,2,3

**Table 2.3:** Possible spin contributions of the final state particles

The various relative angular momenta lead to different CP eigenstates of the final state. The CP-eigenvalue  $\eta_{(J/\Psi\pi^+\pi^-)}$  is computed as

$$\begin{aligned} \eta_{(J/\Psi\pi^+\pi^-)} &= \eta_{J/\Psi} \eta_{f_0/f_2} (-1)^l \\ &= (-1)^l \end{aligned} \quad (2.39)$$

with the CP-eigenvalues  $\eta_{J/\Psi} = 1$  and  $\eta_{f_0/f_2} = 1$ . Thus, for odd angular momenta, the CP-eigenstate is odd, while for even  $l$ , the eigenstate is even. In [37], it is shown that the CP-odd fraction of the final state in this decay is greater than 0.977 at 95 % confidence level with a small  $J_z = \pm 1$  contribution. This analysis therefore assumes a pure CP-odd eigenstate  $\eta_{(J/\Psi\pi^+\pi^-)} = -1$  of the final state  $J/\Psi\pi^+\pi^-$ .

### Time evolution of $B_s^0$ and $\bar{B}_s^0$ decaying into the CP-odd eigenstate $J/\Psi\pi^+\pi^-$

Inserting  $|\lambda_f|^2 = 1$ ,  $Re\lambda_f = -\cos \phi_s$  and  $Im\lambda_f = \sin \phi_s$  into the decay rates 2.27 and 2.28, the decay rate of  $B_s^0$  and  $\bar{B}_s^0$  into the CP-odd eigenstate  $J/\Psi\pi^+\pi^-$  is given by

$$\frac{d\Gamma(B_s^0 \rightarrow J/\Psi\pi^+\pi^-)}{dt N_f} = |A_f|^2 e^{-\Gamma_s t} \left\{ \cosh \frac{\Delta\Gamma_s t}{2} + \cos \phi_s \sinh \frac{\Delta\Gamma_s t}{2} - \sin \phi_s \sin(\Delta m_s t) \right\}$$

and

$$\frac{d\Gamma(\bar{B}_s^0 \rightarrow J/\Psi\pi^+\pi^-)}{dtN_f} = |A_f|^2 e^{-\Gamma_s t} \left\{ \cosh \frac{\Delta\Gamma_s t}{2} + \cos \phi_s \sinh \frac{\Delta\Gamma_s t}{2} + \sin \phi_s \sin(\Delta m_s t) \right\}.$$

Denoting  $q$  as the flavour of the  $B_s^0$  meson where  $q = 1$  refers to a  $B_s^0$  and  $q = -1$  for a  $\bar{B}_s^0$ , the two time evolutions can be written into one equation:

$$\frac{d\Gamma(B_s^{0(\pm)} \rightarrow J/\Psi\pi^+\pi^-)}{dtN_f} = |A_f|^2 e^{-\Gamma_s t} \left\{ \cosh \frac{\Delta\Gamma_s t}{2} + \cos \phi_s \sinh \frac{\Delta\Gamma_s t}{2} - q \sin \phi_s \sin(\Delta m_s t) \right\}.$$

## 2.2 Beyond the Standard Model contributions to B mixing

New Physics can be introduced by additional contributions to the loop diagram 2.2 of  $B_s^0$  mixing. Since the exchanged particles in the loop are only created virtually,  $B_s^0$  mixing is also sensitive to mass scales that are much higher than the actual  $B_s^0$  mass. New phenomena manifest themselves in changing the magnitude of the mixing phase  $\phi_M$ . As a consequence, the Standard Model expectation  $\phi_s^{SM} = (-3.68 \pm 0.17) \cdot 10^{-2}$  [19] gets shifted by an additional phase  $\phi_s^\Delta$  [19]:

$$\phi_s = \phi_s^{SM} + \phi_s^\Delta. \quad (2.40)$$

The direct sensitivity of  $\phi_s$  for additional New Physics contributions  $\phi_s^\Delta$  gives a strong incentive to determine  $\phi_s$  more precisely.

## 3 The LHCb experiment

In order to study the decay  $B_s^0 \rightarrow J/\Psi \pi^+ \pi^-$ , a large number of  $B_s^0$  mesons is needed. At the Large Hadron Collider (LHC), they are produced numerously in proton-proton collisions due to a large  $b\bar{b}$  cross section of  $\sim 284 \mu b$  [42] expected at an energy of 7 TeV. The LHCb detector, located at one of the interaction points, has the excellent vertex and momentum resolution that is needed to study the rapidly oscillating  $B_s^0$  mesons.

### 3.1 Large Hadron Collider

The Large Hadron Collider (LHC) at CERN is a gigantic ring accelerator that is designed to collide proton beams with a maximum center of mass energy of 14 TeV and a luminosity of  $\mathcal{L} = 10^{34} \text{cm}^{-2} \text{s}^{-1}$  [21]. The beam pipe tunnel is 27 kilometres in circumference and built between 45 and 170 m below the surface of the Swiss-French border near the town of Geneva. The collisions take place at four experimental points that are situated in huge underground caverns. A sketch of the tunnel and the interaction points is shown in figure 3.1 which is taken from [22].

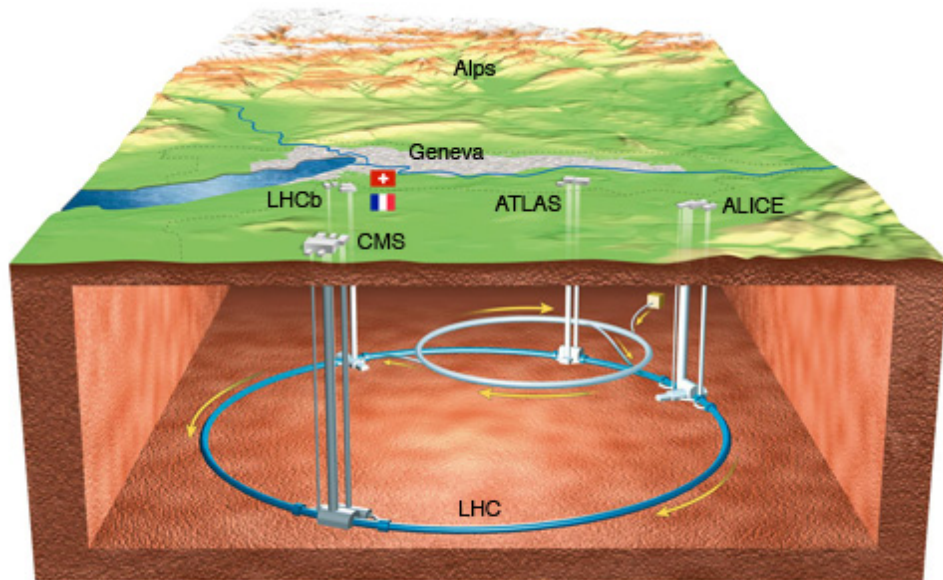


**Figure 3.1:** Schematic illustration of the LHC taken from [22]

ATLAS and CMS are multi-purpose experiments, ALICE is specialized to study heavy ion collisions and LHCb is designed to study B- and D-mesons.

## 3.2 LHCb-experiment

The LHCb experiment is designed to study heavy flavour physics at the LHC. In contrast to the larger experiments ATLAS and CMS, LHCb is operated at a lower luminosity of  $\mathcal{L} = 2 \cdot 10^{32} \text{cm}^{-2} \text{s}^{-1}$  by separating the colliding beams. The advantage of a lower interaction rate is to have only one or two proton-proton interaction per bunch crossing which simplifies the association of the Primary Vertices. Additionally, the occupancy in the detector is lower which reduces combinatorial background. Nevertheless, a number of  $10^{12} \text{ } b\bar{b}$  pairs are produced in  $10^7$  seconds that can be reached in a year of data taking. Due to the high center of mass energy of the protons, the B-hadrons are predominantly produced in the forward and backward direction. This is the reason why LHCb is built as a single-arm forward spectrometer. The angular coverage ranges from approximately 10 to 300 mrad in the bending plane and from 10 to 250 mrad vertical to the bending plane. This corresponds to a pseudorapidity  $\eta$  of approximately  $1.6 < \eta < 4.9$  [24]. A schematic illustration of the side view of the LHCb-detector is shown in figure 3.2 that is taken from [24].



**Figure 3.2:** Schematic illustration of the side view of the LHCb-detector taken from [24]. The proton-proton collision takes place on the left in the Vertex Locator (VELO); RICH1 and RICH2 are Cherenkov detectors; TT is the Trigger Tracker, T1 - T3 the main tracking system, SPD is the Scintillating Pad Detector and PS the Preshower detector; ECAL is the electromagnetic calorimeter, HCAL the hadronic calorimeter and M1 - M5 the muon chambers

In the right-handed coordinate system, the z-axis is equal to the beam axis and the y-axis is along the vertical of the cavern. The single parts are now only mentioned but they will be briefly discussed in the following sections. Most of the information about the detector is taken from a detailed detector description in [24].

- The proton-proton collision takes place on the left within the Vertex Locator (VELO), a silicon strip detector with excellent vertex resolution.
- The Ring Imaging Cherenkov counters (RICH1 and RICH2) are used to identify particles via Cherenkov radiation.

- The magnet provides an integrated field of 4 Tm to bend the charged particles in order to determine the momenta.
- The tracking system consists of a Trigger Tracker (a silicon microstrip detector, TT) in front of the magnet and three main tracking stations behind (T1 - T3). Their inner part with the highest detection rate, the Inner Tracker (IT), is made of silicon microstrips and the outer part, the Outer Tracker(OT) consists of a straw tube gas detector.
- The calorimeter system is used to measure the energy deposited by electromagnetic and hadronic showers but is also important to deliver trigger signals. It consists of a Scintillator Pad and a Preshower (SPD/PS) detector and an electromagnetic (shashlik type) calorimeter (ECAL) followed by a hadronic (Fe and scintillator tiles) calorimeter (HCAL).
- The muon detection system (M1 -M5) is composed of multi-wire proportional chambers (MWPC) and triple gas electron multipliers (GEM) in the region with the highest detection rate.

#### 3.2.1 Track reconstruction

The tracking system of the LHCb-detector is essential to reconstruct a decay signature, measure momenta and determine the proper time of a particle.

#### Vertex Locator (VELO)

Immediately close to the proton-proton interaction point, the first detector is a silicon strip detector called the Vertex Locator(VELO). It consists of 25 disk-shaped silicon modules, each measuring the radial  $r$  and azimuthal  $\phi$  coordinates of the particle tracks with a minimal pitch of  $38 \mu m$  [28]. They are arranged along the beam pipe because the relevant mesons are produced with high longitudinal momenta. A picture of one half of the VELO is given in figure 3.3 that is taken from [22].

During the nominal run, the two VELO halves are moved together and approach the nominal beam axis up to a distance of 5 mm [28] with the sensitive area starting at a radius of 8 mm. During the injection of the proton bunches into the LHC, the VELO halves can be moved 6 cm apart from the center to protect them from the beam. The excellent vertex resolution is used to resolve the proton-proton interaction point, the primary vertex and the displaced secondary decay vertices that are a characteristic feature of the B- and D-mesons. A track in the angular acceptance of 300 mrad in the bending plane will cross at least three sensors.

#### Magnet

A normal conducting dipole magnet with saddle-shaped coils is used to bend charged particles and determine their momenta. The integrated magnetic field of 4 Tm extends over 10 m along the beam axis. The magnetic field can be adjusted to point up- or downwards in order to investigate acceptance effects related to the bending of the tracks.

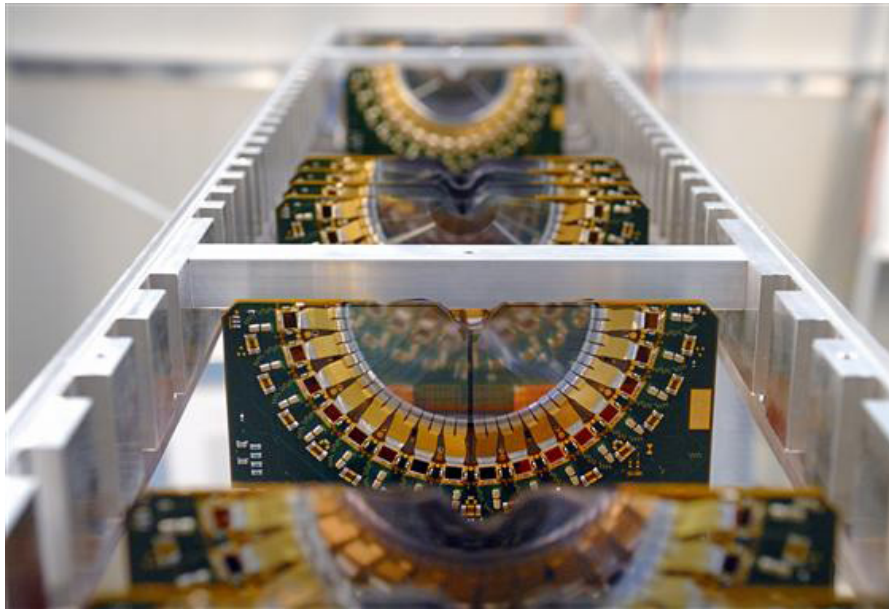


**Figure 3.3:** One half of the Vertex Locator(VELO) disks taken from [22]

### Tracking Stations

The Tracker Turicensis (TT) in front of the magnet and the Inner Tracker (IT), the inner part of the main tracking system behind the magnet both use silicon microstrip sensors that exhibit a very high detection rate. They consist of four layers grouped in two pairs with two vertical x-layers and two layers that are rotated by  $\pm 5^\circ$  to the vertical axis. This structure is called a x-u-v-x geometry and enables 2-dimensional spatial resolution. The silicon strip sensors exhibit a pitch of  $198 \mu\text{m}$  [30] and the spatial resolution of both trackers is about  $50 \mu\text{m}$  [24].

The Outer Tracker (OT) located behind the magnet covers the outer acceptance with an area of  $6 \times 5 \text{ m}$ . Since the particle multiplicity here is lower, it is built from straw-tube drift chamber modules with a mixture of Argon and  $\text{CO}_2$ . The layers are as well arranged in a x-u-v-x geometry and exhibit a maximum drift time of approximately 45 ns which enables to distinguish consecutive proton bunch collisions. A spatial resolution of  $200 \mu\text{m}$  [24] along the x-axis can be achieved for single cells.

A particle track originating from the proton-proton interaction leaves hits in the different tracking detectors. After the pattern recognition to identify the hits belonging to a specific track, the hits are fit using Kalman-filter algorithms [24] which account for multiple scattering of the particle. The quality of the track reconstruction can be estimated by computing the reduced track fit  $\chi^2$ , i.e.  $\chi^2/nDof$ . It is called the track  $\chi^2/nDof$ . Tracks that have been detected in the VELO and the tracking stations exhibit a momentum resolution of  $\delta p/p = 0.35 \%$  [24] for low momentum tracks and  $\delta p/p = 0.55 \%$  [24] for tracks at the high end of the spectrum.

### 3.2.2 Ring Imaging Cherenkov Detector

At LHCb, it is essential to distinguish pions and Kaons that are produced numerous in the decays of B- and D-mesons. The two Ring Imaging Cherenkov counters in front of and behind the magnet (RICH1 and RICH2) detect the Cherenkov radiation that is emitted when charged particles traverse a dense medium with the refractive index  $n$ . This happens when the velocity  $v = \beta c$  is larger than the light velocity  $c' = \frac{c}{n}$  in the medium. The Cherenkov radiation [27] is emitted in a cone of an angle  $\theta$  around the flight direction of the particle:

$$\cos \theta = \frac{c'}{v} = \frac{1}{n\beta}$$

The velocity  $\beta c$  can be determined by measuring the angle  $\theta$ . By comparing the measured momentum and the velocity of the particle, the particle's mass and furthermore the particle type can be determined. RICH 1 uses aerogel and  $C_4F_{10}$  radiators [26] that cover the low momentum range from  $\sim 1 - 60$  GeV/c while the upstream RICH 2 covers the momentum range from  $\sim 15 - 100$  GeV/c with a  $CF_4$  radiator [24]. The average efficiency for Kaon identification is 95% with a pion-as-Kaon misidentification rate of 5% [24].

### 3.2.3 Calorimeter System

Electrons and photons produce electromagnetic showers via bremsstrahlung and  $e^+e^-$ -pair production in the absorber material of the electromagnetic calorimeter while hadrons cause a hadronic shower in the hadronic calorimeter<sup>1</sup>. The calorimeters use plates of absorber interleaved with plates of plastic scintillator read-out by photomultipliers to detect the shower particles. Apart from the measurement of the deposited energy of a particle, the main purpose of the LHCb calorimeter system is to deliver trigger signals from high  $p_T$  photons, electrons and hadrons. The actual electromagnetic calorimeter (ECAL) consists of lead and scintillating layers and has an energy resolution of  $\sigma_E/E = 10\%/\sqrt{E} \oplus 1\%$  (E in GeV) [24]. It is followed by a hadronic calorimeter (HCAL) made of iron and scintillator tiles. Its resolution is  $\sigma_E/E = (69 \pm 5)\%/\sqrt{E} \oplus (9 \pm 2)\%$  (E in GeV) [24].

### 3.2.4 Muon chambers

The muon chambers are used to identify muons. Although, most of the other particles are absorbed in the calorimeter system and do not reach the muon chambers, the stations M2 to M5 are interleaved with additional 80 cm thick iron absorbers [29] which can only be penetrated by muons. Besides for the inner part of M1, multi-wire proportional chambers (MWPC) are used. The time to collect the signal is less than 20  $\mu s$  with an efficiency larger than 95 % [24]. Considering also the angular acceptance of the detector, about 20 % of the muons produced in semileptonic b decays are detected in the muon chambers.

### 3.2.5 Particle identification

The information provided by the two RICH detectors, the calorimeters and the muon chambers is combined to a particle hypothesis in the form of a likelihood  $\mathcal{L}(\pi, \mu \text{ or } K)$ . Since pions

---

<sup>1</sup> and in the electromagnetic calorimeter

are produced most frequently in the proton-proton collisions, the difference of the logarithmic likelihood for a particle X and a pion are computed as the relative particle hypothesis

$$\Delta \ln \mathcal{L}_{X-\pi} = \ln \mathcal{L}(X) - \ln \mathcal{L}(\pi). \quad (3.1)$$

This variable can be used to separate particles X from pions.

### 3.2.6 Event reconstruction

The information provided by the detector components is used to reconstruct the event and the relevant decays like  $B_s^0 \rightarrow J/\Psi \pi^+ \pi^-$ . The 4-momentum vector  $P$  of a particle consists of the energy  $E = \sqrt{m^2 + \vec{p}^2}$  and the 3-momentum vector  $\vec{p}$ . Since the masses  $m$  of the decay products are not directly measured, the corresponding values of the PDG [2] are assigned as the particle masses according to the particle hypothesis. Thus, the resulting 4-momentum is computed as<sup>1</sup>

$$\begin{aligned} P &= (E, \vec{p}) \\ &= \left( \sqrt{m_{PDG}^2 + \vec{p}^2}, \vec{p} \right). \end{aligned} \quad (3.2)$$

A large fraction of the pions, Kaons and muons are produced directly at the proton-proton interaction point. This vertex is reconstructed as the primary vertex (PV).

To reconstruct the decay  $B_s^0 \rightarrow J/\Psi \pi^+ \pi^-$ , the tracks of the decay products of the  $J/\Psi$ , the two muons are used to reconstruct the decay vertex of the  $J/\Psi$ .<sup>2</sup> The tracks of the two pions are combined to reconstruct the vertex of the  $\pi^+ \pi^-$  resonance  $f_0$  or  $f_2$ .<sup>3</sup>

The quality of the vertex reconstruction fit is described by the reduced vertex fit  $\chi^2$ , i.e. the  $\chi^2/nDof$ . This quantity is called the vertex  $\chi^2/nDof$ .

Since the  $J/\Psi$  and the  $f_0/f_2$  decay via the electromagnetic respectively the strong interaction, their lifetimes are so short that they seem to decay immediately. Thus, the combined vertices are used to reconstruct the decay vertex (DV) of the  $B_s^0$  meson as it is sketched in figure 3.4.<sup>4</sup>

Denoting  $\vec{d}_{pr}$  as the determined primary vertex,  $\vec{d}_{decay}$  as the decay vertex and  $d = \left| \vec{d}_{decay} - \vec{d}_{pr} \right|$  as the  $B_s^0$  flight distance with the velocity<sup>5</sup>  $\beta$ , and  $\gamma = 1/\sqrt{1 - \beta^2}$  as in special relativity theory, the proper time  $t_{prop}$  of the  $B_s^0$  can be computed as [38]

1 in natural units

2 The 4-momentum vector  $P_{J/\Psi}$  is calculated as the sum of the muon 4-momenta  $P_{J/\Psi} = P_{\mu^+} + P_{\mu^-}$ .

3 The 4-momentum vector  $P_{f_0/f_2}$  is calculated as the sum of the pion 4-momenta  $P_{f_0/f_2} = P_{\pi^+} + P_{\pi^-}$ .

4 The  $B_s^0$  4-momentum is the sum of  $J/\Psi$  - and  $f_0/f_2$  4-momentum  $P_{B_s^0} = P_{J/\Psi} + P_{f_0/f_2}$ .

5 in natural units

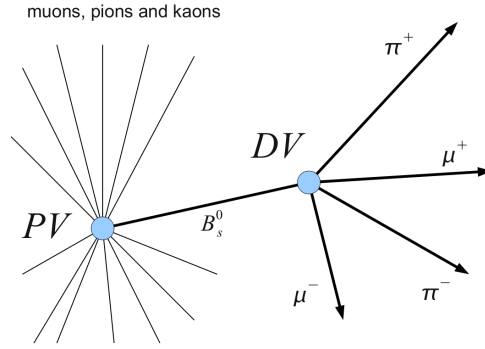


**Figure 3.4:** Illustration of the reconstruction of the decay  $B_s^0 \rightarrow J/\Psi \pi^+ \pi^-$

$$\begin{aligned}
 t_{prop} &= \frac{d}{\gamma v} \\
 \Leftrightarrow t_{prop} &= \frac{d}{\gamma \beta} = \frac{d \sqrt{1 - \beta^2}}{\beta} \\
 \Leftrightarrow t_{prop} &= d \sqrt{\frac{1}{\beta^2} - 1} = d \sqrt{\left(\frac{E}{p}\right)^2 - 1} \\
 \Leftrightarrow t_{prop} &= \frac{d}{p} \sqrt{E^2 - p^2} = \frac{md}{p} = \frac{m \vec{d} \cdot \vec{p}}{|\vec{p}|^2} \\
 \Leftrightarrow t_{prop} &= \frac{m(\vec{d}_{decay} - \vec{d}_{pr}) \cdot \vec{p}}{|\vec{p}|^2}
 \end{aligned}$$

(3.3)

## 4 Analysis Strategy

This analysis aims to measure the CP-violating phase  $\phi_s$  in  $B_s^0 \rightarrow J/\Psi\pi^+\pi^-$  decays which is an almost pure CP-odd eigenstate [37]. In the theory chapter 2, the time-dependent  $B_s^0$  signal partial decay rate  $d\Gamma/dt$  is given as an exponential decay function modulated by the  $B_s^0$ - $\bar{B}_s^0$  oscillation<sup>1</sup>:

$$\frac{d\Gamma(B_s^0 \rightarrow J/\Psi\pi^+\pi^-)}{dt} \propto e^{-\Gamma_s t} \left\{ \cosh \frac{\Delta\Gamma_s t}{2} + \cos \phi_s \sinh \frac{\Delta\Gamma_s t}{2} - q \sin \phi_s \sin(\Delta m_s t) \right\}.$$

In order to determine  $\phi_s$ , this function has to be fitted to the measured proper time distribution of the  $B_s^0$  signal candidates. The measurement is performed in the following steps:

- The collected data has to be separated into relevant signal and background decays. During proton-proton collisions, the amount of particles that are created at the interaction point is very large and it is important to select the relevant decays. The sources of background can be investigated by comparing the mass distribution of the selected  $B_s^0$  candidates with the mass distributions of simulated decays.
- It has to be shown that the CP-eigenstate of the final state is odd. Since it depends on the spin of the decay products, the various spin contributions have to be investigated in an angular analysis.
- Due to the selection process, the measured time-dependent decay rate deviates from expectation. The *proper time acceptance* describes the efficiency of selecting the signal decays as a function of the proper time and has to be determined and correctly applied in the fit.
- To resolve the  $B_s^0$ - $\bar{B}_s^0$  oscillation in time, the initial production flavour  $q$  of the reconstructed  $B_s^0$  must be determined. This information is provided by tagging algorithms. Since this is not perfect, the observable oscillation amplitude gets diluted. This tagging dilution has to be determined.
- $\sin(\phi_s)$  is determined by measuring the amplitude of the  $B_s^0$ - $\bar{B}_s^0$  oscillation. The proper time can only be measured with a certain resolution which also leads to a dilution of the amplitude of the oscillation term. It is therefore necessary to exactly know how well the proper time can be measured. The *time resolution* of the detector has to be determined and correctly applied in the fit.

---

<sup>1</sup>  $\Gamma_s$  is the decay width of the  $B_s^0$ ,  $\Delta\Gamma_s$  the difference of the widths of the light and heavy mass eigenstates and  $\Delta m_s$  is the mixing frequency.  $q$  denotes the flavour of the  $B_s^0$  meson:  $q = 1$  refers to a  $B_s^0$  and  $q = -1$  for a  $\bar{B}_s^0$ .

- The final determination of  $\phi_s$  is done using a 2-dimensional fit to the mass and proper time distribution of the  $B_s^0$  where the mass is used to separate the signal and background component. After obtaining the results, the systematic uncertainties are estimated.

## 5 Signal selection and background

The data sample used in this analysis corresponds to  $1.03 \text{ fb}^{-1}$  of integrated luminosity that was collected in 2011 at a center of mass energy of  $\sqrt{s} = 7 \text{ TeV}$ . In this chapter, the selection cuts are described to reconstruct the decay  $B_s^0 \rightarrow J/\Psi \pi^+ \pi^-$  where the  $J/\Psi$  decays into two muons. Using simulated decays as templates, the number of signal events, background B-decays and combinatorial background decays is determined. In the end, the spin contributions of the final state particles are investigated that are responsible for the CP-eigenstate.

### 5.1 Definition of event reconstruction variables

The basic tool to reconstruct a particular decay is to select only decay products with certain expected kinematic properties. These expectations can be predicted by theory or observed in studies of simulated decays. Apart from the reconstruction variables defined in chapter 3, there are three additional variables that have to be defined here. Since the  $B_s^0$  meson has a relatively long lifetime of  $1.497 \text{ ps}$  [2], its flight distance  $d$  from the primary or production vertex PV to its decay vertex DV, the secondary vertex, can usually be resolved. The left-hand side of figure 5.1 shows a sketch of this flight distance where for simplicity, only the pion is drawn but the other pion and the muons also originate from the secondary vertex (DV).

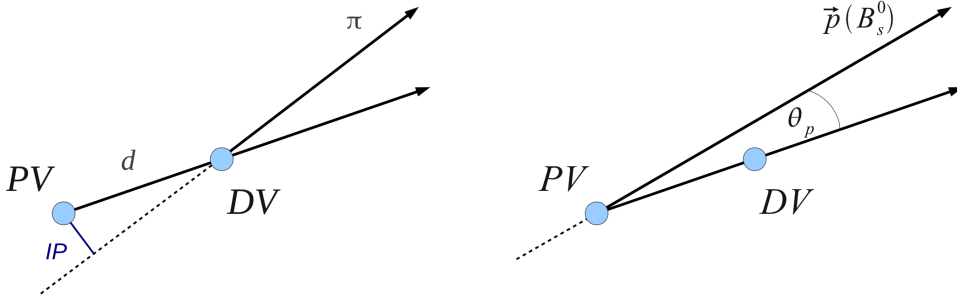


**Figure 5.1:** Definition of impact parameter IP (left) and pointing angle  $\theta_p$ (right)

Thus, the  $B_s^0$  flight distance  $d$  is defined as the absolute value of the flight distance vector  $\vec{d}$  that connects the primary  $\vec{d}_{PV}$  and the secondary vertex  $\vec{d}_{DV}$ :  $d = |\vec{d}_{DV} - \vec{d}_{PV}|$ .

The same sketch also shows the prolongation of the pion track before the decay vertex. The impact parameter IP is defined as the distance of closest approach of the pion track to the primary vertex. The IP significance is defined as the ratio of the impact parameter to its measured uncertainty  $\sigma_{IP}$ :

$$IP_{sig} = \frac{IP}{\sigma_{IP}}. \quad (5.1)$$

Particles that are produced at the PV exhibit a small IP significance. Another kinematic variable is the pointing angle  $\theta_p$  of the  $B_s^0$  sketched on the right-hand side of figure 5.1. It is defined as the angle between the flight distance vector  $\vec{d}$  and the momentum vector  $\vec{p}_{B_s^0}$  of the  $B_s^0$ . Since it moves along the flight distance, the angle should be small for a correctly reconstructed  $B_s^0$ .

## 5.2 Reconstruction and Selection of the decay $B_s^0 \rightarrow J/\Psi\pi^+\pi^-$

The following selection cuts are taken from [38] in which the decay  $B_s^0 \rightarrow J/\Psi f_0(980)$  is studied. By enlarging the selected mass of the  $\pi^+\pi^-$  system, they can also be applied to study the decays of the  $B_s^0$  into  $J/\Psi$  and the heavier resonances  $f_2(1270)$ ,  $f_0(1370)$ ,  $f_0(1500)$  and  $f_2'(1525)$ .

The reconstruction of the decay  $B_s^0 \rightarrow J/\Psi\pi^+\pi^-$  is based on the combination of two muons forming a  $J/\Psi$ , because they can be efficiently detected in the muon chambers. The muons are combined with two pions to form a  $B_s^0$  candidate. In order to ensure a proper track reconstruction quality, all the tracks of the decay products are required to exhibit a track  $\chi^2/nDof$  smaller than 4.<sup>1</sup> Since the  $B_s^0$  has a long lifetime, additional cuts are applied to select events in which it decays at a significant distance away from the primary vertex.

When a selection cut rejects short-lived particles, like a direct cut on the measured proper time, the flight distance from the primary vertex or a cut on the impact parameter, the measured proper time distribution of the selected signal events becomes distorted at low proper times. The selection cut is proper time-dependent. During proton-proton collisions, the number of  $J/\Psi$ 's that are produced directly at the primary vertex is higher than those originating from the decay of a long-lived particle. These  $J/\Psi$ 's are called *prompt* and they pose as background for this analysis and thus have to be rejected.

### 5.2.1 $J/\Psi$ reconstruction

To reconstruct the  $J/\Psi$ , at least two muons are demanded to have traversed the muon chambers with a transverse momentum larger than 500 MeV. Due to the proton beam energy, all the decay products usually have a high longitudinal momentum, but a large transverse momentum indicates that the light muons originate from the decay of a massive particle. The invariant mass of the combined muons is required to lie within 3000 and 3200 MeV, the region around the  $J/\Psi$  PDG [2] mass of 3096.92 MeV. The particle hypothesis provided by the RICH-detectors and the muon chambers is exploited by demanding a  $\Delta \ln \mathcal{L}_{\mu-\pi}$  larger than 0 for the potential muons. To ensure that the decay products originate from the same point, the reconstruction fit of the  $J/\Psi$  vertex must fulfill a  $\chi^2/nDof$  smaller than 11.<sup>2</sup>

<sup>1</sup> The track  $\chi^2/nDof$  was introduced in section 3 and describes the quality of the Kalman filter that is used to reconstruct a track.

<sup>2</sup> The vertex  $\chi^2/nDof$  was introduced in section 3 and describes the quality of the vertex reconstruction.

### 5.2.2 $\pi^+\pi^-$ resonance reconstruction

The selection cuts for the pions are similar to those of the muons, namely a  $\Delta\ln\mathcal{L}_{\pi-K} > -10$  and the sum of the pion transverse momenta is required to be larger than 900 MeV because the  $\pi^+\pi^-$  resonance originates from the massive B-meson. The mass of the combined pion system is demanded to be between 300 and 2200 MeV. Their combined vertex must exhibit a  $\chi^2/nDof < 10$ . An additional cut on the  $IP_{sig}^2 > 9$  for each pion aims to suppress pions produced at the primary vertex, thus this cut already modifies the measured proper time distribution.

### 5.2.3 $B_s^0$ reconstruction

The  $B_s^0$  is reconstructed by combining the  $J/\Psi$  and the  $\pi^+\pi^-$  resonance with a vertex  $\chi^2/nDof$  smaller than 5. The  $B_s^0 IP_{sig}^2$  is required to be smaller than 25. To reject decays in which the proper time has not been measured accurately enough, the estimated proper time uncertainty  $\sigma_{ct}$  is demanded to be smaller than 0.1 ps. The following selection cuts exploit the fact that the finite  $B_s^0$  lifetime leads to a resolvable flight distance. The absolute flight distance is required to be larger than 1.5 mm and the cosine of the pointing angle  $\theta_p$  has to be larger than 0.99993, so that the flight distance direction matches the momentum direction. A list of all applied selection cuts is given in table 5.1. It also includes cuts that are applied later in the determination of  $\phi_s$ .

Quantity	Selected values
Track $\frac{\chi^2}{nDof}$ for muons and pions	$< 4$
$J/\Psi$ Vertex $\frac{\chi^2}{nDof}$	$< 11$
$\pi\pi$ Vertex $\frac{\chi^2}{nDof}$	$< 10$
$B_s^0$ Vertex $\frac{\chi^2}{nDof}$	$< 5$
$B_s^0 IP_{sig}^2$	$< 25$
$\pi IP_{sig}^2$	$> 9$
$p_t(\pi_1) + p_t(\pi_2)$	$> 900$ MeV
$p_t(\mu)$	$> 500$ MeV
$\pi \Delta\ln\mathcal{L}_{\pi-K}$	$> -10$
$\mu \Delta\ln\mathcal{L}_{\mu-\pi}$	$> 0$
$B_s^0$ flight distance	$> 1.5$ mm
$B_s^0$ pointing angle $\cos \theta_p$	$> 0.99993$
$B_s^0$ proper time uncertainty $\sigma_{ct}$	$< 0.1$ ps
$m_{\pi\pi}$	300 – 2200 MeV
cuts applied later in the analysis	
$m_{J/\Psi}$	3048.92 – 3139.92 MeV
$m_{\pi\pi}$	775 – 1550 MeV
$B_s^0$ proper time	$> 0.3$ ps

**Table 5.1:** Analysis selection requirements

### 5.3 Fully simulated samples of signal decays and potential background decays

By looking for channels with the final state  $J/\Psi\pi^+\pi^-$ , the PDG [2] can be used to list the signal decays and potential background decays that might be selected with the analysis selection cuts. Decays in which a  $J/\Psi$  plus one pion and a Kaon are produced must also be considered because the Kaon can be misidentified as a pion by the RICH detectors. For some of these channels, fully simulated decays are available in order to investigate the expected invariant mass distributions. These simulated decays are reconstructed in the same way as the data. As a consequence, the assigned particle hypothesis and hence the mass of the decay products might differ from the original generated decay. This is the reason why the invariant mass of B-candidates of decays like  $B^0 \rightarrow J/\Psi K^*(\rightarrow K\pi)$ , reconstructed as  $B_s^0 \rightarrow J/\Psi \pi^+\pi^-$ , lies in lower mass ranges than the expected  $B^0$  mass and the distribution becomes distorted.

#### 5.3.1 Signal decays

The relevant signal decays that are studied in this analysis are the  $B_s^0 \rightarrow J/\Psi f_0/f_2(\rightarrow \pi^+\pi^-)$  decays that are listed in table 5.2.

decay	notes
$B_s^0 \rightarrow J/\Psi f_0(980)(\rightarrow \pi^+\pi^-)$	simulated decays available
$B_s^0 \rightarrow J/\Psi f_2(1270)(\rightarrow \pi^+\pi^-)$	—
$B_s^0 \rightarrow J/\Psi f_0(1370)(\rightarrow \pi^+\pi^-)$	—
$B_s^0 \rightarrow J/\Psi f_0(1500)(\rightarrow \pi^+\pi^-)$	—
$B_s^0 \rightarrow J/\Psi f_2'(1525)(\rightarrow \pi^+\pi^-)$	—

**Table 5.2:** Signal decays

Simulated decays are only available for the channel  $B_s^0 \rightarrow J/\Psi f_0(980)$ . Figure 5.2 (left) shows the reconstructed mass of the  $B_s^0$  meson and the right-hand side shows the mass distribution of the  $\pi^+\pi^-$  system that is produced in the decay of the  $f_0(980)$ .

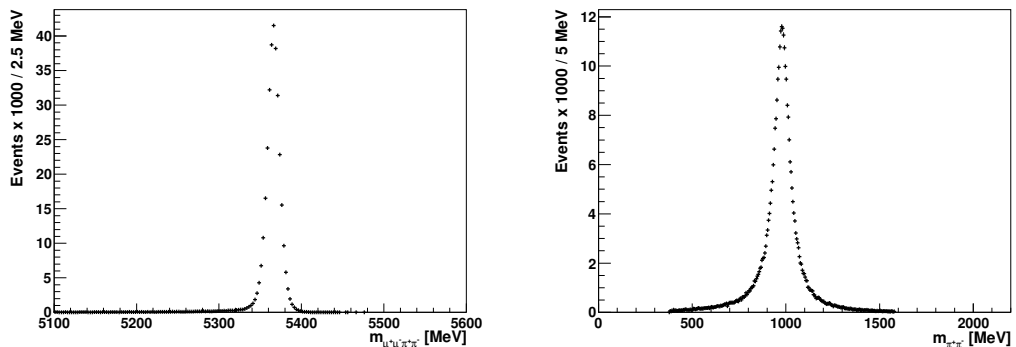


**Figure 5.2:** Invariant mass distribution of the  $B_s^0$  candidates(left) and the  $\pi^+\pi^-$  (right) system from simulated  $B_s^0 \rightarrow J/\Psi f_0(980)$  decays

The  $B_s^0$  signal peak lies approximately in the region  $\pm 20$  MeV of the PDG [2] mass of 5366.3

MeV. The  $f_0(980)$  peak at the PDG mass of 990 MeV has a large width of about 100 MeV and tails that extend to 500 and 1400 MeV.

### 5.3.2 Potential background decays

#### Background from $B^0$ decays

Potential background from  $B^0$  decays is listed in table 5.3. There is a non-resonant  $B^0 \rightarrow J/\Psi \pi^+\pi^-$  and a  $B^0 \rightarrow J/\Psi \rho(770)(\rightarrow \pi^+\pi^-)$  channel. Channels in which the Kaon is misidentified as a pion are  $B^0 \rightarrow J/\Psi K^\pm\pi^\mp$  and resonant  $B^0 \rightarrow J/\Psi K^*(892)(\rightarrow K^\pm\pi^\mp)$ .

decay	notes
$B^0 \rightarrow J/\Psi \pi^+\pi^-$ ( <i>non - resonant</i> )	$B^0$ - signal
$B^0 \rightarrow J/\Psi \rho(770)(\rightarrow \pi^+\pi^-)$	$B^0$ - signal
$B^0 \rightarrow J/\Psi K^\pm\pi^\mp$ ( <i>non - resonant</i> )	misidentified Kaon, no simulated decays available
$B^0 \rightarrow J/\Psi K^*(892)(\rightarrow K^\pm\pi^\mp)$	misidentified Kaon, simulated decays available

**Table 5.3:** Potential background from  $B^0$  decays

Simulated decays are available for the channel  $B^0 \rightarrow J/\Psi K^*(\rightarrow K\pi)$ . The left-hand side of figure 5.3 shows the  $\mu^+\mu^-\pi^+\pi^-$  mass distribution of the selected events from the simulated decay  $B^0 \rightarrow J/\Psi K^*(\rightarrow K\pi)$ . It shows an asymmetric peak around 5230 MeV, about 50 MeV below the  $B^0$  PDG [2] mass of 5279.5 MeV. The peak has a sharp edge to higher masses but stretches widely into the lower mass range. In addition, the invariant mass of the misidentified hadronic system is given on the right. It features a similar asymmetric peak around 700 MeV, about 200 MeV below the  $K^*(892)$  PDG mass of 891.66 MeV, that is smeared into mass regions as high as 1500 MeV because of the large  $K^*$  width of 48.7 MeV and the misidentification of the Kaon.

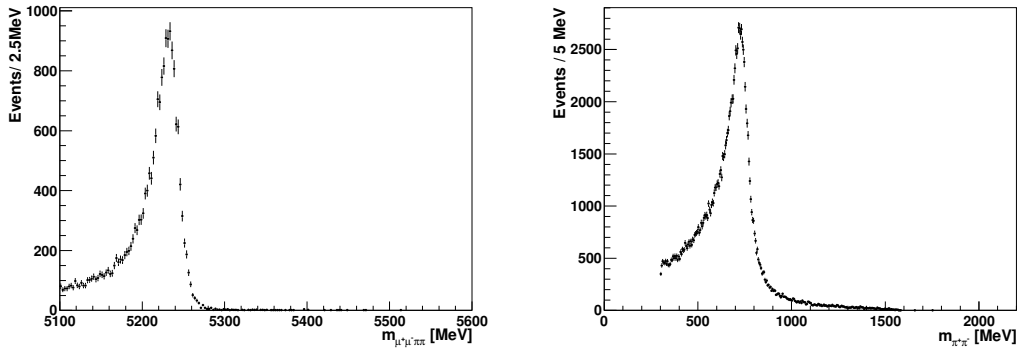


**Figure 5.3:** Invariant mass distribution of the  $\mu^+\mu^-\pi^+\pi^-$  system (left) and the  $\pi^+\pi^-$  system (right) from simulated  $B^0 \rightarrow J/\Psi K^*$  decays

#### Background from $B_s^0$ decays

Background  $B_s^0$  decays that can contribute to the selected  $B_s^0$  candidates are given in table 5.4.

decay	notes
$B_s^0 \rightarrow J/\Psi \eta'(958)(\rightarrow \pi^+\pi^-\gamma(\gamma))$	decay via $\rho$ or $\eta$ , simulated decays available
$B_s^0 \rightarrow J/\Psi \phi(1020)(\rightarrow K^+K^-)$	two misidentified Kaons, simulated decays available

**Table 5.4:** Potential background from  $B_s^0$  decays

In the channel  $B_s \rightarrow J/\Psi \eta'$ , the  $\eta'$  dominantly decays into  $(\rho(\pi\pi) + \gamma)$  or  $(\eta(3\pi^0) + \pi\pi)$ . The mass distribution of the reconstructed  $B_s^0$  candidates of the simulated  $B_s \rightarrow J/\Psi \eta'$  decays is shown on the left-hand side of figure 5.4. Since the emitted photon and the  $\eta$  are not reconstructed, the mass of the  $B_s^0$  candidates is reduced and shifted to lower values. The non-peaking broad structure has an edge around 5330 MeV with a few events leaking into the range of the real  $B_s^0$  mass. Additionally, the mass distribution of the selected pion system is plotted on the right where a clean peak around the  $\rho$  mass of 775.5 MeV [2] can be seen.

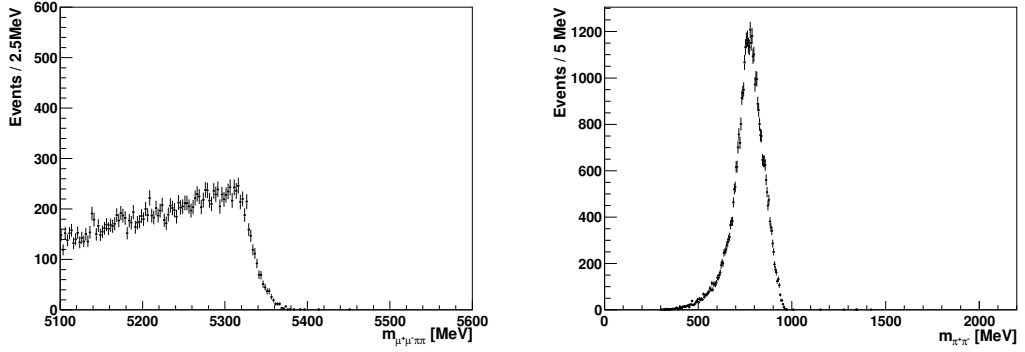


**Figure 5.4:** Invariant mass distribution of the  $\mu^+\mu^-\pi^+\pi^-$  system (left) and the  $\pi^+\pi^-$  system (right) from simulated  $B_s \rightarrow J/\Psi \eta'$  decays

To select  $B_s^0 \rightarrow J/\Psi \phi$  as signal, two Kaons have to be misidentified as pions which is unlikely. The wrong mass hypothesis of the daughter leads to an even larger shift of the  $B_s^0$  candidate mass towards smaller values. Figure 5.5 shows the invariant mass distribution of the misidentified hadronic system from simulated  $B_s \rightarrow J/\Psi \phi$  decays. The reconstructed masses are lower than 775 MeV which will be the final mass selection cut for the pion system. Thus, this channel cannot contribute to the selected decays in data.

### Background from $B^\pm$ decays

The channel  $B^\pm \rightarrow J/\Psi K^\pm$  can contribute to background if the Kaon is misidentified as a pion and combined with a random pion. Since another particle's energy is added to the total energy, the invariant mass of the four particles can be higher than the  $B^\pm$  mass. Simulation shows that the decays of this channel are not selected.

decay	notes
$B^\pm \rightarrow J/\Psi K^\pm$	simulated decays are not selected

**Table 5.5:** Potential background from a  $B^\pm$  decay

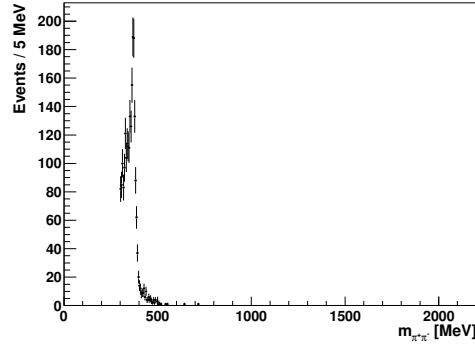


**Figure 5.5:** Invariant mass distribution of the misidentified  $\pi^+\pi^-$  system from simulated  $B_s \rightarrow J/\Psi\phi$  decays

## 5.4 Mass distributions of the selected $B_s^0 \rightarrow J/\Psi\pi^+\pi^-$ candidates obtained from data

This chapter presents the invariant mass distributions of the selected reconstructed decays obtained from data. Since the  $J/\Psi$  is the first particle that is reconstructed in the decay, figure 5.6 shows the invariant mass distribution of the  $\mu^+\mu^-$  system. A clean mass peak is visible. The slightly asymmetric shape is a result of final state bremsstrahlung emission. Candidate events are selected if their reconstructed  $J/\Psi$  mass is within  $-48$  and  $+43$  MeV of the  $J/\Psi$ -mass of  $3096.92$  MeV [2] as it is done in [40].

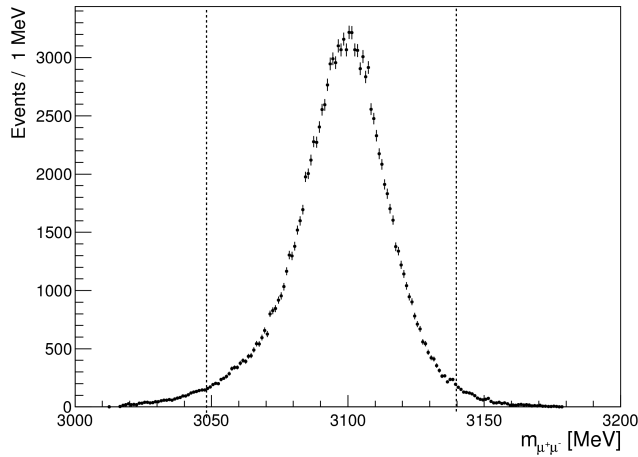


**Figure 5.6:** Invariant mass distribution of the selected  $\mu^+\mu^-$  system. The dashed lines indicate the mass range that is selected from now on.

The left-hand side of figure 5.7 shows the reconstructed mass of the selected  $B_s^0$  candidates in black. On the right, the mass of the selected  $\pi^+\pi^-$  system is plotted in black. In addition, the figures contain combinatorial background (red) which is generated by choosing equal sign  $\pi\pi$  candidates instead of opposite sign as one would expect for a real  $f_0$  or  $f_2$ . This wrong sign

background models the probability to combine two random pions with a  $J/\Psi$  to mimic a  $B_s^0$ .

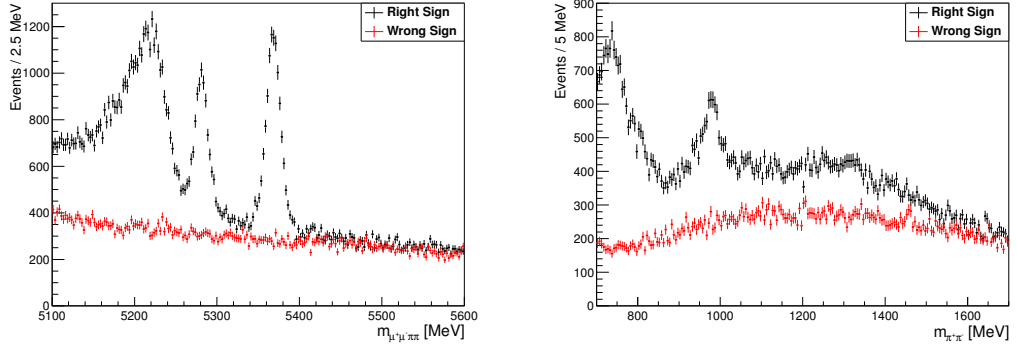


**Figure 5.7:** Invariant mass distribution of the selected  $B_s^0$  candidates (left) and the selected  $\pi^+\pi^-$  systems (right)

In Figure 5.7(left), two narrow peaks at 5370 MeV and 5280 MeV and a broad structure in the lower mass range are visible. Considering the  $B_s^0$  mass of 5366.3 MeV [2] and the  $B^0$  mass of 5279.5 MeV, one can identify the peaks as the  $B_s^0$  and the  $B^0$  while the broad low-mass contribution does not have a typical resonant structure. The contribution from combinatorial background is very large and agrees well with the right sign data in the upper mass region. In the  $\pi^+\pi^-$  mass distribution, there is a wide large peak at the  $\rho$  mass of 775.5 MeV, a smaller one at the  $f_0$  resonance mass of 990 MeV and a non-peaking structure above. A high amount of background events can be observed, but the combinatorial contribution described by the WS events can only explain the visible tails towards high  $\pi^+\pi^-$  masses. The relevant mass region of the  $\pi^+\pi^-$  system that contains the resonances  $f_0$  and  $f_2$  cannot be determined in this figure. Therefore, only events of the potential  $B_s^0$  mass peak, i.e.  $\pm 20$  MeV around 5366.3 MeV, are selected to plot the  $\pi\pi$  mass distribution in figure 5.8.

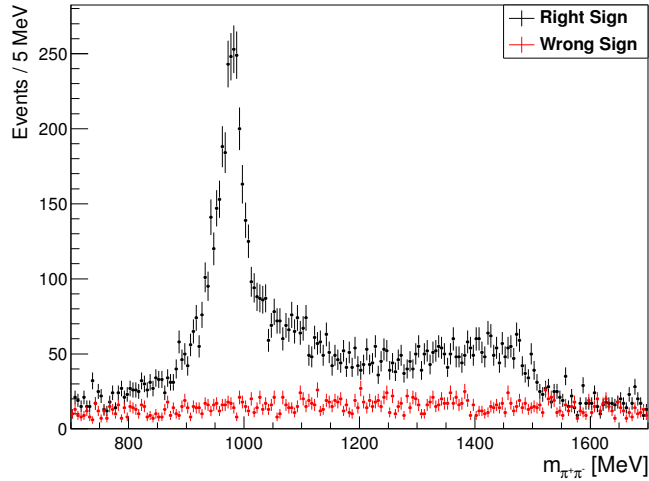


**Figure 5.8:** Invariant mass distribution of the selected  $\pi^+\pi^-$  systems for candidate events with a reconstructed mass of  $m_{B_s^0} \pm 20$  MeV

The background level at small and large  $\pi\pi$  masses is now significantly lower, the  $\rho$  mass peak in the lower mass range completely gone and the large  $f_0$  peak around 990 MeV is visible. Between 1100 and 1500 MeV, one observes a broad non-peaking structure that originates from the higher  $f_0$  and  $f_2$  resonances and lies clearly above the combinatorial background modeled by the wrong sign events. From this plot, one can estimate the relevant mass region of the  $\pi\pi$  system to be between approximately 775 and 1550 MeV. However, it can still contain contributions from the decay  $B_s^0 \rightarrow J/\Psi \eta' (\rightarrow \rho\gamma)$  or from other background sources. Thus, the complete  $B_s^0$  candidate mass distribution has to be analyzed when selecting this  $\pi^+\pi^-$  mass region. The resulting mass distribution of the  $B_s^0$  candidates is plotted in figure 5.9 and will be analyzed in the next section.

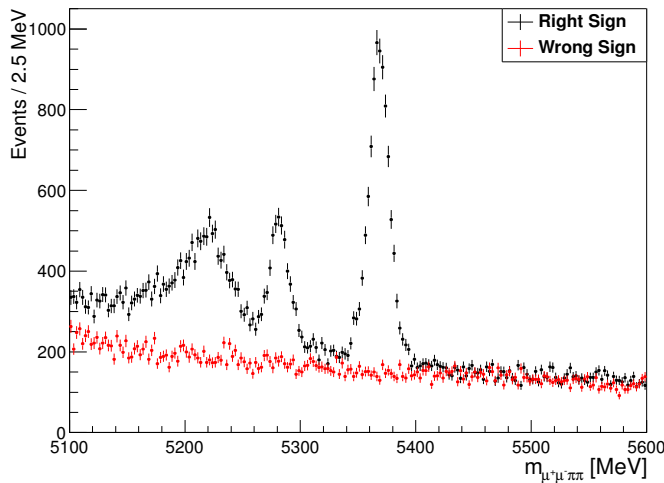


**Figure 5.9:** Invariant mass distribution of the selected  $B_s^0$  candidates with  $775 \text{ MeV} < m_{\pi\pi} < 1550 \text{ MeV}$

The background has decreased while the number of events of the  $B_s^0$  peak appears to remain the same. The peak at 5280 MeV is half as high as before because the  $\rho$  events are only partly selected now. The broad structure is reduced significantly and has a similar structure as the mass distribution of the simulated  $B^0 \rightarrow J/\Psi K^*(892)$  decays in figure 5.3 but it appears to be broader and smeared towards lower masses. Nevertheless, it gives a hint which decays are recorded here.

## 5.5 Signal and background modeling for the selected $B_s^0$ candidates

This section tries to use the mass distributions obtained from the fully simulated events, and several functions to model the complete mass distribution of the selected  $B_s^0$  candidates obtained from data. The  $B_s^0$  mass distribution of the simulated  $B_s^0 \rightarrow J/\Psi f_0(980)$  cannot be used to describe the signal peak because it also contains decays into the higher  $f_0$  and  $f_2$  resonances. Since the natural widths of the B's are much smaller than the mass resolution of the detector, the structure of the  $B_s^0$  and the  $B^0$  signal peaks is determined by the mass resolution which is modeled by the sum of two normalised Gaussian functions

$$DG(m_{\mu\mu\pi\pi}) = \left\{ \frac{f_1}{\sqrt{2\pi}\sigma_1} \exp\left(-\frac{(m_{\mu\mu\pi\pi} - m_B)^2}{2\sigma_1^2}\right) + \frac{1-f_1}{\sqrt{2\pi}\sigma_2} \exp\left(-\frac{(m_{\mu\mu\pi\pi} - m_B)^2}{2\sigma_2^2}\right) \right\}, \quad (5.2)$$

where  $f_1$  indicates the fraction of the first Gaussian,  $\sigma_i$  are the widths of the two Gaussians and  $m_B$ , the mass of the B-mesons, is the mean of the Gaussians.

The combinatorial non-resonance background is not modeled by the wrong sign events as one would expect because this cannot be applied in the determination of the phase  $\phi_s$  where one has to provide a probability density function to model the background behaviour. An exponential decay function

$$N_{comb}(m_{\mu\mu\pi\pi}) \propto e^{-\alpha m_{\mu\mu\pi\pi}} \quad (5.3)$$

with the decay constant  $\alpha$  is chosen because it describes the wrong sign data well. For each simulated background decay, the histogram of the reconstructed  $B_s^0$  mass distribution is normalised and used as a template to model the shape of the data. The normalisation is allowed to float and thus gives the number of decays that contribute to the selected data.

In order to estimate the quality of the fit result for one particular bin of the histogram, the pull distribution for this bin is defined as

$$pull(m_{\mu\mu\pi\pi}) = \frac{N_{bin}(m_{\mu\mu\pi\pi}) - N_{fit}(m_{\mu\mu\pi\pi})}{\sigma_{N_{bin}}}, \quad (5.4)$$

where  $N_{bin}(m_{\mu\mu\pi\pi})$  refers to the entry of the histogram bin at mass  $m_{\mu\mu\pi\pi}$ ,  $\sigma_{N_{bin}} = \sqrt{N_{bin}}$  is the uncertainty of the bin content and  $N_{fit}$  the number of entries described by the fit. If the fit describes the data well, the mean of the pull distribution is zero and the width is 1 because fluctuations of  $N_{bin}$  should be in the order of the assigned uncertainty.

The results of the total fit are shown in figure 5.10 where the lower plot gives the pull distribution and the upper plot shows the invariant mass distribution of the  $B_s^0$  candidates with the respective  $\chi^2$  contributing functions of the fit. The  $\chi^2/nDof$  of the fit is larger than 2.3, i.e. the fit model is insufficient to describe the data in the whole mass range, as can be clearly seen.

In the table of figure 5.10,  $N_{B_s^0}$  refers to the number of signal  $B_s^0$  candidates,  $N_{B^0}$  the number of  $B^0 \rightarrow J/\Psi\pi^+\pi^-$  decays,  $N_{\eta'}$  the number of  $B_s^0 \rightarrow J/\Psi\eta'$  decays,  $N_{K^*}$  the number of  $B^0 \rightarrow J/\Psi K^*$  decays and  $N_{comb}$  the number of combinatorial background decays. The two double Gaussian functions with 6695  $B_s^0$  events in green and 2389  $B^0$  events in blue describe the peaks very well. The measured  $B$  masses are  $5368.2 \pm 0.2$  MeV and  $5281.5 \pm 0.3$  MeV, thus 2 MeV above the PDG [2] values of 5366.77 MeV and 5279.58 MeV. This can be traced back to the misalignment of the detector and a wrong B-field calibration that leads to a momentum scale uncertainty.<sup>1</sup> As this analysis does not measure the absolute mass of the  $B_s^0$ , this observed shift is irrelevant. The combinatorial background in brown agrees with the data in the mass range above the  $B_s^0$  peak but by looking at the pull distribution more closely, the data first lies beneath the fit and towards higher masses exceeds the fit. The decay constant  $\alpha$  is thus too

---

<sup>1</sup> The momentum scale and the B-field are not fully calibrated for the available data set.

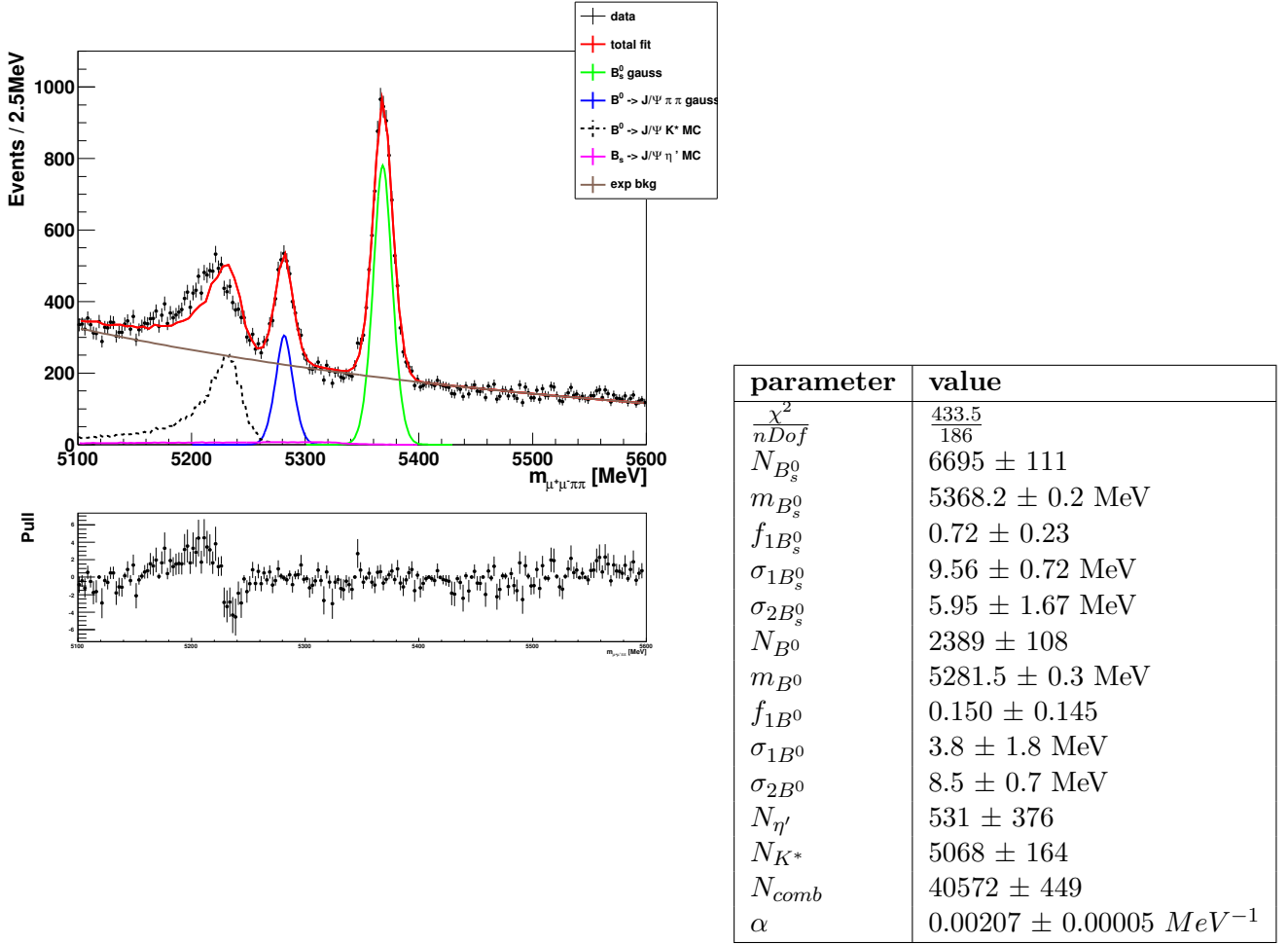


**Figure 5.10:** Invariant mass distribution of the selected  $B_s^0$  candidates obtained from data on the upper left with the double Gaussian functions for the  $B_s^0$  signal candidates in green and the reconstructed  $B^0$  candidates in blue, the  $B_s \rightarrow J/\Psi\eta'$  template in purple, the  $B^0 \rightarrow J/\Psi K^*$  component in dashed black and the combinatorial background in brown. In the lower left, the pull distribution and the fitted parameters are on the right.

large to describe the slope. The  $B_s \rightarrow J/\Psi\eta'$  in purple appears to play a minor role with its tiny peak below and single events in the  $B_s^0$  peak region. The  $B^0 \rightarrow J/\Psi K^*$  decay in dashed black appears to really contribute numerously to the data sample, but the description of the data points by the template is bad. The mass seems to be shifted to lower values in the data, the structure is broader and the rise at the edge is less steep which leads to the bad  $\chi^2/nDof$  value. The reasons for this could be an imperfection of the simulated sample or an additional non-resonant  $B^0 \rightarrow J/\Psi K^\pm \pi^\mp$  portion that should also be taken into account in this mass region but can hardly be described analytically without simulation. Since the Kaon and the pion here do not originate from one resonance but are produced directly in the decay of the  $B^0$ , these decays can exhibit a different mass distribution than the  $K^*$  decays. As for the

determination of the phase  $\phi_s$ , only events in the mass region from 5320 - 5600 MeV will be selected, the badly described background component at around 5200 MeV has no effect.

For this reason the fit is repeated in the mass range from 5260-5600 MeV without the  $B^0 \rightarrow J/\Psi K^*$  component. The results are shown in figure 5.11. Now, the fit exhibits an improved  $\chi^2/nDof$  of 117/123 and a decreased decay constant  $\alpha$  of  $0.00128 \text{ MeV}^{-1}$  so that the pull is equally distributed around zero in the fitted mass range.

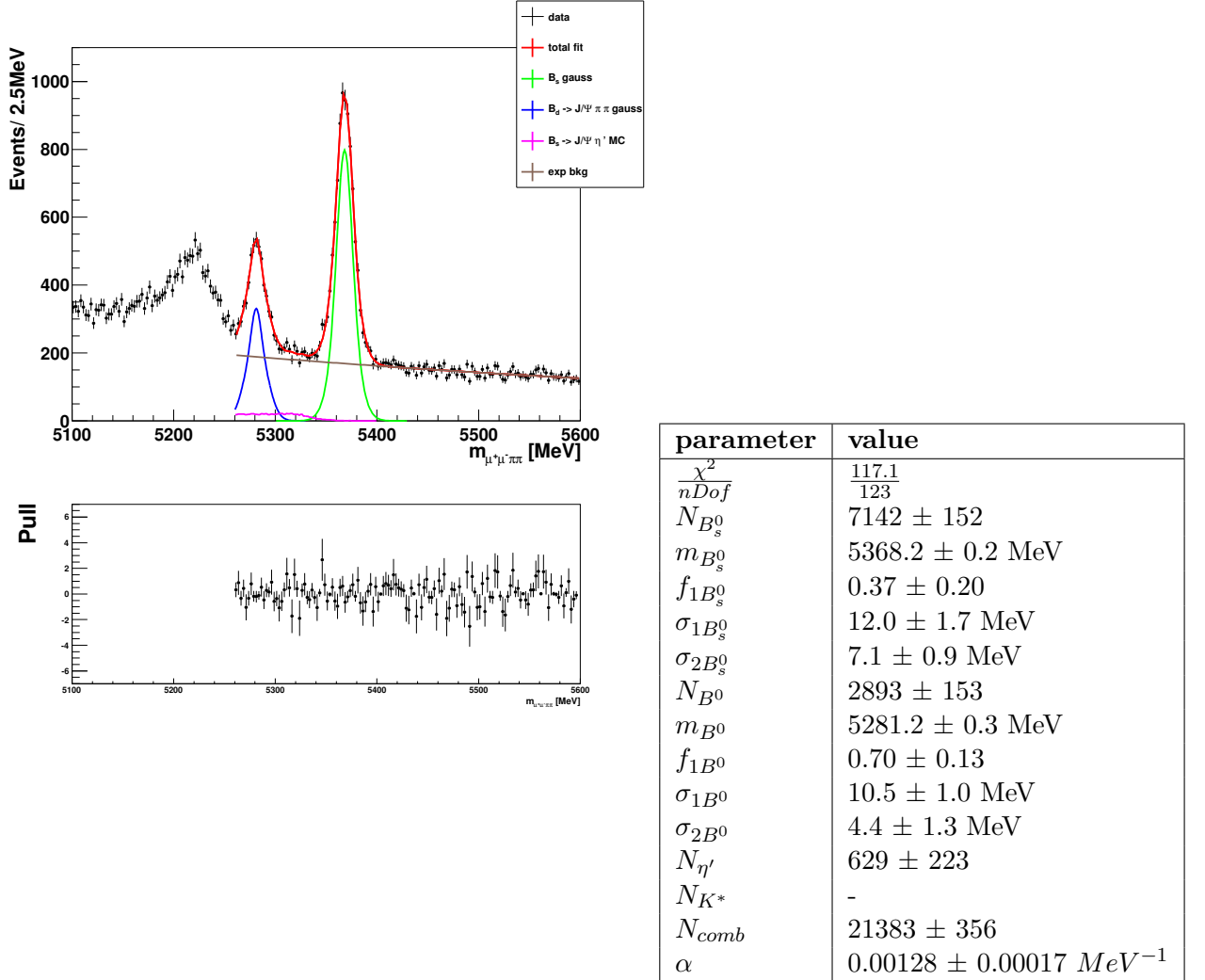


**Figure 5.11:** Invariant mass distribution of the selected  $B_s^0$  candidates obtained from data on the upper left with the double Gaussian functions for the  $B_s^0$  signal candidates in green and the reconstructed  $B^0$  candidates in blue, the  $B_s \rightarrow J/\Psi \eta'$  template in purple and the combinatorial background in brown. In the lower left, the pull distribution and the fitted parameters are on the right.

In the upper sideband of the  $B_s^0$ , the combinatorial background agrees well with the data in average but the fluctuations seen in the pulls are fairly large. However, these fluctuations have also been observed for the wrong sign data in figure 5.9. Due to lower combinatorial

background, the number of signal  $B_s^0$  candidates rises to 7142, the number of  $B^0$  candidates to 2893 but also the number of  $B_s^0 \rightarrow J/\Psi\eta'$  decays rises to 629 although the events below 5260 MeV are not counted anymore.

For the final analysis, there will be an additional proper time cut at 0.3 ps for reasons which are explained later. For completeness the mass fit in the mass range 5260 - 5600 MeV is rerun with this proper time cut and shown in figure 5.12. It can be observed that the combinatorial background decreases significantly from 21383 to 18021 while the number of  $B_s^0$ 's decreases only from 7142 to 7109.

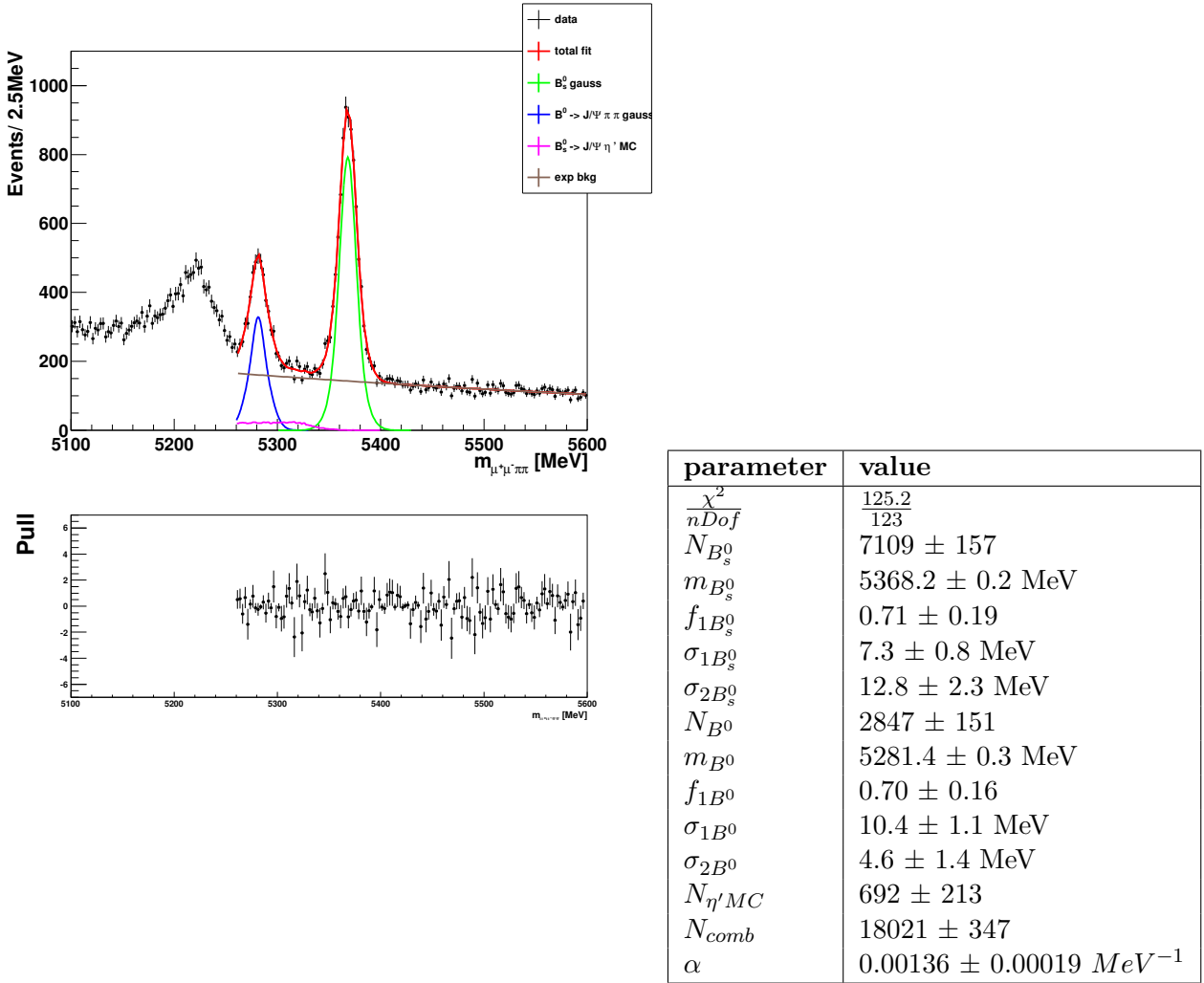


**Figure 5.12:** Invariant mass distribution of the selected  $B_s^0$  candidates obtained from data with an additional proper time cut  $> 0.3$  ps on the upper left. The double Gaussian functions for the  $B_s^0$  signal candidates in green and the reconstructed  $B^0$  candidates in blue, the  $B_s \rightarrow J/\Psi\eta'$  template in purple and the combinatorial background in brown. In the lower left, the pull distribution and the fitted parameters are on the right.

The number of  $B_s^0 \rightarrow J/\Psi \eta'$  is determined to be  $692 \pm 213$  in the fitted mass region but the total number in the mass range 5320 - 5600 MeV is  $162 \pm 50$  and is therefore tiny compared to the  $B_s^0$  contribution.

The results of these mass fits provide a good description of the events that are selected in this analysis. A total number of about 7100  $B_s^0 \rightarrow J/\Psi \pi^+ \pi^+$  signal candidates and 2900  $B^0 \rightarrow J/\Psi \pi^+ \pi^+$  candidates are selected. The presence of a  $B_s^0 \rightarrow J/\Psi \eta'$  component cannot be excluded but its extension into the mass region above 5320 MeV is negligible. The broad structure in the lower mass regions presumably originates from  $B^0 \rightarrow J/\Psi K^\pm \pi^\pm$  events but is definitely limited to smaller masses than 5300 MeV. Considering the good agreement between the wrong sign and the right sign data in the upper mass band and the good description by the exponential function, it is assumed that the background between 5320 and 5600 MeV is solely composed of combinatorics except for a tiny contribution from  $B_s^0 \rightarrow J/\Psi \eta'$ . Since it is difficult to describe the proper time distribution of various background contributions, the mass range of the  $B_s^0$  candidates will be restricted to this region to determine the phase  $\phi_s$ .

## 5.6 Determination of the spin of the $\pi^+ \pi^-$ states in the mass peak region of the $f_0(980)$

For the determination of the phase  $\phi_s$ , it is crucial that the final state  $J/\Psi \pi^+ \pi^-$  makes up a CP-eigenstate. As discussed in the theory chapter, for  $\pi^+ \pi^-$  resonances with spin  $\mathbf{J} = 0$  or 2 and spin projection  $J_z = 0$ , the CP-eigenstate is odd. In [38], it is shown that the two pion system can only have even spin because of even G-parity. Since there are no spin-4 resonances with a mass below 2 GeV, the CP-even eigenstate can only be made up by the  $J/\Psi$  and a  $\pi^+ \pi^-$  state with spin 2 and  $J_z = \pm 1$ . The Dalitz analysis in [37] shows that the CP-odd fraction in  $B_s^0 \rightarrow J/\Psi \pi^+ \pi^-$  decays in the selected mass range of the  $\pi^+ \pi^-$  system is greater than 0.977 at 95 % confidence level. A comparable analysis goes beyond the scope of this thesis, but this chapter attempts to measure the spin contributions of the  $\pi^+ \pi^-$  system in the mass peak region of the  $f_0(980)$  only. This consistency check aims to confirm the spin  $\mathbf{J} = 0$  of the resonance  $f_0(980)$ . If  $\pi^+ \pi^-$  states from higher resonances with spin  $\mathbf{J} = 2$  are among these candidates, they should exhibit a dominant spin projection of  $J_z = 0$  and a negligible  $J_z = \pm 1$  component so that the CP-eigenstate of the final state can be assumed to be odd.

One way to measure the spin of a resonance is to analyze the angular distribution of its decay products. Since the  $f_0(980)$  is produced in the decay of the  $B_s^0$  alongside with the  $J/\Psi$ , the decay products have to be described in the so-called helicity basis defined in figure 5.13. The angle  $\theta_{J/\Psi}$  is defined in the rest frame of the  $J/\Psi$  as the angle of the  $\mu^+$  with respect to the  $B_s^0$  flight direction and  $\theta_{f_0}$  is defined in the rest frame of the  $f_0$  as the angle of the  $\pi^+$  with respect to the  $B_s^0$  flight direction. The spin of the  $B_s^0$  has been determined to be 0 and the  $J/\Psi$  has spin 1. Allowing spin-0 and spin-2 states for the  $\pi^+ \pi^-$  system, the joint angular distribution function is given in equation 5.5 where  $A_{00}$  is the spin-0 amplitude,  $A_{2i}$  the spin-2 amplitudes with

$J_z = i$  and  $\delta$  is the strong phase between the  $A_{20}$  and the  $A_{00}$  amplitude [38]:

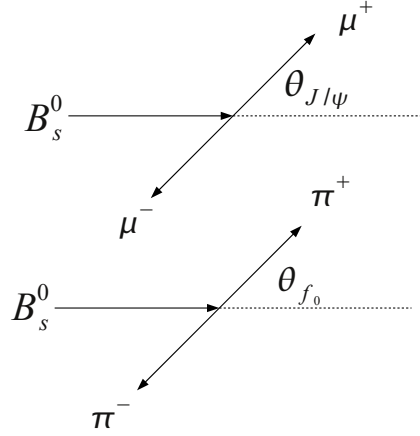


**Figure 5.13:** Definition of  $\theta_{J/\Psi}$  and  $\theta_{f_0}$  in the helicity basis

$$\begin{aligned}
 \frac{d\Gamma}{d \cos \theta_{J/\Psi} d \cos \theta_{f_0}} &= \left| A_{00} + \frac{1}{2} A_{20} e^{i\delta} \sqrt{5} (3 \cos^2 \theta_{f_0} - 1) \right|^2 \sin^2 \theta_{J/\Psi} \\
 &\quad + \frac{1}{4} (|A_{21}|^2 + |A_{2-1}|^2) (15 \sin^2 \theta_{f_0} \cos^2 \theta_{f_0}) (1 + \cos^2 \theta_{J/\Psi}) \\
 &= \sin^2 \theta_{J/\Psi} \left( |A_{00}|^2 + \frac{5}{4} |A_{20}|^2 (3 \cos^2 \theta_{f_0} - 1)^2 \right. \\
 &\quad \left. + \sqrt{|A_{00}|^2} \sqrt{|A_{20}|^2} \sqrt{5} \cos \delta (3 \cos^2 \theta_{f_0} - 1) \right) \\
 &\quad + \frac{1}{4} (|A_{21}|^2 + |A_{2-1}|^2) (15 \sin^2 \theta_{f_0} \cos^2 \theta_{f_0}) (1 + \cos^2 \theta_{J/\Psi}).
 \end{aligned} \tag{5.5}$$

Integrating over  $\cos \theta_{f_0}$  gives the one-dimensional angular distribution in terms of  $\cos \theta_{J/\Psi}$ :

$$\begin{aligned}
 \frac{d\Gamma}{d \cos \theta_{J/\Psi}} &= \int_{\cos \theta_{f_0} = -1}^1 \frac{d\Gamma}{d \cos \theta_{J/\Psi} d \cos \theta_{f_0}} d \cos \theta_{f_0} \\
 &= 2 \left( |A_{00}|^2 + |A_{20}|^2 \right) \sin^2 \theta_{J/\Psi} + \left( |A_{21}|^2 + |A_{2-1}|^2 \right) (1 + \cos^2 \theta_{J/\Psi})
 \end{aligned} \tag{5.6}$$

or correspondingly integrating equation 5.5 over  $\cos \theta_{J/\Psi}$  gives the distribution in  $\cos \theta_{f_0}$ :

$$\begin{aligned}
 \frac{d\Gamma}{d \cos \theta_{f_0}} &= \int_{\cos \theta_{J/\Psi} = -1}^1 \frac{d\Gamma}{d \cos \theta_{J/\Psi} d \cos \theta_{f_0}} d \cos \theta_{J/\Psi} \\
 &= \frac{4}{3} \left( |A_{00}|^2 + \frac{5}{4} |A_{20}|^2 (3 \cos^2 \theta_{f_0} - 1)^2 + \sqrt{|A_{00}|^2} \sqrt{|A_{20}|^2} \sqrt{5} \cos \delta (3 \cos^2 \theta_{f_0} - 1) \right) \\
 &\quad + 10(|A_{21}|^2 + |A_{2-1}|^2) \sin^2 \theta_{f_0} \cos^2 \theta_{f_0}.
 \end{aligned} \tag{5.7}$$

Integrating over both angles gives the total integrated decay width

$$\Gamma = \frac{8}{3} |A_{00}|^2 + \frac{8}{3} |A_{20}|^2 + \frac{8}{3} (|A_{21}|^2 + |A_{2-1}|^2). \tag{5.8}$$

For a pure spin-0 resonance ( $A_{2i} = 0$ ),  $\cos \theta_{J/\Psi}$  should be distributed as  $\sin^2 \theta_{J/\Psi}$  while it is flat in  $\cos \theta_{f_0}$ .

Before the measured angular distributions can be fitted with the theoretical predictions, the geometrical *angular acceptance*  $\epsilon_{acpt}$  of the detector has to be determined. The detector is not a homogeneous object but built from different sub-components with well defined sensitive areas. The acceptance describes the efficiency of the particle detection as a function of the helicity angles and is defined as the ratio of the number of reconstructed and accepted events  $N_{acpt}$  and the total number of events  $N_{event}$ :

$$\epsilon_{acpt}(\cos \theta_{J/\Psi}, \cos \theta_{f_0}) = \frac{N_{acpt}(\cos \theta_{J/\Psi}, \cos \theta_{f_0})}{N_{event}(\cos \theta_{J/\Psi}, \cos \theta_{f_0})}. \tag{5.9}$$

The detector acceptance has been intensively studied and is taken into account by the detector simulations. Hence, the number of accepted events as a function of the angles can be easily determined in simulated  $B_s^0 \rightarrow J/\Psi f_0(980)$  decays. However, the acceptance effects are already accounted for in the generation of the simulated events to reduce the computational effort. The total number of events as a function of the angle cannot be computed. Thus, the acceptance  $\epsilon_{acpt}$  has to be determined by comparing the measured simulated angular distribution  $d\Gamma_{mes}$  with the theoretical prediction  $d\Gamma_{theo}$ . The acceptance is proportional to the ratio  $d\Gamma_{mes}/d\Gamma_{theo}$ :

$$\epsilon_{acpt}(\cos \theta_{J/\Psi}, \cos \theta_{f_0}) \propto \frac{d\Gamma_{mes}(\cos \theta_{J/\Psi}, \cos \theta_{f_0})}{d\Gamma_{theo}(\cos \theta_{J/\Psi}, \cos \theta_{f_0})}. \tag{5.10}$$

This is not the absolute detection efficiency but only the relative efficiency. The shape as a function of  $\cos \theta_{J/\Psi}$  and  $\cos \theta_{f_0}$  is of importance.

The angular acceptance is defined as a 2-dimensional function of the two variables  $\cos \theta_{J/\Psi}$  and  $\cos \theta_{f_0}$ . For clarity, figure 5.14 shows the normalised 1-dimensional projections of the angular acceptance computed with  $B_s^0 \rightarrow J/\Psi f_0(980)$  decays and applying the theoretical distribution from equation 5.5.

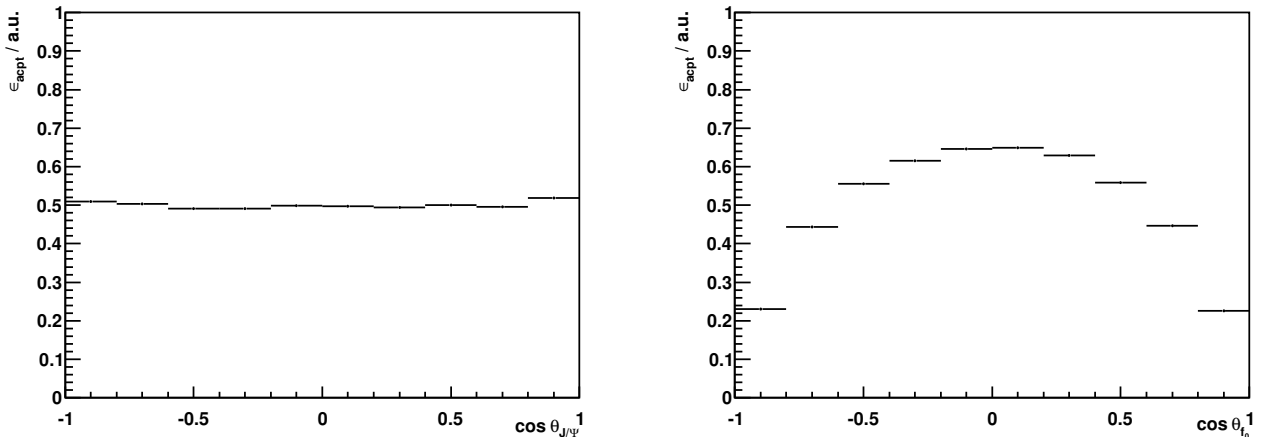


**Figure 5.14:** 1-dimensional projections of the angular acceptance as a function of  $\cos\theta_{J/\Psi}$ (left) and  $\cos\theta_{f_0}$ (right) in simulated  $B_s^0 \rightarrow J/\Psi f_0(980)$  decays

The acceptance as a function of  $\cos\theta_{J/\Psi}$  is almost constant while a drop is seen as a function of  $\cos\theta_{f_0}$  for  $\cos\theta_{f_0} \rightarrow \pm 1$ . Now, it can be used to correct the measured distributions obtained from data.

To select only  $B_s^0 \rightarrow J/\Psi f_0(980)$  candidates in data, the particular mass windows of the  $B_s^0$  and the  $f_0(980)$  peaks are chosen<sup>1</sup>. The background can be modeled by the wrong sign events, but for those the definition of the angle  $\theta_{f_0}$  is ambiguous due to the equal charges of the pions. Hence, the pion for which the angle is computed, is randomly chosen and the evolving distribution is subtracted from the right sign events to obtain the signal distribution. After dividing by the angular acceptance to account for detection efficiency, the data can be fitted with the angular distribution. The fit results are given in table 5.6 and the 1-dimensional projections of the background-subtracted and acceptance-corrected angular distributions are plotted in figure 5.15. The graphs of the fitted functions are provided by the integrated 1-dimensional distribution functions from equations 5.6 and 5.7 using the fitted parameters.

The description of the data by the theoretical distributions is very good. As assumed, the spin-0 amplitude is dominant with a small  $A_{20}$  contribution while the sum of the  $A_{2\pm 1}$  amplitudes is consistent with zero. This confirms that the selected  $\pi^+\pi^-$  states exhibit a spin of  $\mathbf{J} = 0$  which is consistent with the assumption that they originate from the  $f_0(980)$ . The small spin-2 contribution is mainly caused by higher resonances or can be a result of a wrong background subtraction.

<sup>1</sup> The mass of the  $B_s^0$  candidate is required to be in the mass window  $\pm 20$  MeV of the measured  $B_s^0$  mass of 5368.2 MeV and the mass of the  $f_0(980)$  candidate is required to lie in the range  $\pm 90$  MeV of the  $f_0(980)$  mass.

parameter	value
$\frac{X^2}{nDof}$	$\frac{99.2}{96}$
$ A_{00} ^2$	$0.341 \pm 0.016$
$\frac{ A_{20} ^2}{ A_{00} ^2}$	$0.062 \pm 0.043$
$\frac{ A_{21} ^2 +  A_{2-1} ^2}{ A_{00} ^2}$	$0.023 \pm 0.022$
$\delta$	$1.51 \pm 0.07$

**Table 5.6:** Fitted parameters from the 2-dimensional fit to the angular distributions of the background subtracted and acceptance corrected  $B_s^0 \rightarrow J/\Psi f_0(980)$  candidates

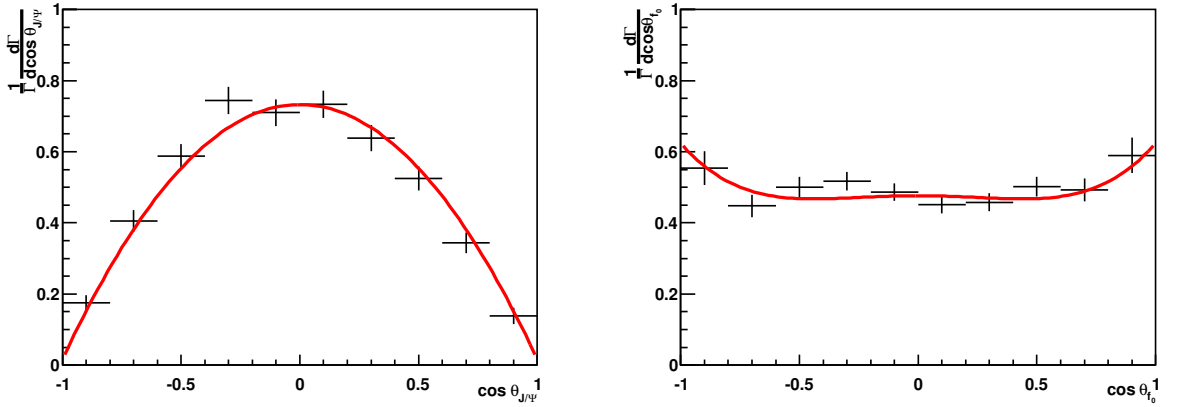


**Figure 5.15:** Angular distribution of  $\cos\theta_{J/\Psi}$  (left) and  $\cos\theta_{f_0}$  (right) for the background-subtracted and acceptance-corrected  $B_s^0 \rightarrow J/\Psi f_0(980)$  candidates with the 1-dimensional projections of the 2-dimensional fit.

The  $A_{2\pm 1}$  fraction of the total decay width  $\Gamma$  is computed as

$$\begin{aligned}
 \frac{|A_{21}|^2 + |A_{2-1}|^2}{|A_{00}|^2 + |A_{20}|^2 + |A_{21}|^2 + |A_{2-1}|^2} &= \frac{\frac{|A_{21}|^2 + |A_{2-1}|^2}{|A_{00}|^2}}{1 + \frac{|A_{20}|^2}{|A_{00}|^2} + \frac{|A_{21}|^2 + |A_{2-1}|^2}{|A_{00}|^2}} \\
 &= 0.022 \pm 0.020.
 \end{aligned} \tag{5.11}$$

As a result, it is assumed that the CP-even fraction of the selected final states  $J/\Psi\pi^+\pi^-$  in the mass region of the  $f_0(980)$  peak is  $2.2 \pm 2.0$  % and consistent with zero.

## 6 Time Resolution

In this chapter, the resolution of the measured  $B_s^0$  proper time for the selected  $B_s \rightarrow J/\Psi\pi^+\pi^-$  candidates is determined. The basic idea to determine the time resolution is to analyze the time distribution of prompt  $J/\Psi$ 's combined with two random pions that mimic a  $B_s^0$  candidate. Prompt particles are particles that are directly produced at the primary vertex (PV) and do not originate from the decay of another intermediate particle. The measured proper time of the reconstructed fake  $B_s^0$  should be zero assuming perfect resolution and that all particles come from the primary vertex but in reality, this determination is subject to uncertainties. Therefore, the width of the distribution of the reconstructed proper time is a measure of the time resolution. As discussed in the detector chapter, the proper time  $t_{prop}$  of a particle is computed from the determined production  $\vec{d}_{pr}$  and decay  $\vec{d}_{decay}$  vertices and from the momentum  $\vec{p}$  as<sup>1</sup>

$$t_{prop} = \frac{m(\vec{d}_{decay} - \vec{d}_{pr}) \cdot \vec{p}}{|\vec{p}|^2}, \quad (6.1)$$

where  $m$  is the reconstructed mass of the  $B_s^0$  candidate. The uncertainty of  $t_{prop}$  is dominated by the reconstruction of the vertices because the uncertainty of the momentum determination is small compared to that. In practice, the measured proper time distribution of particles reconstructed from fake  $B_s^0$ 's is concentrated around zero. Negative proper times are unphysical quantities but reflect the detector's resolution.

To use the time resolution from prompt events as time resolution for the  $B_s^0$  candidates, it has to be proven that they exhibit the same time resolution. This is done by comparing the time resolutions in simulation. Then the time resolution is determined with data applying both an average and a per event time resolution model.

### 6.1 Validation of the method on simulated events

In the first step, the time resolution for prompt  $J/\Psi$ 's combined with two prompt pions is compared to the time resolution of  $B_s \rightarrow J/\Psi\pi^+\pi^-$  candidates in simulation. For  $B_s \rightarrow J/\Psi\pi^+\pi^-$  decays, as explained before, several  $\pi^+\pi^-$ -resonances are involved but only simulated  $B_s \rightarrow J/\Psi f_0(980)$  decays are available. The simulation for the fake  $B_s^0$ 's is using proton-proton collisions in which at least one  $J/\Psi$  is produced. It is required to originate directly from the primary vertex. When combining it with two random pions to mimic a  $B_s^0$ , the same selection criteria as for the  $B_s \rightarrow J/\Psi\pi^+\pi^-$  decays are required except for the cuts on the flight distance, the impact parameter for the pions and the pointing angle of the  $B_s^0$  because they cut on the proper time. To describe the  $J/\Psi f_0$  kinematics, the invariant mass of the  $\pi^+\pi^-$  system is

---

<sup>1</sup> in natural units

restricted to the peak region of the  $f_0(980)$ .<sup>1</sup> The invariant mass of the fake  $B_s^0$ 's is chosen to lie in the peak region of the  $B_s^0$ .<sup>2</sup>

In simulations, the proper time  $t_{prop}$  measured by the detector can be easily compared with the true proper time  $t_{gen}$  which has been generated for a  $B_s^0$  or fake  $B_s^0$ . The width of the distribution of  $\Delta t = t_{prop} - t_{gen}$  then gives the time resolution. The  $\Delta t$  distribution of simulated prompt  $J/\Psi$ 's +  $\pi^+\pi^-$  and  $B_s^0 \rightarrow J/\Psi f_0(980)$  decays are given in figure 6.1. The resolution is modeled by a triple Gaussian  $TG(t)$ ,

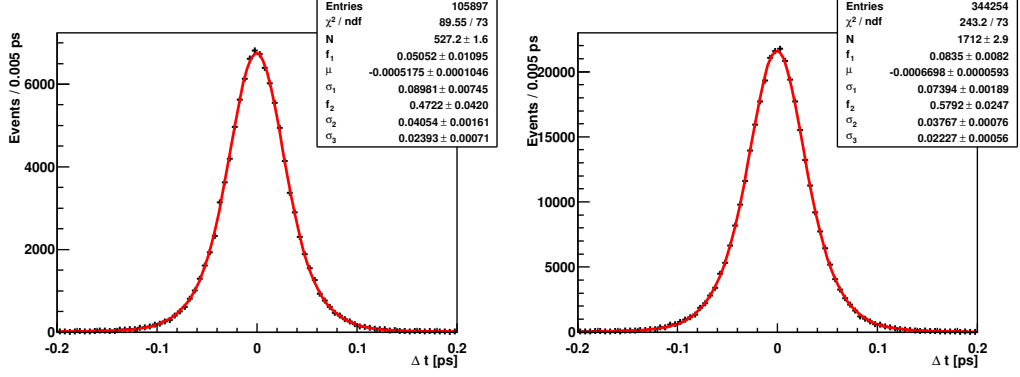


**Figure 6.1:**  $\Delta t$  distribution of simulated prompt  $J/\Psi$ 's +  $\pi^+\pi^-$  (left) and  $B_s^0 \rightarrow J/\Psi f_0$  decays(right) fitted with a triple Gaussian  $TG(t)$  model

which is defined as:

$$\begin{aligned}
 TG(t; f_1, f_2, \sigma_1, \sigma_2, \sigma_3) = & \frac{f_1}{\sqrt{2\pi}\sigma_1} \exp\left(-\frac{(t-\mu)^2}{2\sigma_1^2}\right) \\
 & + \frac{f_2}{\sqrt{2\pi}\sigma_2} \exp\left(-\frac{(t-\mu)^2}{2\sigma_2^2}\right) \\
 & + \frac{1-f_1-f_2}{\sqrt{2\pi}\sigma_3} \exp\left(-\frac{(t-\mu)^2}{2\sigma_3^2}\right), \quad (6.2)
 \end{aligned}$$

where  $\sigma_i$ ,  $i = 1,2,3$  are the three widths,  $f_1$ ,  $f_2$  and  $f_3 = 1 - f_1 - f_2$  the fractions of the three Gaussians and  $\mu$  the central value to allow a tiny deviation from zero. The average width  $\bar{\sigma}_{\Delta t}$  of the triple Gaussian is calculated by weighting the single widths with their fractions:

$$\bar{\sigma}_{\Delta t} = \sqrt{\sum_{i=1}^3 f_i \sigma_i^2}. \quad (6.3)$$

The average width  $\bar{\sigma}_{\Delta t}$  is the resulting width if a single Gaussian is used to describe the time distribution.

<sup>1</sup> i.e. between 890 and 1070 MeV.

<sup>2</sup> within  $\pm 20$  MeV of the  $B_s^0$  PDG [2] mass of 5366.77 MeV.

The effect of a finite time resolution on the measurement of the phase  $\phi_s$  is an effective dilution of the observable  $B_s^0 - \bar{B}_s^0$  mixing amplitude. The dilution factor  $D$  is the Fourier transform of the resolution function and for the triple Gaussian resolution model  $TG(t)$ , one obtains [32]:

$$D_{TG} = \sum_{i=1}^3 f_i \exp\left(-\frac{\Delta m_s^2 \sigma_i^2}{2}\right), \quad (6.4)$$

where  $\Delta m_s = 17.63 \pm 0.11 \text{ ps}^{-1}$  [15]<sup>1</sup> and  $f_i$  and  $\sigma_i$  as above. If this dilution  $D_{TG}$  is used within a single Gaussian resolution model, the effective width  $\sigma_{effective}$  of the single Gaussian is computed by solving equation 6.4<sup>2</sup> for  $\sigma$ :

$$\sigma_{effective} = \frac{\sqrt{-2 \ln D_{TG}}}{\Delta m_s}. \quad (6.5)$$

It describes the effective time resolution in the measurement of the phase  $\phi_s$ .

The average and effective widths  $\bar{\sigma}_{\Delta t}$  and  $\sigma_{effective}$  of the simulated  $\Delta t$  distributions are listed in table 6.1.

	<b>prompt <math>J/\Psi</math>'s + <math>\pi^+\pi^-</math></b>	$B_s^0 \rightarrow J/\Psi f_0(980)$
$\bar{\sigma}_{\Delta t}$	$0.0382 \pm 0.0019 \text{ ps}$	$0.0380 \pm 0.0009 \text{ ps}$
$\sigma_{effective}$	$0.0361 \pm 0.0004 \text{ ps}$	$0.0365 \pm 0.0003 \text{ ps}$

**Table 6.1:** Average and effective widths  $\bar{\sigma}_{\Delta t}$  and  $\sigma_{effective}$  of the simulated  $\Delta t$  distributions obtained from figure 6.1 with equations 6.3 and 6.5

The average and effective widths of the two simulated  $\Delta t$  resolutions are almost identical. The estimated effective time resolution obtained from simulated  $B_s^0 \rightarrow J/\Psi f_0(980)$  decays is  $36.5 \pm 0.3 \text{ fs}$ .

### Event-dependent resolution model

The widths  $\sigma_i$ ,  $i = 1, 2, 3$  of the triple Gaussians are computed here in average for all events and they are described by an *Average Resolution Model*. As the time resolution of the detector depends on the measured proper time itself, it is more correct to use an event-dependent resolution model. An estimation of the measured proper time uncertainty  $\sigma_{ct}$  of every individual event is provided by time reconstruction algorithms and is based on the kinematics of the decay. Figure 6.2 shows the measured  $\sigma_{ct}$  of the selected  $B_s^0 \rightarrow J/\Psi + \pi^+\pi^-$  decays obtained from data as a function of the proper time. From now on,  $t$  shortly denotes the proper time  $t_{prop}$ .

An increasing trend in  $\sigma_{ct}$  can be seen. The problem of the event-based uncertainty is that the relative variations from event to event are correctly described but that their average errors do not agree with what one measures in the average resolution model. Therefore, the event resolutions  $\sigma_{ct}$  are corrected for by three scaling factors  $s_i$  by the *Per Event Resolution Model*,

<sup>1</sup>  $\Delta m_s$  is the mixing frequency of the  $B_s^0$   
<sup>2</sup> with  $f_1 = 1$  and  $f_2 = f_3 = 0$

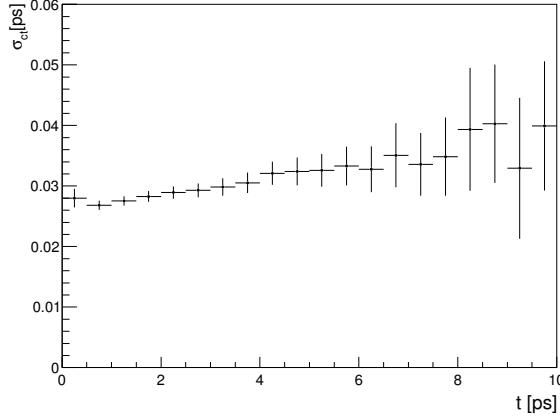


**Figure 6.2:** Estimated proper time uncertainty  $\sigma_{ct}$  as a function of the proper time  $t$  for all selected  $B_s^0 \rightarrow J/\Psi\pi^+\pi^-$  candidates obtained from data (including background)

so that the widths of the triple Gaussian  $TG(t)$  are computed as  $\sigma_i = s_i \cdot \sigma_{ct}$ . Since this is done for every event, the complete per event resolution model  $TG_{ev}(t)$  is proportional to the sum of three Gaussian functions over all events<sup>1</sup>:

$$TG_{ev}(t, \sigma_{ct}, f_1, f_2, s_1, s_2, s_3) \propto \sum_{i=1}^{N_{events}} \left\{ \frac{f_1}{\sqrt{2\pi} s_1 \sigma_{ct,i}} \exp\left(-\frac{(t-\mu)^2}{2(s_1 \sigma_{ct,i})^2}\right) + \frac{f_2}{\sqrt{2\pi} s_2 \sigma_{ct,i}} \exp\left(-\frac{(t-\mu)^2}{2(s_2 \sigma_{ct,i})^2}\right) + \frac{1-f_1-f_2}{\sqrt{2\pi} s_3 \sigma_{ct,i}} \exp\left(-\frac{(t-\mu)^2}{2(s_3 \sigma_{ct,i})^2}\right) \right\} \quad (6.6)$$

where  $N_{events}$  is the number of events.

Since the per event resolution model uses the uncertainty of the proper time fit  $\sigma_{ct}$ , it is also necessary to compare these uncertainties in the two simulations if one wants to apply the model on data. As the estimated uncertainties depend on the measured proper time, they cannot be compared directly but only relative to the proper time. The pull distribution that has been introduced in chapter 5.5 in equation 5.4 gives the relation of the measured  $\Delta t$  value to its uncertainty  $\sigma_{ct}$ . If the uncertainty is correctly estimated, the pull distribution exhibits a width of 1. If it is larger, the uncertainty is underestimated and has to be corrected for as it is done by the per event resolution model. The pull distributions  $\Delta t/\sigma_{ct}$  of the two simulations are given in figure 6.3.

They are modeled by the sum of two Gaussian functions with dimensionless widths. Two Gaussians instead of three are chosen because the tails in the pull distributions are less pronounced than in the  $\Delta t$  distributions. The average width  $\bar{\sigma}_{pull}$  of the pull distribution is calculated by weighting the two widths with their fractions:

<sup>1</sup> it still has to be correctly normalised

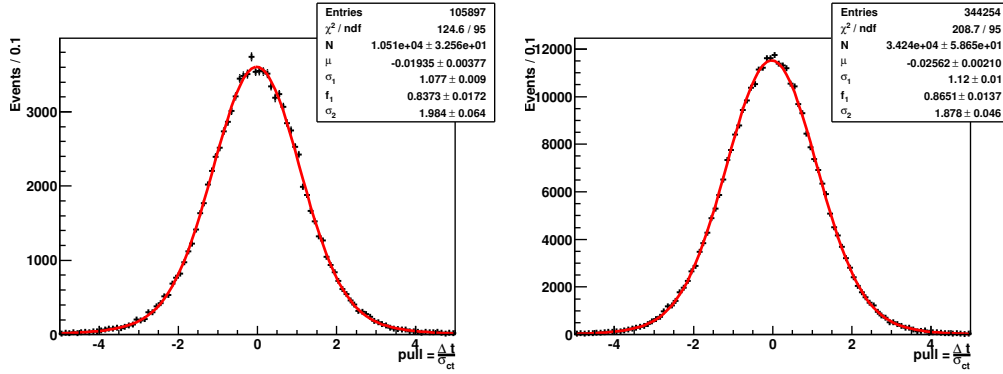


**Figure 6.3:** Pull distributions  $\Delta t/\sigma_{ct}$  of simulated prompt  $J/\Psi$ 's  $+\pi^+\pi^-$  (left) and  $B_s^0 \rightarrow J/\Psi f_0$  decays(right) fitted with a double Gaussian function

$$\bar{\sigma}_{pull} = \sqrt{\sum_{i=1}^2 f_i \sigma_i^2}. \quad (6.7)$$

For the two simulations, they are given in table 6.2.

	prompt $J/\Psi$ 's $+\pi^+\pi^-$	$B_s^0 \rightarrow J/\Psi f_0(980)$
$\bar{\sigma}_{pull}$	$1.270 \pm 0.022$	$1.249 \pm 0.017$

**Table 6.2:** Average widths  $\bar{\sigma}_{pull}$  for the pull distributions  $\Delta t/\sigma_{ct}$  obtained from figure 6.3

Considering the uncertainties, the average widths of the pull distributions are also well compatible with each other but they are larger than 1, i.e. the time reconstruction algorithms underestimate the uncertainty of the proper time measurement and it is reasonable not to use them uncorrected.

The prompt events can be used to determine the time resolution on data which is dealt with in the next two chapters. Although the widths of the pull distributions agree with each other, the relative difference of the two average widths  $\bar{\sigma}_{pull}$  will serve as a systematic uncertainty of the measured scaling factors  $s_i$ . Varying them within the observed differences will be studied as a systematic uncertainty when determining  $\phi_s$ .

## 6.2 Time Resolution on data

After having shown that it is possible to use prompt fake  $B_s^0$ 's composed from a prompt  $J/\Psi$  and two prompt pions to obtain the time resolution for  $B_s^0 \rightarrow J/\Psi \pi^+\pi^-$ , the procedure is applied on data. The selection requirements are modified to also select prompt background candidates.<sup>1</sup> Besides long-lived  $B$  decays like the signal  $B_s^0 \rightarrow J/\Psi \pi^+\pi^-$ , the selected events

<sup>1</sup> The cuts on the flight distance, the impact parameter for the pions and the pointing angle of the  $B_s^0$  are not required. The invariant mass of the fake  $B_s^0$  is required to lie in the  $B_s^0$  peak region within  $\pm 20$  MeV of the

now consist mainly of prompt  $J/\Psi$ 's and prompt non- $J/\Psi$  background combined with two random pions.

This non- $J/\Psi$  background has to be subtracted before the resolution parameters can be determined. This is done by using the sFit-technique [16] described in the following. The  $J/\Psi$  candidate mass distribution is fitted with the sum of two Gaussian functions

$$DG(m_{\mu^+\mu^-}) \propto f_{sig} \left\{ f_1 \exp\left(-\frac{(m_{\mu^+\mu^-} - m_{J/\Psi})^2}{2\sigma_1^2}\right) + (1 - f_1) \exp\left(-\frac{(m_{\mu^+\mu^-} - m_{J/\Psi})^2}{2\sigma_2^2}\right) \right\} \quad (6.8)$$

for signal that has already been introduced in chapter 5.5 to describe the B signal peaks. The background is described by an exponential decay function

$$N_{exp}(m_{\mu^+\mu^-}) \propto (1 - f_{sig}) e^{-\alpha m_{\mu^+\mu^-}}, \quad (6.9)$$

where  $f_{sig}$  is the signal fraction compared to the background fraction  $1 - f_{sig}$ .<sup>2</sup> The invariant mass distribution of the two muons with the fitted functions is shown in figure 6.4 and the corresponding fitted parameters in table 6.3.

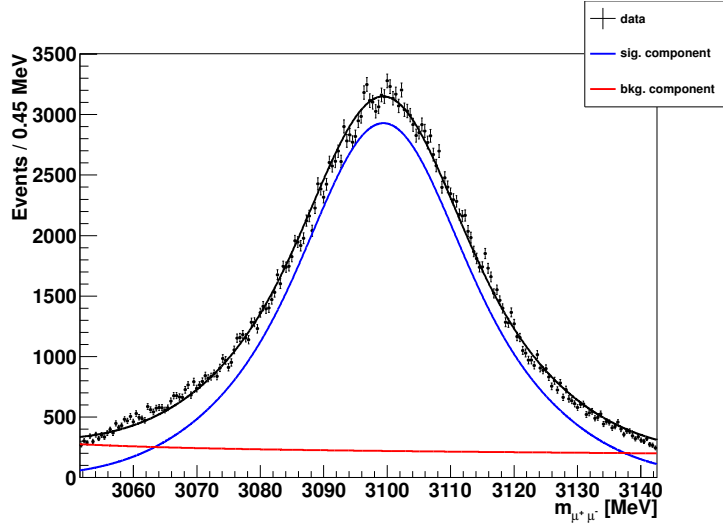


**Figure 6.4:** Invariant mass distribution of the  $\mu^+\mu^-$  system described by a double Gaussian function for signal and an exponential decay function for background

Then, according to this fit result, every single event is assigned a weight which can be positive or negative, so that the mass distribution of these weighted events constitutes the  $J/\Psi$  signal mass distribution. Thus, the contribution from non- $J/\Psi$  background is subtracted on a statistical basis. These weights are called sweights [16].

Besides the non- $J/\Psi$  background, long-lived particles like the  $B_s^0$  signal or misreconstructed B-decays are still selected and present in these events. This long-lived background component

measured  $B_s^0$  mass of 5368.2 MeV. The selected mass range of the  $\pi^+\pi^-$  system covers the whole region from 775 - 1550 MeV.

<sup>2</sup>  $f_1$  is the fraction of the first Gaussian,  $\sigma_i$  the two widths of the Gaussian functions and  $\alpha$  the decay constant.

parameter	value
$f_{sig}$	$0.8378 \pm 0.0074$
$m_{J/\Psi}$	$3099.41 \pm 0.04 \text{ MeV}$
$f_1$	$0.717 \pm 0.023$
$\sigma_1$	$18.54 \pm 0.40 \text{ MeV}$
$\sigma_2$	$9.52 \pm 0.15 \text{ MeV}$
$\alpha$	$0.0581 \pm 0.0084 \text{ MeV}^{-1}$

**Table 6.3:** Fit results of the fit to the  $J/\Psi$  candidate mass distribution

is not described by the resolution model  $TG(t)$  of equation 6.2 and is modeled by the sum of two exponential decay functions. To account for time resolution effects of this component, it is convoluted with the resolution function  $TG(t)$  where the convolution  $\otimes$  is defined as

$$(f \otimes g)(t) = \int_{-\infty}^{\infty} f(\tau) g(t - \tau) d\tau. \quad (6.10)$$

To describe the proper time distribution of the prompt events and the long-lived component, one obtains the calibration function

$$R_{calibration}(t) \propto f_{pr} \cdot TG(t) + (1 - f_{pr}) \left\{ f_1^b \left( \frac{1}{\tau_1} \exp(-t/\tau_1) \otimes TG(t) \right) + (1 - f_1^b) \left( \frac{1}{\tau_2} \exp(-t/\tau_2) \otimes TG(t) \right) \right\}, \quad (6.11)$$

where  $f_{pr}$  is fraction of the prompt compared to the fraction of the long-lived decays,  $f_1^b$  the fraction of the first exponent and  $\tau_i$  the lifetimes. A potential deviation  $\mu$  from the zero in  $TG(t)$ (6.2) is ignored since an absolute shift of the resolution function is not relevant for the resolution model. The average resolution model or the per event resolution model can be applied within the triple Gaussian  $TG(t)$ . A single long-lived component would not be sufficient because the various long-lived particles exhibit different lifetimes that are merged in two effective lifetimes that describe the data better but still not perfectly.

### 6.2.1 Average time resolution

Applying the average resolution model, the calibration function  $R_{calibration}(t)$  of equation 6.11 including the triple Gaussian describing the resolution, is fitted to the proper time distribution of the  $J/\Psi\pi^+\pi^-$  decays in the range from -1.2 – 2.5 ps. Figure 6.5 shows the distribution and table 6.4 gives the corresponding fit results. The number of events in one bin can be below 1 because the events are weighted in the sFit procedure. The data is described very well in the core of the distribution but lies slightly beneath the fit at higher proper times. Considering that the distribution is plotted with a logarithmic scaling over 6 orders of magnitude and that the model of the long-lived component is only an effective description, the fit result is acceptable.

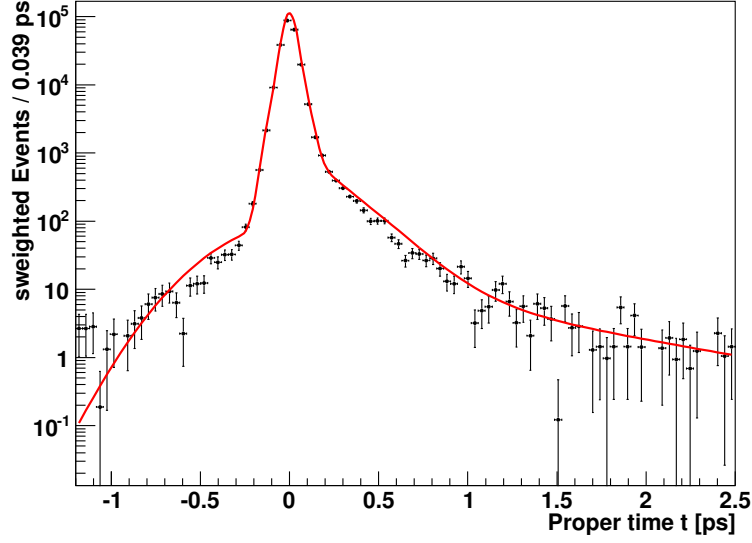


**Figure 6.5:** Proper time distribution of prompt  $J/\Psi + \pi^+\pi^-$  events fitted with the average time resolution model within the calibration function  $R_{calibration}(t)$  of equation 6.11

parameter	value
$f_{pr}$	$0.9763 \pm 0.0007$
$f_1$	$0.6862 \pm 0.004$
$f_2$	$0.3073 \pm 0.005$
$\sigma_1$	$0.0316 \pm 0.00011$ ps
$\sigma_2$	$0.0618 \pm 0.0003$ ps
$\sigma_3$	$0.323 \pm 0.015$ ps
$f_1^b$	$0.950 \pm 0.011$
$\tau_1$	$0.186 \pm 0.024$ ps
$\tau_2$	$0.96 \pm 0.32$ ps

**Table 6.4:** Fit results applying the average time resolution model for prompt  $J/\Psi\pi\pi$  decays using the calibration function  $R_{calibration}(t)$  of equation 6.11

The effective time resolution  $\sigma_{effective}$  is computed with equation 6.5 as  $42.2 \pm 0.3$  fs which is slightly worse than the expected 36 fs in the simulation.

### 6.2.2 Per event time resolution

Figure 6.6 and table 6.5 show the results of the fit applying the per event resolution model within the calibration function  $R_{calibration}(t)$  6.11. The fit still lies slightly above the data at high proper times but the description is better. Except for the edge at -0.3 ps, the core and the negative range are described fairly well.

The effective time resolution  $\sigma_{effective}$  is calculated with equation 6.5 as  $42.6 \pm 0.9$  fs which agrees with the time resolution computed with the average resolution model.

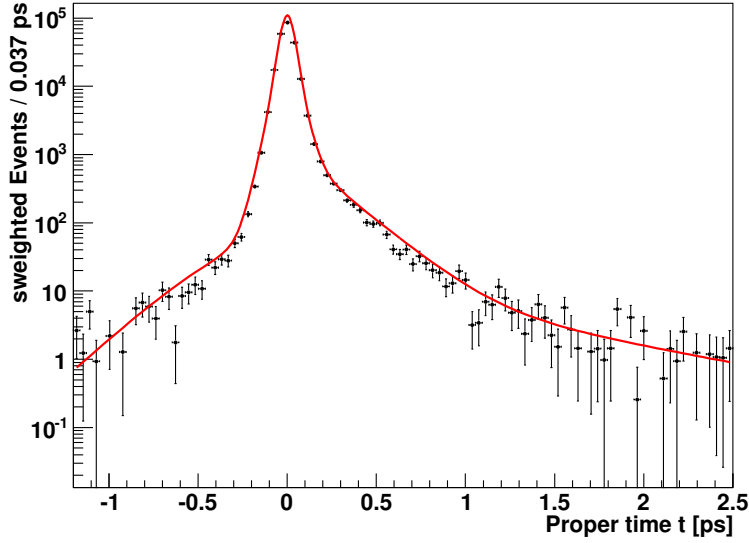


**Figure 6.6:** Proper time distribution of prompt  $J/\Psi + \pi^+\pi^-$  events fitted with the per event time resolution model within the calibration function  $R_{calibration}(t)$  of equation 6.11

parameter	value
$f_{pr}$	$0.9781 \pm 0.0007$
$f_1$	$0.8184 \pm 0.0079$
$f_2$	$0.1767 \pm 0.009$
$s_1$	$1.2951 \pm 0.0066$
$s_2$	$2.601 \pm 0.039$
$s_3$	$13.61 \pm 0.14$
$f_1^b$	$0.947 \pm 0.008$
$\tau_1$	$0.188 \pm 0.006$ ps
$\tau_2$	$0.90 \pm 0.22$ ps

**Table 6.5:** Fit results applying the per event time resolution model for prompt  $J/\Psi\pi\pi$  decays within the calibration function  $R_{calibration}(t)$  of equation 6.11

To determine the phase  $\phi_s$ , the per event resolution model will be applied because it accounts for the dependence of time resolution of the measured proper time. But since the resolution has to be computed for each event, the fit procedure is a lot more CPU time-consuming than for the average resolution model. Thus, the average resolution model is used in the toy studies described later in chapter 10.7 where a lot of fits are to be done. As described above, the difference of the simulated pull distributions and the statistical uncertainties of the scaling factors  $s_i$  will be used to study the systematic uncertainties of the determination of  $\phi_s$ .

## 7 Determination of the time acceptance correction

As discussed before, the event selection profits from the fact that the  $B_s^0$  lifetime is so large that the flight distance between the production and the decay vertex can usually be resolved. Decays in which the decay products, the muons and the pions, appear to originate from the primary vertex, are removed so that the signal proper time distribution becomes distorted. The *proper time acceptance* describes the efficiency of selecting the signal decays as a function of proper time  $t$  and can be defined as the proper time dependent ratio of selected and produced signal particles:

$$\epsilon_{time}(t) = \frac{\# \text{ of selected } B_s^0(t)}{\# \text{ of produced } B_s^0(t)}. \quad (7.1)$$

In data, the total number of produced  $B_s^0$  is not known. The kinematically similar channel  $B^0 \rightarrow J/\Psi K^*(892)$  is used to model the time acceptance. The advantages of this decay are the excellent signal-to-background ratio, a high statistics and the well-known lifetime of the  $B^0$ . The number of produced  $B^0$ 's is not known as well. Instead, the shape of the proper time distribution of the produced  $B^0$ 's is taken as an exponential decay function with the PDG [2] lifetime of 1.519 ps. The proper time distribution of the selected  $B^0$ 's denoted as  $N_{B^0}(t)$  can be described by the fixed exponential decay function corrected by the time acceptance:

$$N_{B^0}(t) = \epsilon_{time}(t) \cdot \frac{1}{\tau_{PDG}} \exp\left(-\frac{t}{\tau_{PDG}}\right). \quad (7.2)$$

For the  $B_s^0$  signal events this cannot be done because the lifetime is not known precisely enough and is part of the parameters that will be determined in the fit for  $\phi_s$ .<sup>1</sup>

The event selection for  $B^0 \rightarrow J/\Psi K^*(892)$  uses the same cuts as for  $B_s^0 \rightarrow J/\Psi \pi^+ \pi^-$  decays except for the delta-log likelihood  $\Delta \ln \mathcal{L}$  for particle identification of the Kaon and the mass of the  $K^*$  and  $B^0$  candidates.<sup>2</sup> Variations of the analysis selection are given in table 7.1.

Before the  $B^0 \rightarrow J/\Psi K^*(892)$  events can be used to determine the time acceptance, it has to be shown that the time acceptance for  $B_s^0 \rightarrow J/\Psi \pi^+ \pi^-$  and for  $B^0 \rightarrow J/\Psi K^*(892)$  are the same. This is done for simulated events.

<sup>1</sup> Due to the light and heavy mass eigenstates  $B_L$  and  $B_H$  and a non-trivial difference  $\Delta \Gamma_s$  of the decay widths, there are even two different  $B_s^0$  lifetimes

<sup>2</sup> The decay is reconstructed as  $B^0 \rightarrow J/\Psi K^*(892)$  and not as  $B_s^0 \rightarrow J/\Psi \pi^+ \pi^-$  as it has been done in chapter 5.3

quantity	selection cut
$\Delta \ln \mathcal{L}_{K-\pi}$ (Kaon)	$> 0$
$m_{K^*}$	592 – 1192 MeV
$m_{B^0}$	5245 – 5315 MeV

**Table 7.1:** Changed selection criteria for  $B^0 \rightarrow J/\Psi K^*(892)$ . The other cuts are the same as in table 5.1

## 7.1 Comparison of $B_s^0 \rightarrow J/\Psi f_0(980)$ and $B^0 \rightarrow J/\Psi K^*(892)$ time acceptance in simulated data

In this chapter, the time acceptances of simulated  $B^0 \rightarrow J/\Psi K^*(892)$  and  $B_s^0 \rightarrow J/\Psi f_0(980)$  decays are compared. For fully simulated events, the generated particles and their properties are accessible independent of the simulated detector response. In addition to the selection criteria, the B's are required to be correctly reconstructed. The proper time distribution taken from the generator information of the selected B's is divided by the generated proper time distribution of all B's. For both distributions, no resolution effects are present. Figure 7.1 shows the time acceptances. The histograms are normalised for comparison.

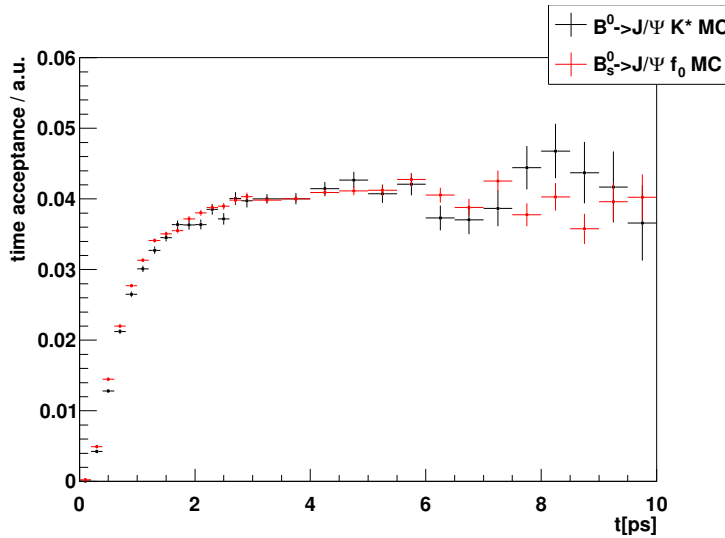


**Figure 7.1:** Time Acceptances of  $B^0 \rightarrow J/\Psi K^*(892)$  (black) and  $B_s^0 \rightarrow J/\Psi f_0$ (red) from fully simulated events

At very low proper times, the acceptances are zero due to the time-dependent selection cuts. Then, the acceptance rises steeply until it reaches a constant value where a maximum fraction of the produced B's can be detected and selected. It can be observed in the plot that the acceptances for the two channels are not exactly the same and the  $f_0$  time acceptance appears to rise slightly faster, but the differences are not precarious considering the very steep rise at

low proper times. The acceptances are described by the following function [40]:

$$A(t) = C \frac{[a(t - t_0)]^n}{1 + [a(t - t_0)]^n}, \quad (7.3)$$

in which the parameter  $t_0$  marks the offset at which the function becomes non-zero at low proper times and  $a$  and  $n$  are parameters responsible for the steep slope until it reaches the constant value  $C$ . Figure 7.2 shows the fit of the function to the acceptances and the fitted parameters.

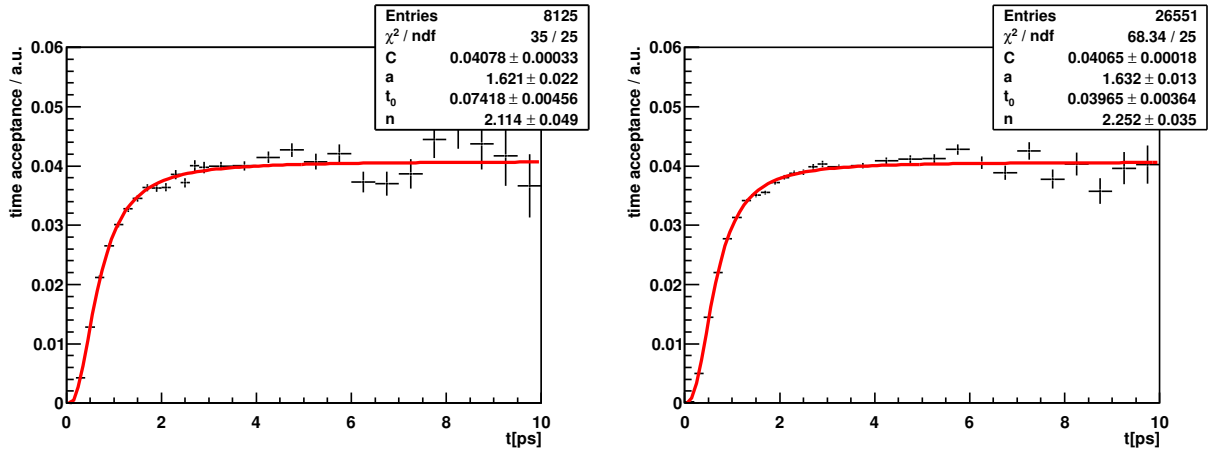


**Figure 7.2:** Time Acceptances of  $B^0 \rightarrow J/\Psi K^*(892)$  (left) and  $B_s^0 \rightarrow J/\Psi f^0$  (right) from fully simulated events fitted with the acceptance function  $A(t)$  of equation 7.3

The results reflect the slight differences in the acceptances of the two channels. While parameter  $a$  is in good agreement,  $t_0$  and  $n$  do not agree within their uncertainties. In the correlation matrices in table 7.2 and especially in table 7.3, it can be seen that  $t_0$  and  $n$  are strongly correlated which can be caused by an over-parameterisation of the function. Due to the significant correlation, the fit results for the two parameters depend on the start values and of settings of the fit.

	<b>a</b>	$t_0$	<b>n</b>
<b>a</b>	1	0.311	0.213
$t_0$	0.311	1	-0.73
<b>n</b>	0.213	-0.73	1

**Table 7.2:** Correlation Matrix of the time acceptance fit for  $B^0 \rightarrow J/\Psi K^*(892)$  simulated decays

Since for the final analysis, an additional proper time cut will remove events with proper times larger than 0.3 ps, the fit is repeated when applying this cut and shown in figure 7.3.

Now, the parameters  $n$ ,  $t_0$  and  $a$  are compatible within their statistical uncertainties. From this result it is concluded that the time acceptance of the channel  $B^0 \rightarrow J/\Psi K^*(892)$  can be used to model the acceptance of  $B_s^0 \rightarrow J/\Psi \pi^+ \pi^-$  decays. The parameters of the

	<b>a</b>	$t_0$	<b>n</b>
<b>a</b>	1	0.502	-0.124
$t_0$	0.502	1	-0.850
<b>n</b>	-0.124	-0.850	1

**Table 7.3:** Correlation Matrix of the time acceptance fit for  $B_s^0 \rightarrow J/\Psi f_0(980)$  simulated decays

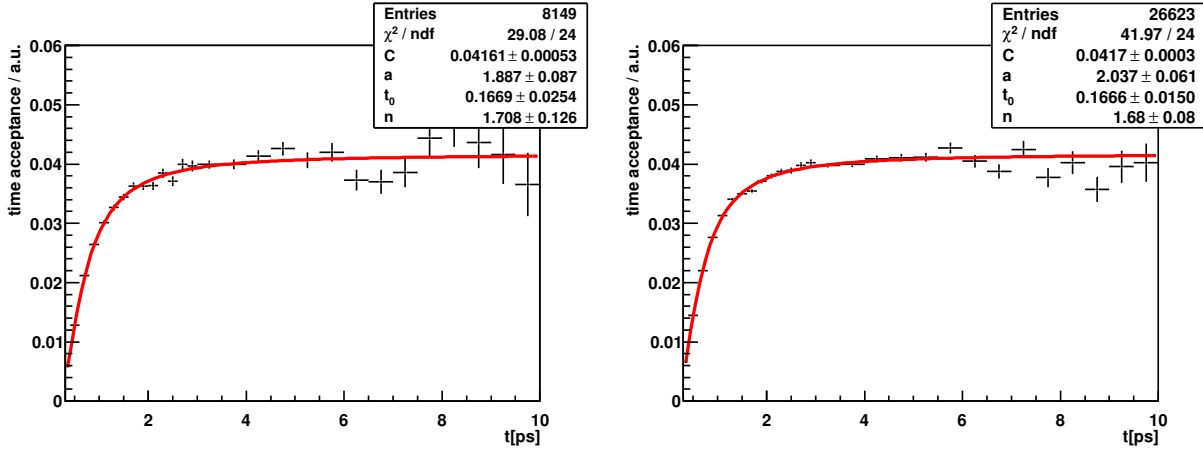


**Figure 7.3:** Time Acceptances of  $B^0 \rightarrow J/\Psi K^*(892)$  (left) and  $B_s^0 \rightarrow J/\Psi f^0$  (right) from fully simulated events when applying an additional proper time cut at 0.3 ps

functional description will be varied within the observed differences in figure 7.2 to estimate the systematic uncertainties when determining  $\phi_s$ .

## 7.2 Determination of the time acceptance using $B^0 \rightarrow J/\Psi K^*(892)$ decays in data

The time acceptance is determined using  $B^0 \rightarrow J/\Psi K^*(892)$  decays that have been collected in 2011. Again, the event selection of  $B_s^0 \rightarrow J/\Psi \pi^+ \pi^-$  decays is only modified to select  $B^0 \rightarrow J/\Psi K^*(892)$  decays according to table 7.1. In the invariant mass distribution of the  $B^0$  candidates in figure 7.4 it can be seen that the  $B^0 \rightarrow J/\Psi K^*(892)$  channel is characterised by a very low background fraction and a very high number of signal events. In order to subtract the small background, the mass distribution is fitted with the sum of two Gaussian functions<sup>1</sup> for signal and a constant value  $C$  to account for the background.  $N_B$  refers to the number of  $B^0$ 's,  $f_1$  is the fraction of the first Gaussian and  $\sigma_i$  the widths of the two Gaussian functions. In the plot, the  $B^0$  signal component is given in blue, the constant background in green and the total fit in red.

The fit yields  $62560 \pm 248$   $B^0$  signal events and a  $B^0$  mass of 5281 MeV. The  $B^0$  signal peak region is chosen in the mass range 5245 – 5315 MeV. The sidebands outside the signal

<sup>1</sup> The sum of two Gaussian function has already been introduced in chapter 5.5 in equation 5.2

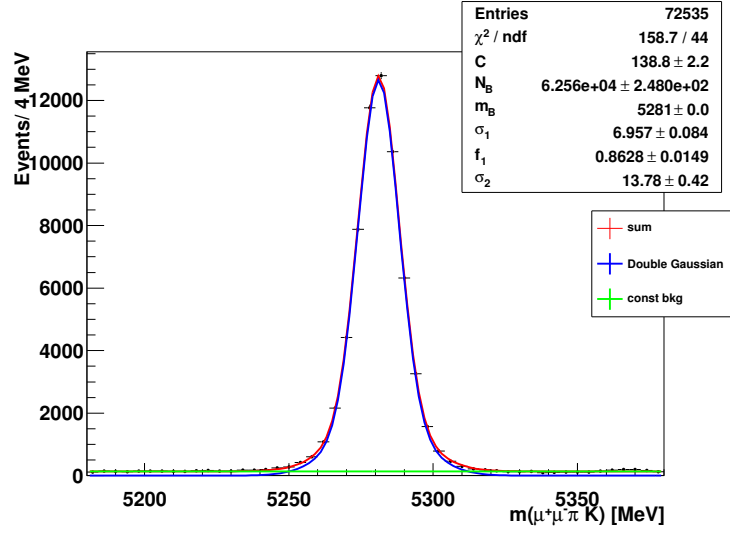


**Figure 7.4:** Invariant mass distribution of selected  $\mu^+\mu^-K\pi$  candidates fitted with a double Gaussian function and constant background C

region but within 5150 – 5450 MeV are taken as background. The proper time distribution of the candidates in the sidebands is scaled to the peak window width and subtracted from the distribution of the candidates in the signal region. Thus, the background is statistically subtracted and one gets the proper time distribution  $N(t)$  of the signal candidates. It can be described by an exponential decay time function with the PDG [2] lifetime of 1.519 ps that is multiplied with the acceptance function  $A(t)$  of equation 7.3. To account for time resolution, it is convoluted with the resolution model  $TG(t)$  with the average time resolution parameters determined in the previous chapter:

$$N(t) = N \frac{[a(t - t_0)]^n}{1 + [a(t - t_0)]^n} \cdot \frac{1}{\tau_{PDG}} \exp\left(-\frac{t}{\tau_{PDG}}\right) \otimes TG(t), \quad (7.4)$$

where  $N$  is a normalisation parameter. The function is fitted to the signal distribution with the acceptance parameters floating. Assuming for the  $B^0 \rightarrow J/\Psi K^*(892)$  decays the same resolution as for  $B_s^0 \rightarrow J/\Psi \pi^+ \pi^-$  is an approximation. In order to demonstrate that the influence of the resolution is negligible, the fit is done twice: First with the measured time resolution on the left of figure 7.5 and ignoring time resolution effects totally on the right. The results are exactly the same and the function describes the data excellently. The parameters are determined to be  $a = 1.91 \pm 0.03$ ,  $n = 1.84 \pm 0.05$  and  $t_0 = 0.135 \pm 0.005$  ps. In the determination of the phase  $\phi_s$ , the acceptance function  $A(t)$  with these fixed parameters will be used to describe the time acceptance of the signal component of the  $B_s^0 \rightarrow J/\Psi \pi^+ \pi^-$  decays. Due to the differences in simulation discussed in the previous chapter, a possible systematic bias is introduced that will be investigated by varying the acceptance parameters.

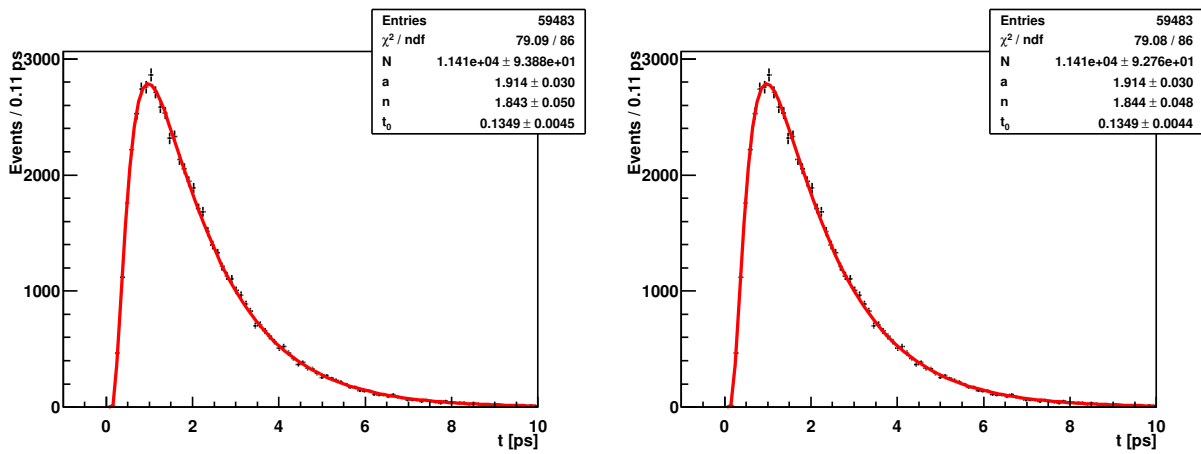


**Figure 7.5:** Background-subtracted proper time distribution of the  $B^0$  candidates fitted with a time acceptance corrected exponential decay function with  $\tau_{PDG} = 1.519$  ps with measured time resolution from  $B_s^0 \rightarrow J/\Psi \pi^+ \pi^-$  (left) and ignoring resolution effects(right)

## 8 Proper time description of the background

This chapter studies the proper time distribution of the background components. It is shown that the upper mass sideband of the  $B_s^0$  has the same proper time behaviour as the wrong sign events that model the combinatorial background. This combinatorial background is observed to be composed of a prompt and a long-lived component that have to be modeled separately. Therefore, a cut on the proper time to remove the prompt events at low proper times is introduced. The shape of the PDF describing the time behaviour of the long-lived background component is determined after applying this time cut.

### 8.1 Proper time distributions of background events

As discussed in section 5.5, the lower sideband in the  $B_s^0$  mass distribution has a large fraction of other resonant B-decays while in the signal region and the upper sideband, the background appears to be solely composed of combinatorics neglecting a very small  $B_s^0 \rightarrow J/\Psi\eta'$  component. Thus, for the determination of the phase  $\phi_s$ , only events in the  $B_s^0$  candidate mass region from 5320 - 5600 MeV are selected. Figure 8.1 compares the proper time distribution of right sign with wrong sign events in the lower mass sideband (5100-5320 MeV (left)) and the upper mass sideband (5410-5600MeV(right)). The histograms are normalised for comparison.

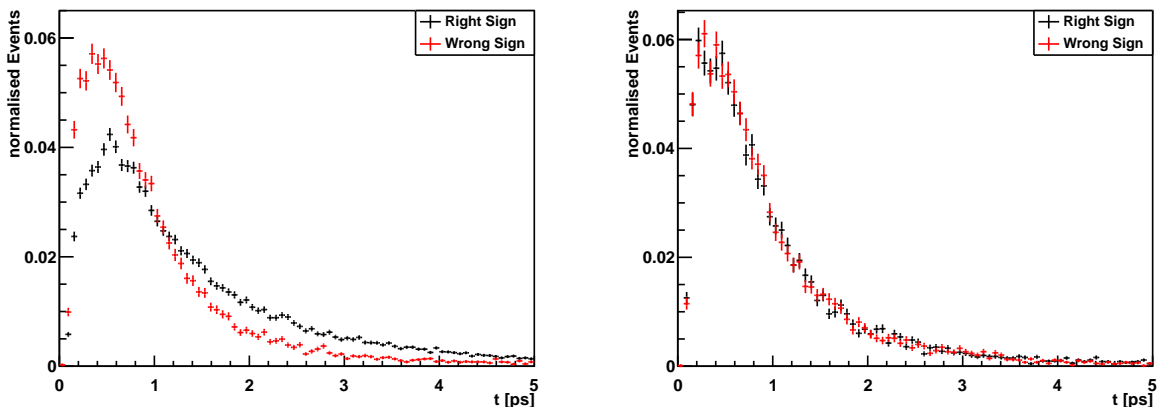


**Figure 8.1:** Proper time distribution of WS and RS events in the lower(5100-5320 MeV(left)) and the upper sideband((5410-5600MeV(right))) in the  $B_s^0$  mass distribution

In the lower mass sideband, the proper time distribution cannot be described by the combinatorial background while in the upper mass sideband, they agree.

## 8.2 Determination of the proper time shape of the background

Since there is no theoretical prediction, the proper time shape of the background is chosen to be the sum of two exponential decay functions that has already been used when the time resolution was determined on data. It is an effective description of the various lifetimes. The effect of the finite time resolution is accounted for by convoluting the exponential decay with the resolution model  $TG(t)$  applying the average resolution model. The proper time acceptance of the background is modeled by the acceptance function  $A(t)$  of equation (7.3) using new parameters  $a_b$ ,  $n_b$  and  $t_{0,b}$ . The complete function to model the proper time distribution of the background is

$$\mathcal{P}_{bkg}(t) \propto \frac{[a_b(t - t_{0,b})]^{n_b}}{1 + [a_b(t - t_{0,b})]^{n_b}} \cdot \left\{ \frac{f_1^b}{\tau_1} \exp\left(-\frac{t}{\tau_1}\right) + \frac{1 - f_1^b}{\tau_2} \exp\left(-\frac{t}{\tau_2}\right) \right\} \otimes TG(t), \quad (8.1)$$

where  $f_1^b$  is the fraction of the first exponential and  $\tau_i$  the two lifetimes.

In the analysis of the channel  $B_s^0 \rightarrow J/\Psi\phi$  [14], a small contribution from prompt events to the proper time distribution of the selected  $B_s^0$  candidates is observed at very low proper times that cannot be described by  $\mathcal{P}_{bkg}(t)$ . These prompt events might originate from badly reconstructed vertices or come from a different proton - proton collision point that was very close to the determined primary vertex. One way to confirm the possibility that prompt  $J/\Psi$ 's contribute is to check if simulated prompt  $J/\Psi + \pi^+\pi^-$  decays pass the selection. In chapter 6.1, simulated prompt decays were used to determine the time resolution. This simulated inclusive sample contains events with prompt  $J/\Psi$ 's as well as  $J/\Psi$ 's from B decays. Figure 8.2 shows the proper time distribution of the simulated fake  $B_s^0$ 's that pass the selection including the cuts on the proper time. The black data refers to decays in which the  $J/\Psi$  is prompt and the red events are candidates in which the  $J/\Psi$  does not originate from the primary vertex but from the decay of a long-lived particle.

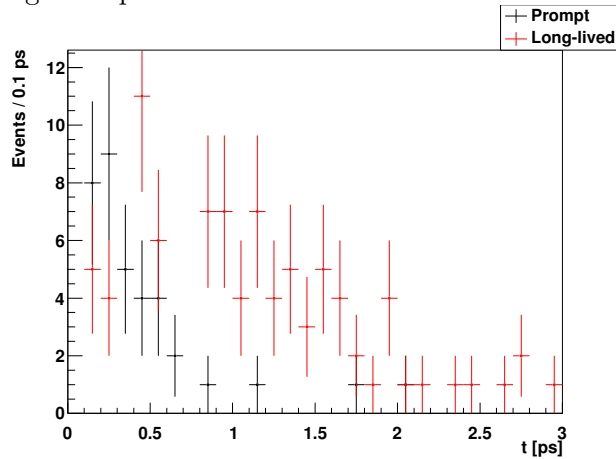


**Figure 8.2:** Proper time distribution of simulated prompt fake  $B_s^0$ 's (black) passing the analysis selection criteria. The data in red refers to  $B_s^0$  candidates where the  $J/\Psi$ 's are produced in the decay of a long-lived particle

35 B candidates using a prompt  $J/\Psi$  pass the selection criteria while in 84 decays, the  $J/\Psi$

originates from a long-lived particle. These absolute numbers do not represent the decays of an integrated luminosity of  $1.03 \text{ fb}^{-1}$  because the simulation is designed to study prompt decays but it shows that prompt  $J/\Psi$ 's can contribute to the selected events at small proper times.

The proper time distribution of prompt events is modeled by a single Gaussian with a mean around zero and one effective width  $\sigma_{pr}$  that is multiplied by an own time acceptance function with parameters  $a_{pr}$ ,  $n_{pr}$  and  $t_{0,pr}$ . The component of the combinatorics that can be described by  $\mathcal{P}_{bkg}(t)$  is called the long-lived component. Thus, the complete PDF to model the proper time distribution of background events is

$$\mathcal{P}(t) \propto \left\{ (1 - f_{pr}) \mathcal{P}_{bkg}(t) + f_{pr} \frac{[a_{pr}(t - t_{0,pr})]^{n_{pr}}}{1 + [a_{pr}(t - t_{0,pr})]^{n_{pr}}} \cdot \exp\left(-\frac{t^2}{2\sigma_{pr}^2}\right) \right\} \quad (8.2)$$

with  $\mathcal{P}_{bkg}(t)$  as above and  $f_{pr}$  is the fraction of prompt compared to the long-lived component. On the left of figure 8.3, this function is fitted to the proper time distribution of the upper sideband in the  $B_s^0$  mass distribution with the long-lived  $\mathcal{P}_{bkg}(t)$  in blue, the prompt component in green and the sum in red. On the right, only the long-lived PDF  $\mathcal{P}_{bkg}(t)$  is used for comparison. For both fits, the second lifetime  $\tau_2$  is fixed to a value of 2.5 ps to enable them to converge. The offsets  $t_0$  of both acceptances are fitted to the allowed limit of 0 ps and are therefore fixed to 0 ps.

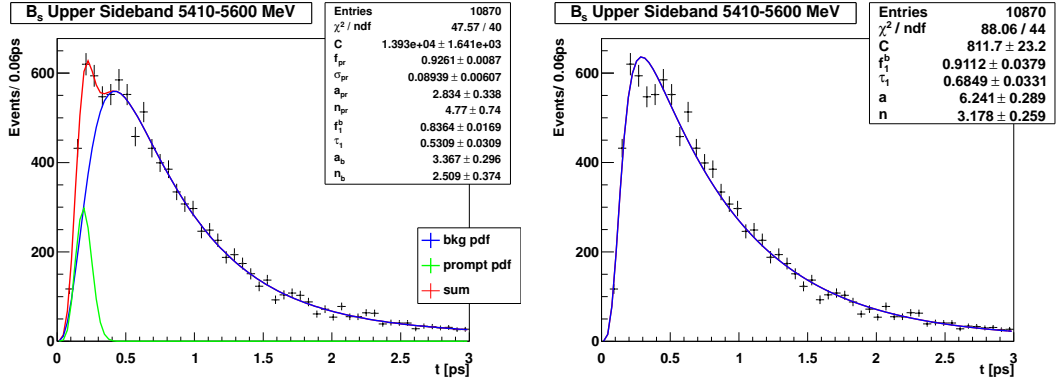


**Figure 8.3:** Prompt (green) and long-lived component (blue) (left) fitted to proper time distribution of the  $B_s^0$  upper sideband. On the right, it is attempted to model it only with the long-lived component (blue)  $\mathcal{P}_{bkg}(t)$  for comparison

On the right-hand side, it can be observed that the function  $\mathcal{P}_{bkg}(t)$  is insufficient to describe the data at low proper times while on the left, the data is described very well when the additional prompt PDF is included. However, the fit is very unstable and the numerous free parameters are highly correlated. Additionally, the result of this fit is dependent on the mass window that is selected. This is shown in figure 8.4 where the mass region of the upper sideband is divided into two sectors and described by the total PDF.

The prompt component appears to be more pronounced in the lower mass range from 5410 - 5500 MeV while the structure gets smeared out above 5500 MeV. The behaviour of the combinatorial background at low proper times cannot be exactly predicted in the peak region. To

## 8.2 Determination of the proper time shape of the background

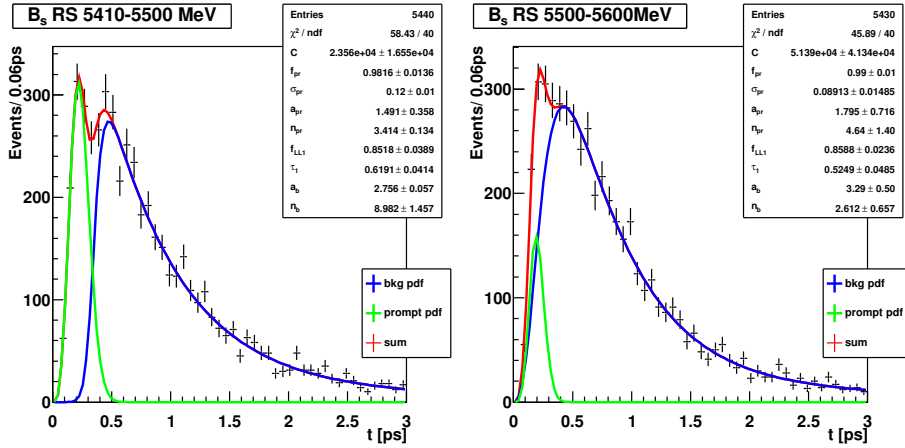


**Figure 8.4:** Prompt (green) and long-lived component (blue) fitted to the proper time distribution of the upper sideband in the  $B_s^0$  mass distribution in two mass regions

deal with this problem, a hard proper time cut at 0.3 ps removes the whole prompt component as it is applied in [14]. Furthermore, the number of signal events that are lost due to the proper time cut is small as it was shown in the mass fit in figure 5.12.

The proper time distribution of the upper mass sideband of the  $B_s^0$  signal region when enforcing the proper time cut can be described by the long-lived component  $\mathcal{P}_{bkg}(t)$  only which is shown in figure 8.5.

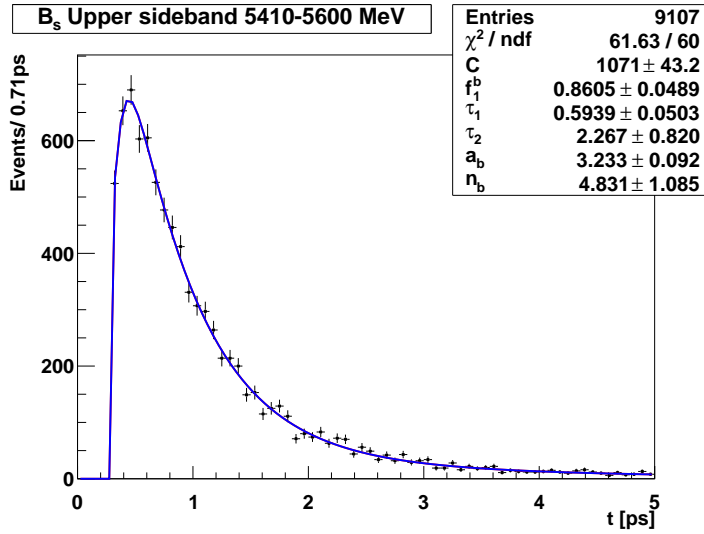


**Figure 8.5:** Proper time distribution of the upper sideband in the  $B_s^0$  mass distribution with proper time cut  $> 0.3$  ps described by the long-lived component  $\mathcal{P}_{bkg}(t)$  only

The fit is stable also without fixing  $\tau_2$  of the second long-lived component. The offset  $t_{0,b}$  is still fitted to be zero. The resulting values for the lifetimes and the acceptance parameter  $a_b$  are compatible with the results given in the fit without the proper time cut and including a prompt component. The acceptance parameter  $n_b$  with the value of  $4.83 \pm 1.085$  is higher

than the previous value of  $2.51 \pm 0.37$  but the fit without a prompt component and with a reduced number of free variables is preferred. The acceptance parameters  $a_b = 3.23 \pm 0.09$ ,  $n_b = 4.83 \pm 1.09$  and  $t_{0,b} = 0$  ps will be fixed in the determination of  $\phi_s$  and the decay parameters  $f_1^b = 0.86 \pm 0.05$ ,  $\tau_1 = 0.59 \pm 0.05$  ps and  $\tau_2 = 2.27 \pm 0.82$  will be floating but constrained within their measured Gaussian uncertainties.<sup>1</sup> Variations of the background time acceptance parameters will be studied as a systematic uncertainty.

---

<sup>1</sup> The method to constrain a parameter within its Gaussian uncertainty will be explained in [chapter 10](#)

## 9 Determination of the initial $B_s^0$ production flavour

### flavour

Without the knowledge of the initial flavour state of the B-meson, it is impossible to resolve the  $B_s^0$ - $\bar{B}_s^0$  time oscillation in time and to perform a CP analysis. The determination of the initial  $B_s^0$  production flavour is called *Flavour Tagging*. There are two different methods for tagging that are sketched in figure 9.1.

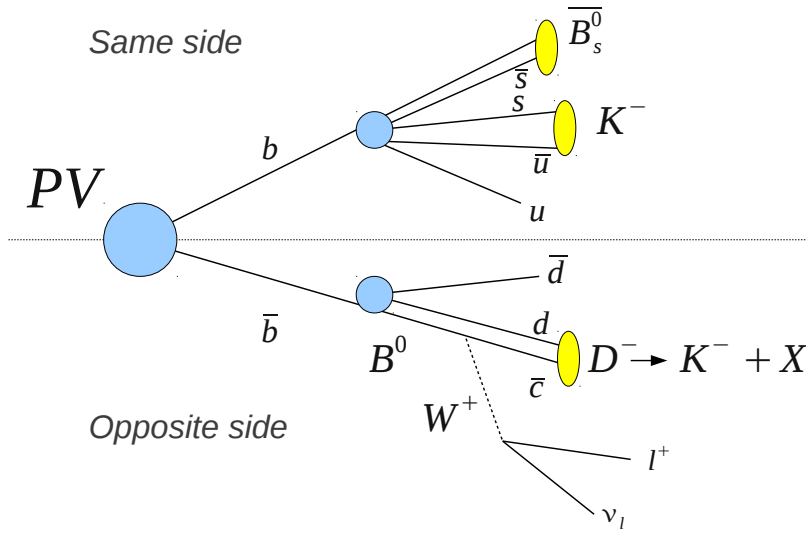


**Figure 9.1:** Illustration of the flavour tagging algorithms. In the upper part the same side tagger and below the opposite side tagger

- The *opposite side* tagging algorithm sketched in the lower part of figure 9.1 profits from the fact that in proton-proton collisions, the b-quarks are produced as a quark–anti-quark pair. While one of them hadronizes to become the signal  $\bar{B}_s^0$ , the other quark hadronizes to a B-hadron with opposite flavour that can decay semileptonically into a D-meson, a lepton  $l$  and a neutrino  $\nu_l$ . The flavour of the b-quark is then determined by the charge of the lepton  $l$ . Additionally, when the charmed meson decays into a Kaon, the Kaon charge can also be used to confirm the flavour. The combined tagging decision forms the *opposite side tag*.
- The *same side* tagging algorithm is sketched in the upper part. The s anti-quark that is used in the hadronization of the b-quark to form the signal  $\bar{B}_s^0$ , is produced together

with an s-quark. The s-quark hadronizes and can form a K-meson that is close to the signal  $\bar{B}_s^0$ . The charge of the Kaon can be used to determine the flavour of the initial b-quark. This algorithm is called the *same side Kaon tagger* or shortly the same side tagger. If the signal B-meson is a  $B^0$ , the same side tagger uses pions that are created in the vicinity.

The flavour tag decision  $q$  provided by the taggers is defined as  $q = 1$  for a tagged  $B_s^0$ ,  $q = -1$  for a  $\bar{B}_s^0$  and  $q = 0$  for an unsuccessful tag. Since the algorithms are not perfect, the mistag probability  $\omega_{tag}$  gives the probability that the algorithm has assigned the wrong tag decision where an  $\omega_{tag}$  of 0.5 already means that the decision is completely random. The dilution that dilutes the  $B_s^0$ - $\bar{B}_s^0$  oscillation is defined as  $D_{tag} = (1 - 2\omega_{tag})$ . For every event, the mistag probability is estimated by the tagging algorithms based on the occurring kinematics and is denoted as  $\omega_{est}$ . Furthermore, the taggers are not always able to provide a tag decision. The tagging efficiency  $\epsilon_{tag}$  therefore indicates the ratio of events for which the tagging algorithms are able to deliver a tagging decision:

$$\epsilon_{tag} = \frac{\text{number of tagged events}}{\text{number of all events}} = \frac{N_{tagged}}{N}. \quad (9.1)$$

The effective tagging power  $\mathcal{P}_{tag}^{eff} = \epsilon_{tag} D_{tag}^2$  is the measure for the statistical power of the events if tagging is considered. Considering a per event determination of the mistag probabilities, it is computed as

$$\mathcal{P}_{tag}^{eff} = \epsilon_{tag} \langle D_{tag}^2 \rangle = \frac{N_{tagged}}{N} \frac{1}{N_{tagged}} \sum_{i=1}^{N_{tagged}} (1 - 2\omega_{i,est})^2 = \frac{1}{N} \sum_{i=1}^{N_{tagged}} (1 - 2\omega_{i,est})^2. \quad (9.2)$$

## 9.1 Calibration of the $B_s^0$ production flavour determination

Since the mistag probability  $\omega_{est}$  provided by the tagging algorithms is just an estimate, its quality has to be evaluated by testing it on decays where the true flavor is known. For the opposite side tagger, this calibration is done with  $B^+ \rightarrow J/\Psi K^+$  decays in [34] where the b-flavour is determined by the charge of the Kaon. The same side Kaon tagger is calibrated with the channel  $B_s^0 \rightarrow D_s^\pm \pi^\mp$  in [35] where the pion charge determines the flavour of the final state  $D_s^\mp \pi^\pm$ . Here, the  $B_s^0$  can oscillate which makes a time dependent calibration procedure necessary. The dependence of the true  $\omega_{tag}$  of the measured mistag probability  $\omega_{est}$  is described by a linear function with the offset  $p_0$  and the slope  $p_1$ :

$$\omega_{tag} = p_0 + p_1 \cdot (\omega_{est} - \eta), \quad (9.3)$$

where  $\eta = \langle \omega_{est} \rangle$  is the average estimated mistag probability. If  $\omega_{tag}$  and  $\omega_{est}$  are close to each other,  $p_0$  takes a similar value as  $\eta$  and  $p_1$  is close to 1. The determined parameters  $p_0$ ,  $p_1$  and  $\eta$  are given in table 10.3. They are used to correct the estimated event-dependent values  $\omega_{est}$ .

	$p_0$	$p_1$	$\eta$
opposite side	0.392	1.035	0.391
same side	0.35	0.51	0.324

**Table 9.1:** Tagging calibration parameters of opposite and same side tagger taken from [34] and [35] in 2011 data

opposite side tagging efficiency $\epsilon_{tag}$	$33.2 \pm 0.09$ %
opposite side average $\omega_{tag}$	$36.7 \pm 0.2$ %
opposite side tagging power $\mathcal{P}_{tag}^{eff}$	$2.35 \pm 0.06$ %
same side tagging efficiency $\epsilon_{tag}$	$15.8 \pm 0.3$ %
same side tagging average $\omega_{tag}$	$33.2 \pm 2.2$ %
same side tagging power $\mathcal{P}_{tag}^{eff}$	$1.6 \pm 0.3$ %

**Table 9.2:** Tagging performance of the calibration samples  $B^+ \rightarrow J/\Psi K^+$  (opposite side) in [34] and  $B_s^0 \rightarrow D_s^\pm \pi^\mp$  (same side) in [35] in 2011 data

The tagging performance determined with the calibration samples  $B^+ \rightarrow J/\Psi K^+$  in [34] and  $B_s^0 \rightarrow D_s^\pm \pi^\mp$  in [35] in 2011 data are listed in table 9.2.

If there is a tagging decision from both the opposite and the same side tagger, the two values are combined by reweighting them according to their mistag probabilities described in [36].<sup>1</sup> The combined mistag probability is denoted as  $\omega_{ovl}$  where the index ovl stands for overlapping tagging decisions. How tagging is implemented in the fitting procedure will be described in the next chapter.

<sup>1</sup> The calibrated wrong-tag probability from the opposite side tagger is denoted as  $\omega_{os}$  and the calibrated value from the same side tagger as  $\omega_{ss}$ . If the decisions are the same, the combined mistag probability  $\omega_{ovl}$  is computed as follows:

$$\omega_{ovl} = \left( 1 - \frac{1 - \omega_{ss} - \omega_{os} + \omega_{ss}\omega_{os}}{1 - \omega_{os} - \omega_{ss} - 2\omega_{ss}\omega_{os}} \right), \quad (9.4)$$

where  $\omega_{ovl}$  stands for the combined mistag probability for overlapping tagging decisions. When the two decisions are different, the tag with the smaller mistag probability  $\omega_{<}$  is chosen and the combined  $\omega_{ovl}$  is calculated as

$$\omega_{ovl} = \left( 1 - \frac{\omega_{>}(1 - \omega_{<})}{\omega_{>}(1 - \omega_{<}) + \omega_{<}(1 - \omega_{>})} \right), \quad (9.5)$$

where  $\omega_{>}$  is the larger mistag probability of the two.

## 10 Determination of the phase $\phi_s$

The phase  $\phi_s$  is determined from a 2-dimensional fit of the mass and proper time distribution of the selected  $B_s^0$  candidates using an unbinned maximum likelihood fit.

### 10.1 Maximum Likelihood Fit

A probability density function (PDF)  $\mathcal{P}(\vec{x}; \vec{a})$  describes the probability to measure certain variables  $\vec{x}$  with given parameters  $\vec{a}$ .  $\mathcal{P}(\vec{x}; \vec{a})$  is positive and the integral over the whole variable space  $\int \mathcal{P}(\vec{x}; \vec{a}) d\vec{x} = 1$  since the probability to measure anything is one. However,  $\mathcal{P}(\vec{x}; \vec{a})$  does not give the probability for a parameter set  $\vec{a}$  given a measurement  $\vec{x}$ , but the probability to measure  $\vec{x}$  given a parameter set  $\vec{a}$ , i.e.  $\mathcal{P}(\vec{x}; \vec{a}) = \mathcal{P}(\vec{x}|\vec{a})$ .

The likelihood function  $\mathcal{L}$  is defined by the product of the single event probabilities of all events  $e$ :

$$\mathcal{L} = \prod_{e=1}^{N_{events}} \mathcal{P}(\vec{x}_e, \vec{a}), \quad (10.1)$$

where  $N_{events}$  is the total number of events. The best estimation of the parameter set  $\vec{a}$  is obtained by maximizing the likelihood  $\mathcal{L}$  to observe the given data set  $\vec{x}$ . Taking the negative logarithm of the likelihood function  $\mathcal{L}$  facilitates the procedure and turns it into a minimization problem:

$$- \ln \mathcal{L} = - \sum_{e=1}^{N_{events}} \ln \mathcal{P}(\vec{x}_e; \vec{a}). \quad (10.2)$$

In this analysis, the measured variables are the reconstructed  $B_s^0$  candidate mass  $m$ , the proper time  $t$  and the flavour tag  $q$ . Furthermore, it is assumed that the total PDF  $\mathcal{P}(m, t, q; \vec{a})$  can be split up in a signal and a background component:

$$\mathcal{P}(m, t, q; \vec{a}) = f_{sig} \mathcal{P}_{sig}(m, t, q; \vec{a}) + (1 - f_{sig}) \mathcal{P}_{bkg}(m, t; \vec{a}), \quad (10.3)$$

where  $f_{sig}$  refers to the signal fraction compared to the background fraction  $(1 - f_{sig})$ . Each component factorizes in a mass  $\mathcal{P}_{sig/bkg}(m; \vec{a})$  and a proper time-dependent part  $\mathcal{P}_{sig/bkg}(t, (q); \vec{a})$ :  $\mathcal{P}_{sig/bkg}(m, t, q; \vec{a}) = \mathcal{P}_{sig/bkg}(m; \vec{a}) \mathcal{P}_{sig/bkg}(t, (q); \vec{a})$  and the complete PDF is

$$\begin{aligned} \mathcal{P}(m, t, q; \vec{a}) &= f_{sig} \mathcal{P}_{sig}(m; \vec{a}) \mathcal{P}_{sig}(t, q; \vec{a}) \\ &+ (1 - f_{sig}) \mathcal{P}_{bkg}(m; \vec{a}) \mathcal{P}_{bkg}(t; \vec{a}). \end{aligned} \quad (10.4)$$

According to their physical meaning, the involved parameters can be classified into three different groups. The parameters  $\vec{a}_{phys}$  parameterise the physics that is expected from theory

for a pure signal sample in a perfect measurement. The parameters  $\vec{a}_{det}$  that have been determined in the previous chapters are needed to describe detector and acceptance effects in the real measurement. The background parameters  $\vec{a}_{bkg}$  parameterise the background PDF to model the background behaviour. The detector and background parameters can be further divided into parameters that are incorporated into the mass-, time- and flavour-dependent PDFs. Thus,

$$\begin{aligned} \mathcal{P}(m, t, q; \vec{a}) &= f_{sig} \mathcal{P}_{sig}(m; \vec{a}_{phys}, \vec{a}_{det;m}) \mathcal{P}_{sig}(t, q; \vec{a}_{phys}, \vec{a}_{det;t,q}) \\ &+ (1 - f_{sig}) \mathcal{P}_{bkg}(m; \vec{a}_{bkg;m}, \vec{a}_{det;m}) \mathcal{P}_{bkg}(t; \vec{a}_{bkg,t}, \vec{a}_{det;t}). \end{aligned} \quad (10.5)$$

### Gaussian constraints

A few parameters of the parameter set  $\vec{a}$  have been determined independently and there is no reason to also determine these parameters. As these parameters have uncertainties, it is not desirable to fix them to constant values but to constrain them to their measured values in the experimental uncertainties. This is done by adding an additional term to the negative logarithmic likelihood function  $\mathcal{L}$ :

$$- \ln \mathcal{L} = - \sum_{e=1}^{N_{events}} \left\{ \ln \mathcal{P}(m_e, t_e, q_e; \vec{a}) + \sum_{i=1}^{N_{constraints}} \frac{(a_i - a_{i,meas})^2}{2\sigma_{i,meas}^2} \right\}, \quad (10.6)$$

where  $N_{constraints}$  is the number of constrained parameters,  $a_{i,meas}$  is the measured value of the  $i$ 'th parameter and  $\sigma_{i,meas}$  its experimental uncertainty. In this way, these parameters  $a_i$  are still included in the fitted parameter set  $\vec{a}$ . The negative logarithmic likelihood increases quadratically with an increasing deviation from  $a_{i,meas}$ , which prevents it from drifting away.

In the following sections the involved pdfs and their parameters are introduced in detail.

## 10.2 Signal description

### 10.2.1 Mass description

The signal PDF for the mass distribution is the sum of two Gaussian functions as it was introduced in section 5.5 in equation 5.2 to describe the  $B_s^0$  mass peak:

$$\begin{aligned} \mathcal{P}_{sig}(m; m_{B_s^0}, f_1^m, \sigma_1, \sigma_2) &= \left\{ \frac{f_1^m}{\sqrt{2\pi}\sigma_{m,1}} \exp\left(-\frac{(m - m_{B_s^0})^2}{2\sigma_{m,1}^2}\right) \right. \\ &\quad \left. + \frac{1 - f_1^m}{\sqrt{2\pi}\sigma_{m,2}} \exp\left(-\frac{(m - m_{B_s^0})^2}{2\sigma_{m,2}^2}\right) \right\}. \end{aligned}$$

The only physics parameter, the mass  $m_{B_s^0}$  is the mean of the Gaussian,  $f_1^m$  is the fraction of the first Gaussian and the two widths  $\sigma_i$  are describing the mass resolution of the detector. The parameters  $m_{B_s^0}$ ,  $f_1^m$  and  $\sigma_1$  are free and determined in the fit. The ratio  $\frac{\sigma_1}{\sigma_2}$  is fixed to a value computed in a 1-dimensional mass fit where the dependence of the proper time is neglected. This is done because the resolution parameters are strongly correlated.

### 10.2.2 Proper time dependence

When neglecting any detector effects, the PDF describing the proper time distribution of the signal is given by the theoretical expression of equation 10.7. It consists of an exponential decay function modulated by a time-dependent function which depends on  $\Delta\Gamma_s$ ,  $\Delta m_s$  and  $\phi_s$ :

$$\mathcal{P}_{sig}(t, q) \propto e^{-\Gamma_s t} \left\{ \cosh \frac{\Delta\Gamma_s t}{2} + \cos \phi_s \sinh \frac{\Delta\Gamma_s t}{2} - q \sin \phi_s \sin(\Delta m_s t) \right\}. \quad (10.7)$$

However, for the CP eigenstate  $J/\Psi\pi^+\pi^-$ , the parameters  $\Gamma_s$  and  $\Delta\Gamma_s$  cannot be determined simultaneously. Instead, the covariance matrix of  $\Gamma_s$  and  $\Delta\Gamma_s$  determined in the measurement using  $B_s^0 \rightarrow J/\Psi\phi$  decays [14] is used to constrain them:

	$\Gamma_s$	$\Delta\Gamma_s$
$\Gamma_s$	$0.0054^2$	$-0.38 \cdot (0.0054 \cdot 0.018)$
$\Delta\Gamma_s$	$-0.38 \cdot (0.0054 \cdot 0.018)$	$0.018^2$

**Table 10.1:** Covariance matrix of  $\Gamma_s$  and  $\Delta\Gamma_s$  measured in the channel  $B_s^0 \rightarrow J/\Psi\phi$  [14]

This is equivalent to a 2-dimensional Gaussian constraint of  $\Gamma_s = 0.658 \pm 0.0054 \text{ ps}^{-1}$  and  $\Delta\Gamma_s = 0.116 \pm 0.018 \text{ ps}^{-1}$  [14]. A Gaussian constraint is also applied for  $\Delta m_s = 17.63 \pm 0.11$  measured in  $B_s^0 \rightarrow D_s^-(3)\pi$  decays in [15].

The wrong-tag probability  $\omega_{tag}$  of the tagging algorithms has to be accounted for and leads to a dilution of the oscillation amplitude by the factor  $D = 1 - 2\omega_{tag}$ :

$$\mathcal{P}_{sig}(t, q, \omega_{tag}) \propto e^{-\Gamma_s t} \left\{ \cosh \frac{\Delta\Gamma_s t}{2} + \cos \phi_s \sinh \frac{\Delta\Gamma_s t}{2} - q D \sin \phi_s \sin(\Delta m_s t) \right\}. \quad (10.8)$$

Due to the uncertainties of the calibration of the tagging algorithms, the calibrated mistag probabilities  $\omega_{tag}$  are not fixed in the fit but constrained to their calibrated values within the measured uncertainties. Thus, the uncertainty of the calibration does not have to be treated as a systematic uncertainty for  $\phi_s$  but is included in the statistical uncertainty of the fit result. Variations of  $\omega_{tag}$  according to the same linear dependence as in the calibration procedure are allowed:

$$\omega_{tag}^{fit} = p_0^{fit} + p_1^{fit} \cdot (\omega_{tag} - \eta_{tag}), \quad (10.9)$$

where  $\omega_{tag}^{fit}$  is the fitted mistag probability and  $\eta_{tag}$  is the average calibrated mistag probability. The parameters  $p_0^{fit}$  and  $p_1^{fit}$  are chosen such that  $\omega_{tag}^{fit}$  is equal to  $\omega_{tag}$ . The uncertainties of  $p_0^{fit}$  and  $p_1^{fit}$  reflect the uncertainty of the calibration procedure. In the fit, Gaussian constraints are applied for the floating parameters  $p_0^{fit}$  and  $p_1^{fit}$ . The values and their uncertainties are taken from [34] and [35] and listed in table 10.2.

For the wrong-tag probability of overlapping tagging decisions,  $p_1^{fit}$  is fixed to one and  $\eta_{tag}$  is fixed to zero because the statistics is too low for two floating parameters. A possible deviation

	$p_0^{fit}$	$p_1^{fit}$	$\eta_{tag}$
opposite side	$0.392 \pm 0.008$	$1.0 \pm 0.023$	0.391
same side	$0.35 \pm 0.017$	$1.0 \pm 0.016$	0.35
overlap	$0.0 \pm 0.025$	1.0	0.0

**Table 10.2:** Tagging calibration parameters  $p_0^{fit}$  and  $p_1^{fit}$  in the fit taken from [34] and [35]

of the tagging performance for  $B_s^0$ - and  $\bar{B}_s^0$ -mesons is taken into account by an additional parameter  $\delta$ :

$$\omega_{tag,B/\bar{B}}^{fit} = p_0^{fit} + p_1^{fit} \cdot (\omega_{tag} - \eta_{tag}) \pm \frac{\delta}{2}. \quad (10.10)$$

The tagging parameter  $\delta$  is constrained to its determined value in the measured uncertainty. The values are provided from private communication with G. Krocker, a member of the LHCb tagging group and are given in table 10.3.

	$\delta$
opposite side	$0.011 \pm 0.0034$
same side	$-0.019 \pm 0.005$
overlap	$-0.011 \pm 0.004$

**Table 10.3:** Additional tagging parameters  $\delta$  to account for possible differences in the tagging performances for  $B_s^0$ - and  $\bar{B}_s^0$ -mesons provided from private communication with G. Krocker

## 10.3 Background description

### 10.3.1 Mass description

The mass distribution of the background component is described by an exponential decay function with the constant  $\alpha$ :

$$\mathcal{P}_{bkg}(m; \alpha) \propto e^{-\alpha m}. \quad (10.11)$$

In the studies of the  $B_s^0$  background components in chapter 5.5, it has been confirmed that the upper mass sideband of the  $B_s^0$  signal region is well described by this function and  $\alpha$  will be floating in the fit.

### 10.3.2 Proper time dependence

The time behaviour of the proper time distribution of the background is modeled by the sum of two exponential decay functions

$$\mathcal{P}_{bkg}(t; f_1^b, \tau_1, \tau_2) = \frac{f_1^b}{\tau_1} \exp\left(-\frac{t}{\tau_1}\right) + \frac{1-f_1^b}{\tau_2} \exp\left(-\frac{t}{\tau_2}\right), \quad (10.12)$$

where  $f_1^b$  is the fraction of the first exponential and  $\tau_i$  the lifetimes. It has been validated that it describes the proper time distribution of the upper sideband in the  $B_s^0$  mass distribution. It is assumed that the background in the signal region exhibits the same structure. Gaussian constraints are applied for the floating parameters.

## 10.4 Proper time resolution

The resolution model that is applied in this analysis is the model with a triple Gaussian  $TG_{ev}(t, \sigma_{ct})$  using the per event time resolution defined in equation 6.6. It is applied by convoluting the triple Gaussian with the time-dependent signal and background PDFs:

$$\begin{aligned} \mathcal{P}_{sig}(t, q) &\rightarrow \mathcal{P}_{sig}(t, q) \otimes TG_{ev}(t, \sigma_{ct}) \\ \mathcal{P}_{bkg}(t; f_1^b, \tau_1, \tau_2) &\rightarrow \mathcal{P}_{bkg}(t; f_1^b, \tau_1, \tau_2) \otimes TG_{ev}(t, \sigma_{ct}) \end{aligned} \quad (10.13)$$

The resolution is assumed to be the same for signal and background. The resolution parameters  $(f_1, f_2, s_1, s_2, s_3)$  are fixed in the fit.

## 10.5 Proper time acceptance

The time acceptance is modeled by the acceptance function  $\epsilon_{time}(t)$  of equation 7.3. It is applied by multiplying the time-dependent signal and background PDFs by the acceptance function  $\epsilon_{time}(t)$ :

$$\begin{aligned} \mathcal{P}_{sig}(t, q) &\rightarrow \epsilon_{time}(t; a_{sig}, n_{sig}, t_{0,sig}) \cdot \mathcal{P}_{sig}(t, q) \\ \mathcal{P}_{bkg}(t; f_1^b, \tau_1, \tau_2) &\rightarrow \epsilon_{time}(t; a_{bkg}, n_{bkg}, t_{0,bkg}) \cdot \mathcal{P}_{bkg}(t; f_1^b, \tau_1, \tau_2) \end{aligned} \quad (10.14)$$

The determined acceptance parameters are fixed in the fit but the uncertainties in their determination will be treated as a systematic uncertainty.

## 10.6 Correct treatment of the per event uncertainties $\omega_{tag}$ and $\sigma_{ct}$

The uncertainties  $\omega_{tag}$  and  $\sigma_{ct}$  are evaluated for every particular event and can be different for the signal and the background components. Although they are observables, the PDFs that were computed in the previous sections depend on their measured distributions, i.e. the PDFs must be correctly denoted as  $\mathcal{P}(m, q, t | \omega_{tag}, \sigma_{ct}; \vec{a})$  [11]. The simple conditional probability law  $P(A \cup B) = P(A|B) P(B)$  gives

$$\mathcal{P}(\vec{x}, \omega_{tag}, \sigma_{ct} | \vec{a}) = \mathcal{P}(\vec{x} | \omega_{tag}, \sigma_{ct}, \vec{a}) \mathcal{P}(\omega_{tag}) \mathcal{P}(\sigma_{ct}). \quad (10.15)$$

Hence, for a correct treatment of the per event variables  $\omega_{tag}$  and  $\sigma_{ct}$ , the signal and the background PDFs have to be multiplied with the probability distributions of  $\omega_{tag}$  and  $\sigma_{ct}$  to ensure the correct weights and normalisations of the two components [11]:

$$\mathcal{P}(m, t, q; \vec{a}) = f_{sig} \mathcal{P}_{sig}(m, t, q | \omega_{tag}, \sigma_{ct}, \vec{a}) \mathcal{P}_{sig}(\omega_{tag}) \mathcal{P}_{sig}(\sigma_{ct}) + (1 - f_{sig}) \mathcal{P}_{bkg}(m, q, t | \omega_{tag}, \sigma_{ct}, \vec{a}) \mathcal{P}_{bkg}(\omega_{tag}) \mathcal{P}_{bkg}(\sigma_{ct}). \quad (10.16)$$

In the maximization process of the likelihood function  $\mathcal{L}$ , the distribution  $\mathcal{P}(\omega_{tag})$  and  $\mathcal{P}(\sigma_{ct})$  can be factored out if they are the same for signal and background. Since this is not the case, they have to be considered.

The distributions of  $\omega_{tag}$  have to be computed for the opposite, the same side tagger and for both opposite and same side tagged events. Exemplary, figure 10.1 shows the distribution of the opposite side tagging dilution (left) and the estimated proper time error  $\sigma_{ct}$  (right) for the selected events. The wrong sign events in red model the background distribution and are subtracted from the right sign events to model the signal component in black.

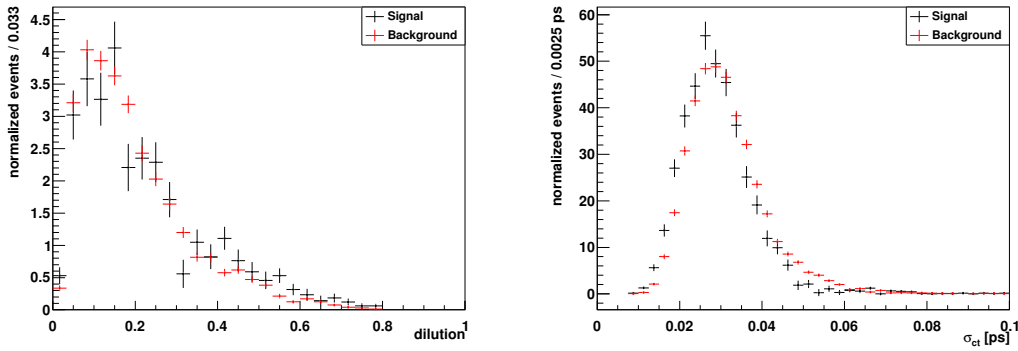


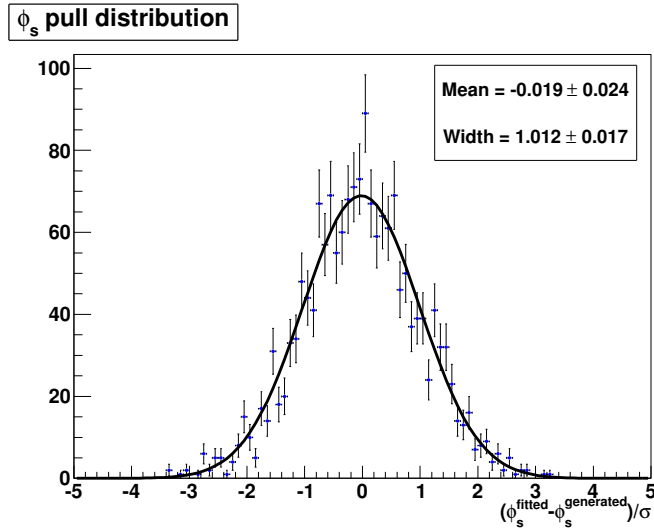
**Figure 10.1:** Distributions of estimated dilution of opposite side tagger (left) and estimated proper time error  $\sigma_{ct}$  (right) of the selected  $B_s^0 \rightarrow J/\Psi \pi^+ \pi^-$  decays

## 10.7 Validation of the fitting procedure

Before starting to fit the data with the constructed maximum likelihood fit, the fitting procedure has to be validated, in particular the handling of the errors and the likelihood normalisations. This is done with so-called *Toy Studies*. Toy Studies are pseudo experiments in which a number of events is generated according to the PDFs that are described above with parameters that can be chosen arbitrary. Since there will be only a limited number of 21551 selected  $B_s^0 \rightarrow J/\Psi \pi^+ \pi^-$  events in the fit, each toy experiment is also generated with 21551 events that are then subject to statistical fluctuations. By repeating toy experiments 1750 times the fluctuations can be estimated and the measured parameters can be compared with those used to generate the events. Since this analysis is not sensitive to  $\Gamma_s$  and  $\Delta\Gamma_s$  simultaneously,  $\Delta\Gamma_s$  is fixed in the toys while  $\Gamma_s$  can float. The values that are used in the generation of the toys are  $\phi_s = -0.02$ ,  $\Gamma_s = 0.656 \text{ ps}^{-1}$  and  $\Delta\Gamma_s = 0.123 \text{ ps}^{-1}$ , the others are taken as described above. Except for  $\Delta m_s$ , all Gaussian constraints are removed. Since the resolution

has to be computed for every event in the per event time resolution model, the fit procedure consumes a lot of CPU time. Therefore, the average resolution model is applied for the toy experiments. The tagging parameter  $\delta$  has to be fixed in the toy experiments because the normalisation of the PDF has to be recalculated for every event when  $\delta$  can float which is also very CPU time consuming. The key quantity to describe the quality of the fit algorithm is the *pull* distribution of a given parameter  $a$ . When the fitting algorithm works correctly, the pull exhibits a symmetric distribution around zero with a width of 1. The average uncertainty of the fitted values for  $\phi_s$  can be used as a first estimation of the expected statistical uncertainty of  $\phi_s$ .

The results of 1750 fits, each generated with 21551 events, are shown in the following. Figure 10.2 shows the pull distribution of  $\phi_s$  that is distributed around the mean  $-0.019 \pm 0.024$  with a width of  $1.012 \pm 0.017$  as it is expected. This proves that the errors and likelihood normalisations are correctly treated in the fitting procedure.



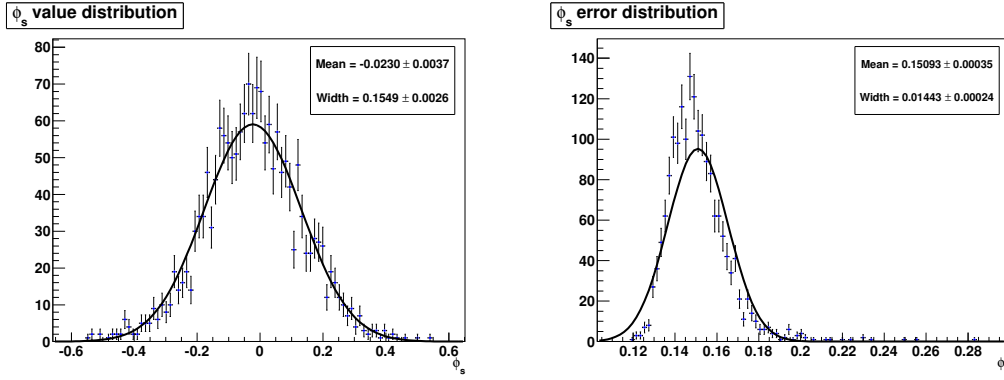
**Figure 10.2:**  $\phi_s$  pull distribution of 1750 toy studies with input value  $\phi_s = -0.02$  with 21551 events

Figure 10.3 shows the fitted values (left) and the determined errors (right) for  $\phi_s$ .

It can be seen that the error distribution of  $\phi_s$  expected from the toy studies for a statistics of 21551 events lies within 0.12 and 0.19 with an average uncertainty of 0.151.

Since  $\Delta m$  is constrained with Gaussian errors, its pull distribution is not meaningful, instead figure 10.4 shows the value and pull distribution of  $\Gamma_s$ .

The  $\Gamma_s$  pull distribution with its mean of  $-0.022 \pm 0.024$  is still compatible with zero while the width of  $1.003 \pm 0.017$  is almost exactly 1. Thus, the fitting procedure works correctly and can be applied to finally fit for  $\phi_s$  on the selected  $B_s^0 \rightarrow J/\Psi \pi^+ \pi^-$  decays.



**Figure 10.3:** Fitted values for  $\phi_s$  (left) and uncertainties (right) of 1750 toy studies with input value  $\phi_s = -0.02$  with 21551 events

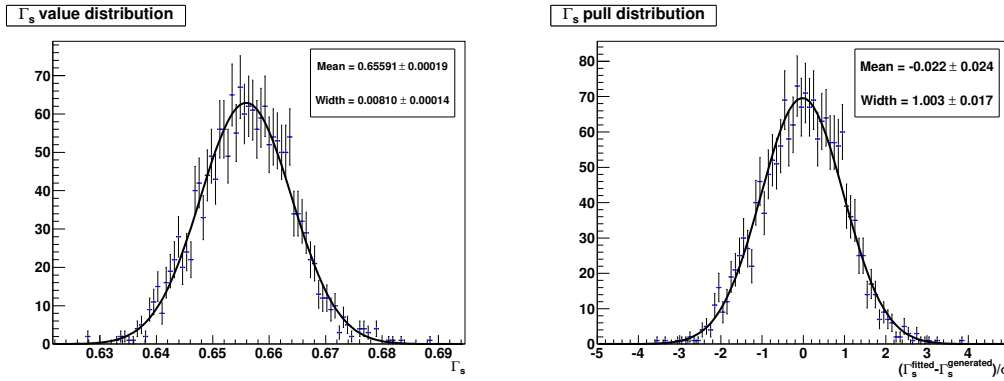


**Figure 10.4:** Fitted values (left) for  $\Gamma_s$  and the pull distributions for  $\Gamma_s$  (right) of 1750 toy studies with input value  $\Gamma_s = 0.656$ . with 21551 events

## 10.8 Results

The fit model of the previous sections is applied on data to determine the value of  $\phi_s$ . In total, a number of 21551 selected  $B_s^0$  candidates in the mass range from 5320 - 5600 MeV are subject to this fit. Since the parameters of the signal mass PDF  $\mathcal{P}(m; f_1^m, \sigma_1, \sigma_2)$  are highly correlated, the ratio of  $\frac{\sigma_1}{\sigma_2}$  is fixed in the fit. This ratio is determined in a separate fit beforehand in which the mass  $m$  is the only measured variable and only the mass PDFs for signal and background are applied in the likelihood function. The results of this fit can be seen in table 10.4. The invariant mass distribution and the fitted mass PDF are shown in figure 10.5.

The data is very well described by the PDFs in the full mass region. The fit yields a total number of  $7090 \pm 140$   $B_s^0$  signal events and the value for  $\sigma_1/\sigma_2$  is  $1.71 \pm 0.14$ .

In the next step, the 2-dimensional fit to the mass and proper time distributions is performed. The final fit results are presented in table 10.5. The mass and proper time distributions of the selected  $B_s^0$  candidates with the 1-dimensional projections of the 2-dimensional fit are shown in figure 10.6. The fit yields  $7148 \pm 97$   $B_s^0$  signal candidates. For the CP-violating phase  $\phi_s$ , a value of  $-0.074 \pm 0.177$  rad is obtained. The statistical uncertainty is slightly higher than the average uncertainty of 0.151 expected from the toy studies but it is still within the

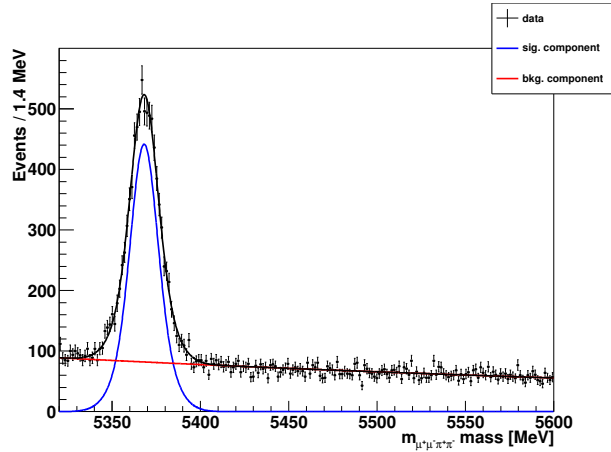


**Figure 10.5:** Invariant mass distribution of the  $B_s^0$  candidates described by mass PDFs only

parameter	value
$f_{sig}$	$0.3290 \pm 0.0065$
$m_{B_s^0}$	$5368.14 \pm 0.15 \text{ MeV}$
$f_1^m$	$0.52 \pm 0.23$
$\sigma_1$	$7.06 \pm 0.91 \text{ MeV}$
$\frac{\sigma_1}{\sigma_2}$	$1.71 \pm 0.14$
$\alpha$	$0.00168 \pm 0.00015 \text{ MeV}^{-1}$

**Table 10.4:** Fit results of the fit of the mass PDF to the mass distribution of the selected  $B_s^0 \rightarrow J/\Psi\pi^+\pi^-$  to determine  $\sigma_1/\sigma_2$

expected error distribution. Due to the application of the average resolution model in the toy experiments and the smaller number of floating parameters<sup>1</sup>, the observed uncertainty on data can be slightly higher.

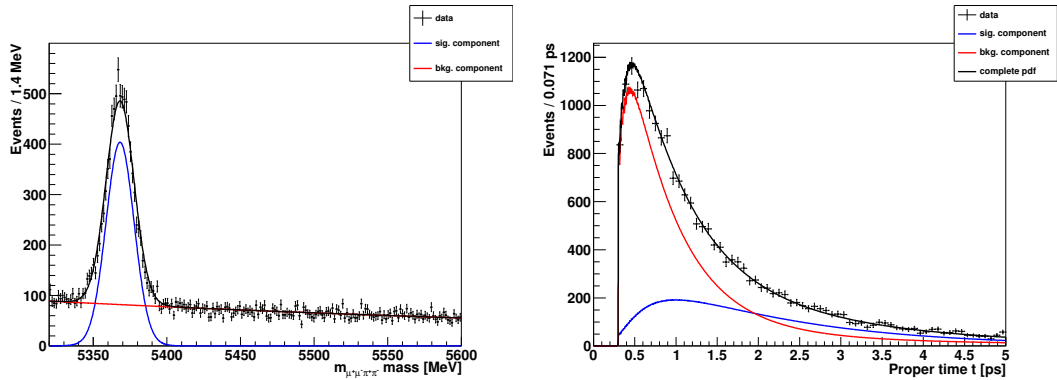


**Figure 10.6:** Invariant mass distribution(left) and proper time distribution(right) of the selected  $B_s^0$  candidates with the 1-dimensional projections of the 2-dimensional fit

<sup>1</sup>  $\Delta\Gamma_s$  and  $\delta$  have to be fixed in the toy experiments

parameter	value
$\phi_s$	$-0.074 \pm 0.177$ rad
$\Gamma_s$	$0.6627 \pm 0.0043$ $ps^{-1}$
$\Delta\Gamma_s$	$0.097 \pm 0.012$ $ps^{-1}$
$\Delta m_s$	$17.65 \pm 0.13$ $ps^{-1}$
$f_{sig}$	$0.3317 \pm 0.0045$
$m_{B_s^0}$	$5368.16 \pm 0.15$ $MeV$
$f_1^m$	$0.957 \pm 0.024$
$\sigma_{m,1}$	$9.48 \pm 0.16$ $MeV$
$\alpha$	$0.00163 \pm 0.00012$ $MeV^{-1}$
$f_1^b$	$0.800 \pm 0.013$
$\tau_1$	$0.590 \pm 0.012$ $ps$
$\tau_2$	$2.67 \pm 0.12$ $ps$
$p_0^{fit}(os)$	$0.392 \pm 0.008$
$p_1^{fit}(os)$	$1.000 \pm 0.023$
$p_0^{fit}(ss)$	$0.350 \pm 0.017$
$p_1^{fit}(ss)$	$1.00 \pm 0.16$
$p_0^{fit}(ovl)$	$0.000 \pm 0.025$
$\delta_{os}$	$0.011 \pm 0.003$
$\delta_{ss}$	$-0.019 \pm 0.005$
$\delta_{ovl}$	$-0.011 \pm 0.004$

**Table 10.5:** Fitted parameters of the final fit to determine  $\phi_s$

The invariant mass and the proper time distribution of the selected  $B_s^0 \rightarrow J/\Psi\pi^+\pi^-$  candidates are well described by fit. Figure 10.7 shows the proper time distribution also for a wider range and with logarithmic scaling to confirm that the fit describes the tails at higher proper times.

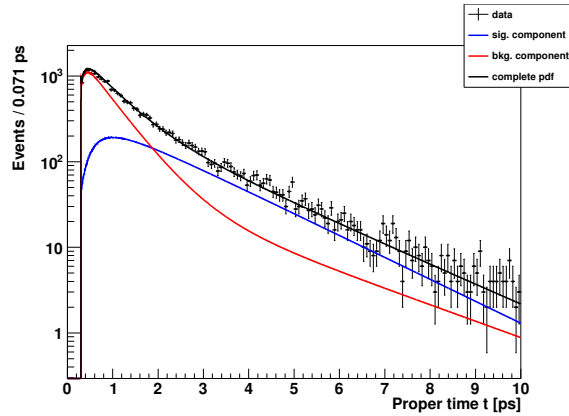


**Figure 10.7:** Proper time distribution of the selected  $B_s^0$  candidates with the 1-dimensional projected time PDFs in a wider range from 0 - 10 ps with logarithmic scaling

# 11 Estimation of Systematic Uncertainties

To estimate the systematic uncertainties of the determined value of  $\phi_s$ , the detector and background parameters fixed in the fit are varied within their estimated uncertainty and the resulting deviation of  $\phi_s$  is determined. For parameters that have been constrained with Gaussian errors in the fit, the systematic uncertainty is already included in the statistical uncertainty of the result. Thus, the parameters that will be studied are the time resolution, the acceptance parameters and the ratio  $\sigma_{1,m}/\sigma_{2,m}$  in the signal mass PDF.

In simulated prompt  $J/\Psi$ 's  $+\pi^+\pi^-$  decays and  $B_s^0 \rightarrow J/\Psi f_0(980)$  decays in chapter 6.1 it was observed that the average widths of the pull distributions of the measured proper time distributions are slightly different although their values are compatible within the determined uncertainties. Nevertheless, the relative difference of 1.68 % is taken into account by a relative 1.68 % systematic uncertainty of the scaling factors  $s_i$  that is quadratically added to the measured statistical uncertainty obtained in the determination of the time resolution. The total uncertainty of the scaling parameters of the resolution model are given in table 11.1.

parameter	value $\pm$ (stat) $\pm$ (sys)	total error
$s_1$	$1.2951 \pm 0.0066 \pm 0.022$	$\pm 0.023$
$s_2$	$2.601 \pm 0.04 \pm 0.044$	$\pm 0.059$
$s_3$	$13.61 \pm 0.14 \pm 0.228$	$\pm 0.27$

**Table 11.1:** Scaling factors of the per event resolution model with statistical and systematic uncertainties

It could also not be validated that the time acceptance of the channels  $B_s^0 \rightarrow J/\Psi f_0(980)$  and  $B^0 \rightarrow J/\Psi K^*(892)$  are exactly the same in the simulation. The acceptance parameter of simulated  $B^0 \rightarrow J/\Psi K^*(892)$   $a_{sig}$  is 0.74% smaller,  $t_{0,sig}$  is 46% larger and  $n_{sig}$  is 6.5% smaller than for simulated  $B_s^0 \rightarrow J/\Psi f_0(980)$ . Thus, the uncertainties will be also varied in the direction in which the difference occurred in the simulation, i.e.  $a_{sig}$  and  $n_{sig}$  are enlarged by 1  $\sigma$  while  $t_{0,sig}$  is decreased by 1  $\sigma$ . For consistency, the total uncertainty is also added and subtracted to all parameters at the same time. The total uncertainty of the signal time acceptance parameters are given in table 11.2.

parameter	value $\pm$ (stat) $\pm$ (sys)	total error
$a_{sig}$	$1.914 \pm 0.03 \pm 0.014$	$\pm 0.033$
$t_{0,sig}$	$0.135 \pm 0.0045 \pm 0.062$	$\pm 0.062$
$n_{sig}$	$1.843 \pm 0.05 \pm 0.12$	$\pm 0.13$

**Table 11.2:** Signal time acceptance parameters with statistical and systematic uncertainties

The background time acceptance parameters and their statistical uncertainties are given in table 11.3.

parameter	value $\pm$ (stat)
$a_{bkg}$	$3.23 \pm 0.09$
$n_{bkg}$	$4.83 \pm 1.09$

**Table 11.3:** Background time acceptance parameters with statistical uncertainties

In [37], it was shown that the CP-odd fraction of the selected signal  $B_s^0 \rightarrow J/\Psi \pi^+ \pi^-$  decays is greater than 0.977 at 95 % confidence level. To account for possible CP-even final states, the mistag probability of the tagging algorithms is increased by 2.3 % which is equivalent to a CP-even component of the same size.

The changes of  $\phi_s$  when varying the parameters are given in table 11.4. In this table, “+ 1  $\sigma$ ” and “- 1  $\sigma$ ” denotes adding respectively subtracting the total uncertainty. “ $\pm \sigma$ ” denotes the change of the signal acceptance parameters in the direction in which the difference occurred in the simulation.

changed parameter	$\phi_s \pm$ (stat)
Nominal unchanged	$-0.074 \pm 0.177$
Time Resolution scaling factors + 1 $\sigma$	$-0.075 \pm 0.179$
Time Resolution scaling factors - 1 $\sigma$	$-0.073 \pm 0.176$
Signal Time Acceptance parameters $\pm 1 \sigma$	$-0.061 \pm 0.168$
Signal Time Acceptance parameters + 1 $\sigma$	$-0.076 \pm 0.177$
Signal Time Acceptance parameters - 1 $\sigma$	$-0.061 \pm 0.170$
Background Time Acceptance parameters + 1 $\sigma$	$-0.076 \pm 0.177$
Background Time Acceptance parameters - 1 $\sigma$	$-0.074 \pm 0.177$
2.5 % enlarged wrong-tag probability	$-0.068 \pm 0.184$
$\frac{\sigma_{1,m}}{\sigma_{2,m}} + 1 \sigma$	$-0.074 \pm 0.177$
$\frac{\sigma_{1,m}}{\sigma_{2,m}} - 1 \sigma$	$-0.074 \pm 0.177$

**Table 11.4:** Estimation of the systematic uncertainties

While changing most of the parameters has only a small influence on the measured  $\phi_s$ , the uncertainty in the signal time acceptance has a large impact. Varying the parameters according to the differences observed in simulation,  $\phi_s$  increases from -0.074 to -0.061. The overall systematic uncertainty of the determination of  $\phi_s$  is determined by adding all determined differences quadratically. For the difference of the signal time acceptance, only the largest difference when changing the parameters in the direction in which the difference occurred, is taken into account. It yields a systematic uncertainty of 0.015. This is small compared to the statistical uncertainty of 0.177.

## 12 Summary and Conclusion

This thesis presents the determination of the CP-violating phase  $\phi_s$  in  $B_s^{(-)} \rightarrow J/\Psi \pi^+ \pi^-$  decays which is an almost pure CP-odd eigenstate. The analyzed data sample has been collected in 2011 by the LHCb-experiment and corresponds to an integrated luminosity of  $\mathcal{L} = 1.03 \text{ fb}^{-1}$ . The fitting procedure that is applied to determine  $\phi_s$  is a 2-dimensional unbinned maximum likelihood fit to the mass and proper time distributions of the selected  $B_s^0$  candidates where the mass is used to separate the signal and background component. It is shown that the background of the selected mass region between 5320 and 5600 MeV is composed of pure combinatorics so that the background of the proper time distribution can be modeled by the background candidates of the upper sideband in the  $B_s^0$  mass distribution. For the selected  $\pi^+ \pi^-$  states in the  $f_0(980)$  mass peak region which make up about a half of all selected  $\pi^+ \pi^-$  signal states, it is shown that they exhibit an almost pure spin-0 state so that the contribution from CP-even final  $J/\Psi \pi^+ \pi^-$  states can be assumed to be compatible with zero. To perform a measurement of the time-dependent CP asymmetry, information of the initial production flavour is used. The effective proper time resolution of 42.6 fs is determined with prompt  $J/\Psi$ 's combined with two prompt pions that fake a  $B_s^0$ . Time acceptance effects due to selection cuts are determined with  $B^0 \rightarrow J/\Psi K^*(892)$  decays. Correcting for time acceptance and time resolution and using  $\Gamma_s$ ,  $\Delta\Gamma_s$  and  $\Delta m_s$  constrained to previous measurements, the fit yields  $7148 \pm 97 B_s^0 \rightarrow J/\Psi \pi^+ \pi^-$  signal decays. The obtained CP-violating phase is

$$\phi_s = -0.074 \pm 0.177 \text{ (stat)} \pm 0.015 \text{ (syst) rad}$$

which is compatible with the Standard Model expectation for  $\phi_s^{SM} = (-0.0363_{-0.0015}^{+0.0016}) \text{ rad}$  [20]. A similar measurement has already been performed in LHCb in [40]. The analysis has used the opposite side tagging algorithm only and with  $7421 \pm 105$  signal events, the value of  $\phi_s = -0.019_{-0.174}^{+0.173} \pm_{-0.003}^{+0.004} \text{ rad}$  has been obtained. By applying a different selection, the signal-to-background ratio is significantly larger and the statistical uncertainty is smaller although the same side tagger has not been included. Both results agree well within their uncertainties.

In the presented analysis, systematic uncertainties due to the determination of the time resolution and the time acceptance parameters and a possible CP-even component are determined to be small compared to the statistical uncertainty. Including the events of the expected integrated luminosity of  $2.2 \text{ fb}^{-1}$  that will be collected until the end of 2012, will decrease the statistical uncertainty by about 43 %. Until 2015, the effective integrated luminosity might exceed  $5 \text{ fb}^{-1}$  which leads to a 55 % smaller statistical uncertainty and a much more significant measurement. By applying the selection cuts of [40], the signal-to-background ratio can be improved by about 30 - 40 %. The systematic uncertainty is dominated by the uncertainty of the signal time acceptance. It can be reduced with an improved understanding of the correct time acceptance. By allowing the constrained acceptance parameters to float, the uncertainty is included in the statistical uncertainty.

---

Since the measurement of the channel  $B_s^0 \rightarrow J/\Psi \pi^+ \pi^-$  will be statistically competitive with  $B_s^0 \rightarrow J/\Psi \phi$  when the larger data set is included, it will provide a cross-check measurement for the angular-dependent analysis in  $B_s^0 \rightarrow J/\Psi \phi$ . The results from  $B_s^0 \rightarrow J/\Psi \phi$  decays [14] and  $B_s^0 \rightarrow J/\Psi \pi^+ \pi^-$  decays [40] have been combined to  $\phi_s = -0.002 \pm 0.083$  (*stat*)  $\pm 0.027$  (*syst*) rad [14]. This is the most precise determination of  $\phi_s$ .

# Bibliography

- [1] lhcb public web site : <http://lhcb.web.cern.ch/lhcb/>.
- [2] Particle Data Group(PDG) : <http://pdg.lbl.gov/>.
- [3] M. Kobayasi and T. Maskawa. *CP Violation in the Renormalizable Theory of Weak Interaction, Progress of Theoretical Physics, VoL 49, No. 2, February 1973.*
- [4] Lincoln Wolfenstein. *Parameterization of the Kobayashi-Maskawa Matrix.* 1983.
- [5] Isard Dunietz, Robert Fleischer, Ulrich Nierste. *In Pursuit of New Physics with  $B_s$  Decays.*
- [6] Ulrich Nierste. *Three Lectures on Meson Mixing and CKM phenomenology, arXiv:0904.1869v1.*
- [7] The LHCb Collaboration. *Road map for the measurement of mixing induced CP violation in  $B_s^0 \rightarrow J/\Psi\phi$  at LHCb, arXiv:0904.1869v1.*
- [8] J. Beringer et al.(PDG) *CP violation in Meson Decays.*
- [9] J. H. Christenson, J.W. Cronin, V.L. Fitch and R. Turlay. *Evidence for the  $2\pi$  decay of the  $K_2^0$  Meson, Phys. Rev. Lett. 13, 138 (1964).*
- [10] The BABAR Collaboration. *arXiv:hep-ex/0703016v2, Observation of CP Violation in  $B^0 \rightarrow K^+\pi^-$  and  $B^0 \rightarrow \pi^+\pi^-$ .*
- [11] Giovanni Punzi. *Comments on Likelihood fits with variable resolution, arXiv:physics/0401045v1.*
- [12] The LHCb Collaboration. LHCb-PAPER-2011-021: *Measurement of the CP-violating phase  $\phi_s$  in the decay  $B_s^0 \rightarrow J/\Psi\phi$ .*
- [13] CDF Collaboration. LHCb-PAPER-2011-021: *Measurement of the CP-Violating phase  $\beta_s^{J/\Psi\phi}$  in  $B_s^0 \rightarrow J/\Psi\phi$  decays, arXiv:1112.1726v1.*
- [14] The LHCb Collaboration. LHCb-CONF-2012-002: *Tagged time-dependent angular analysis of  $B_s^0 \rightarrow J/\Psi\phi$  decays at LHCb.*
- [15] The LHCb Collaboration. LHCb-PAPER-2011-010: *Measurement of the  $B_s^0 - \bar{B}_s^0$  oscillation frequency  $\Delta m_s$  in  $B_s^0 \rightarrow D_s^-(3)\pi$  decays, arXiv:1112.4311v2.*
- [16] Yuehong Xie. *arXiv:0905.0724v1: sFit: a method for background subtraction in maximum likelihood fit.*
- [17] The CKMfitter Group. *Updated Results on the CKM Matrix.*

- 
- [18] The CKMfitter Group. CP Violation and the CKM Matrix: *Assessing the Impact of the Asymmetric B Factories*. *Eur. Phys. J. C* **41**, 1-131 (2005) [[hep-ph/0406184](http://hep-ph/0406184)], updated results and plots available at: <http://ckmfitter.in2p3.fr>.
- [19] A. Lenz, U. Nierste. arXiv:1008.1593v3: *Anatomy of New Physics in  $B - \bar{B}$  mixing*
- [20] The CKMfitter Group. arXiv:1106.4041v2: *Predictions of selected flavour observables within the Standard Model*
- [21] Lyndon Evans and Philip Bryant (editors). JINST, 3:S08001, 2008: *LHC Machine*.
- [22] CERN Public Webpage. <http://public.web.cern.ch/>.
- [23] CERN. <http://lhc.web.cern.ch/lhc/>: *LHC Design Report*.
- [24] The LHCb Collaboration. 2008 JINST 3 S08005: *The LHCb Detector at the LHC*.
- [25] LHCb Magnet Design Team. Technical Design Report CERN/LHCC/2000-007: *LHCb Magnet*.
- [26] The LHCb Collaboration. Technical Design Report CERN/LHCC/2000-037: *LHCb RICH*.
- [27] P.A. Cerenkov. *Phys. Rev.* **52**, 378: *Visible Radiation Produced by Electrons Moving in a Medium with Velocities Exceeding that of Light*.
- [28] The LHCb Collaboration. Technical Design Report, CERN/LHCC/2001-011: *LHCb Vertex Locator*.
- [29] The LHCb Collaboration. Technical Design Report CERN/LHCC/2001-010: *LHCb Muon System*.
- [30] The LHCb Collaboration. Technical Design Report CERN/LHCC/2002-029: *LHCb Inner Tracker*.
- [31] The LHCb Collaboration. Technical Design Report CERN/LHCC/2001-024: *LHCb Outer Tracker*.
- [32] The LHCb Collaboration. LHCb-ANA-2011-001: *Selections and lifetime measurements for exclusive  $b \rightarrow J/\Psi X$  decays with  $J/\Psi \rightarrow \mu^+ \mu^-$  with 2010 data*.
- [33] The LHCb Collaboration. LHCb 2009-025: *Lifetime unbiased selection of  $B_s^0 \rightarrow J/\Psi \phi$  and related control channels:  $B^0 \rightarrow J/\Psi K^*$  and  $B^+ \rightarrow J/\Psi K^+$* .
- [34] The LHCb Collaboration. LHCb-CONF-2012-026: *Performance of flavour tagging algorithms optimised for the analysis  $B_s^0 \rightarrow J/\Psi \phi$* .
- [35] The LHCb Collaboration. LHCb-CONF-2012-032: *Optimization and calibration of the Same-Side Kaon tagging algorithm using hadronic  $B_s^0$  decays in 2011 data*.
- [36] The LHCb Collaboration. LHCb-PAPER-2011-027: *Opposite-side flavour tagging of B mesons at the LHCb experiment*.

- [37] The LHCb Collaboration. LHCb-PAPER-2012-005: *Analysis of the resonant components in  $B_s^0 \rightarrow J/\Psi\pi^+\pi^-$  .*
- [38] The LHCb Collaboration. LHCb-PAPER-2011-031: *Measurement of the CP violating phase  $\phi_s$  in  $B_s^0 \rightarrow J/\Psi f_0(980)$  .*
- [39] The LHCb Collaboration. LHCb-ANA-2011-051: *Measurement of  $\phi_s$  in  $\bar{B}_s^0 \rightarrow J/\Psi f_0(980)$ .*
- [40] The LHCb Collaboration. LHCb-PAPER-2012-006: *Measurement of the CP-violating phase  $\phi_s$  in  $\bar{B}_s^0 \rightarrow J/\Psi\pi^+\pi^-$  decays.*
- [41] The ATLAS Collaboration. CERN-PH-EP-2012-218: *Observation of a New Particle in the Search for the Standard Model Higgs Boson with the ATLAS Detector at the LHC.*
- [42] The LHCb Collaboration. Physics Letters B 694 (2010) 209-216: *Measurement of the  $\sigma(pp \rightarrow bbX)$  at  $s = \sqrt{7}$  TeV in the forward region.*



# Danksagung

Ich möchte an dieser Stelle noch einigen Menschen danken:

Meiner Familie, weil sie mich mein ganzes Leben lang unterstützt hat wo sie nur konnte, sei es seelisch oder finanziell.

Ulrich Uwer für die Betreuung, dass er sich für jeden Einzelnen aus der Gruppe so viel Zeit nimmt, was in meinen Augen keine Selbstverständlichkeit ist.

Christian und Sebastian für die technische Betreuung. Auch wenn ich mal schwer von Begriff war, haben sie mir so viel geholfen. Ich habe viel gelernt in dem Jahr.

Der ganzen LHCb Gruppe Heidelberg, für die schöne Zeit und für die Hilfsbereitschaft.

Andreas, Adrian und Waldemar. Wir hatten eine echt schöne Studienzeit.

Allen meinen Freunden und Verwandten, weil sie mein Leben begleiten und es lebenswert machen.



Erklärung:

Ich versichere, dass ich diese Arbeit selbständig verfasst und keine anderen als die angegebenen Quellen und Hilfsmittel benutzt habe.

Heidelberg, den .....

.....

Unterschrift